OUKA
The University of Osaka
Institutional Knowledge Archive

Title	Structure-function relationships of the menaquinol:cytochrome c oxidoreductase in the green sulfur bacterium Chlorobaculum tepidum
Author(s)	岸本, 拓
Citation	大阪大学, 2023, 博士論文
Version Type	VoR
URL	https://doi.org/10.18910/92176
rights	
Note	

The University of Osaka Institutional Knowledge Archive : OUKA

https://ir.library.osaka-u.ac.jp/

The University of Osaka

Structure-function relationships of the menaquinol:cytochrome *c* oxidoreductase in the green sulfur bacterium *Chlorobaculum tepidu*m

緑色硫黄細菌 *Chlorobaculum tepidu*m におけるメナキノール:
シトクロム *c* 酸化還元酵素の構造機能相関

Doctoral dissertation

Hiraku Kishimoto

2022

Graduate School of Science
Osaka University

Table of Contents

Abbreviation **1**

Abstract **2**

General Introduction **4**

Over view of photosynthesis 4

Cytochrome *bc* complexes 11

Outline of the dissertation 18

Chapter I. Biochemical Analyses of cyt *c*-556$_{sol}$ **19**

Introduction 19

Materials and Methods 21

Results 25

Discussion 31

Chapter II. Structural Analyses of cyt *c*-556$_{sol}$ **33**

Introduction 33

Materials and Methods 34

Results 36

Discussion 46

Chapter III. Structural Analyses of the Rieske$_{sol}$ **49**

Introduction 49

Materials and Methods 52

Results 55

Discussion 73

Chapter IV. NMR analysis of the interactions between the Rieske$_{sol}$ and cyt *c*-556$_{sol}$ 76

Introduction 76

Materials and Methods 78

Results 82

Discussion 93

General Discussion and Conclusion 99

List of Publication 103

Acknowledgements 104

References 105

Abbreviation

ADP	Adenosine diphosphate
ATP	Adenosine triphosphate
CBB	Coomassie Brilliant Blue
Ccm	Cytochrome *c* maturation
Cyt	Cytochrome
CQ	Caldariellaquinone
DTT	Dithiothreitol
ESR	Electron spin resonance
FNR	Ferredoxin-$NADP^+$ reductase
Fd	Ferredoxin
MK	Menaquinone
NADP	Nicotinamide adenine dinucleotide phosphate
NMR	Nuclear magnetic resonance
OEC	Oxygen evolving complex
PC	Plastocyanin
PCR	Polymerase chain reaction
PDB	Protein data bank
pmf	Proton motive force
PS	Photosystem
Q	Quinone
QH_2	Quinol
RC	Reaction center
Rieske ISP	Rieske iron sulfur protein
RMSD	Root-mean-square deviation
SAD	Single-wavelength anomalous diffraction
SDS-PAGE	Sodium dodecyl sulphate-polyacrylamide gel electrophoresis

Abstract

In green sulfur photosynthetic bacteria, the electron transfer reaction from menaquinol:cytochrome *c* oxidoreductase (Rieske/cytochrome (cyt) *b* complex) lacks *c*-type cytochrome which is thought that other cyt *bc* complexes were obtained in evolutionary process and was proposed to have the most primitive structure and function. This complex was thought to transfer electron to the P840 reaction center complex (RC) directly without any electron carrier proteins. In contrast, spectroscopic data indicated that mono-heme cyt *c* which an α-absorption peak at 556 nm was involved in electron transfer between the Rieske/cyt*b* complex and RC. The *CT0073* gene was the candidate for the gene encoding this cytochrome *c* (cyt *c*-556), and it was supposed to anchor to the membrane with fatty acid. However, detailed biochemical and structural properties of cyt *c*-556 have not been verified. The properties of the Rieske/cyt*b* complex is also still unknown. Because of these, I aimed to reveal the electron transfer mechanisms between the Rieske/cyt*b* complex and RC, and also to verify the evolutionary process of cyt *bc* complexes in terms of structure and function of these complex.

In this study, I detected that the *CT0073* gene express in membrane and encode cyt *c*-556. The three-dimensional structures of the soluble domains of cyt *c*-556 (designated cyt *c*-556$_{sol}$) and the Rieske iron-sulfur protein (designated Rieske$_{sol}$) from green sulfur bacterium *Chlorobaculum tepidum* were determined by X-ray crystallography. The overall fold of cyt *c*-556$_{sol}$ consists of four α-helices and is very similar to that of water-soluble cyt *c*-554, which independently functions as an electron donor to the RC, except for its remarkably long and flexible loop between the α3 and α4 helices. On the other hand, the structure of the Rieske$_{sol}$ shows a typical β-sheets-dominated fold of nine not ten, with a

small cluster-binding and large subdomains. The Rieske$_{sol}$ belongs to b_6f-type Rieske ISPs although its C-terminal extension is missing, as in the case of bc_1-type Rieske ISPs. Nuclear magnetic resonance measurements revealed weak non-polar but specific interaction sites on the Rieske$_{sol}$ when mixed with cyt *c*-556$_{sol}$. Therefore, the Rieske/cyt*b* complex is supposed that it tightly associated with cyt *c*-556 and could not function independently.

Based on these results, I propose electron transfer model between the Rieske/cyt*b* complex and RC that electron transfer is not conducted directly but conducted with membrane-anchored cyt *c*-556. The evolutionary scenario of cyt *bc* complexes which is different from the previously proposed one is also presented. I propose the scenario that the Rieske/cyt*b* complex and cyt *c*-556 was evolved into cyt b_6f type complex with replacement of membrane-anchored cyt *c*-556 with transmembrane cyt *f*.

General Introduction

Overview of photosynthesis

Mechanisms of photosynthesis

Photosynthesis is the reaction which converts light energy from the sun to chemical energy. It largely contributes to primary production on the present earth. In plants, photosynthesis is composed of two reactions, photosynthetic electron transport and carbon fixation (Figure 1). Photosynthetic electron transport takes place in thylakoid membrane. Light absorption, excitation energy transfer, electron transfer reaction and water cleavage are conducted in this system. Protons, electrons and oxygen are produced by water cleavage reaction. Electrons are transferred via electron transport chain and finally utilized for NADPH production. In addition, proton motive force (*pmf*) generated by proton translocation across membrane coupled with electron transport is used for ATP synthesis. Carbon fixation takes place in the stroma. It is involved in the fixation of carbon dioxide into carbohydrates via the photosynthetic carbon reduction cycle (Calvin-Benson cycle) [1].

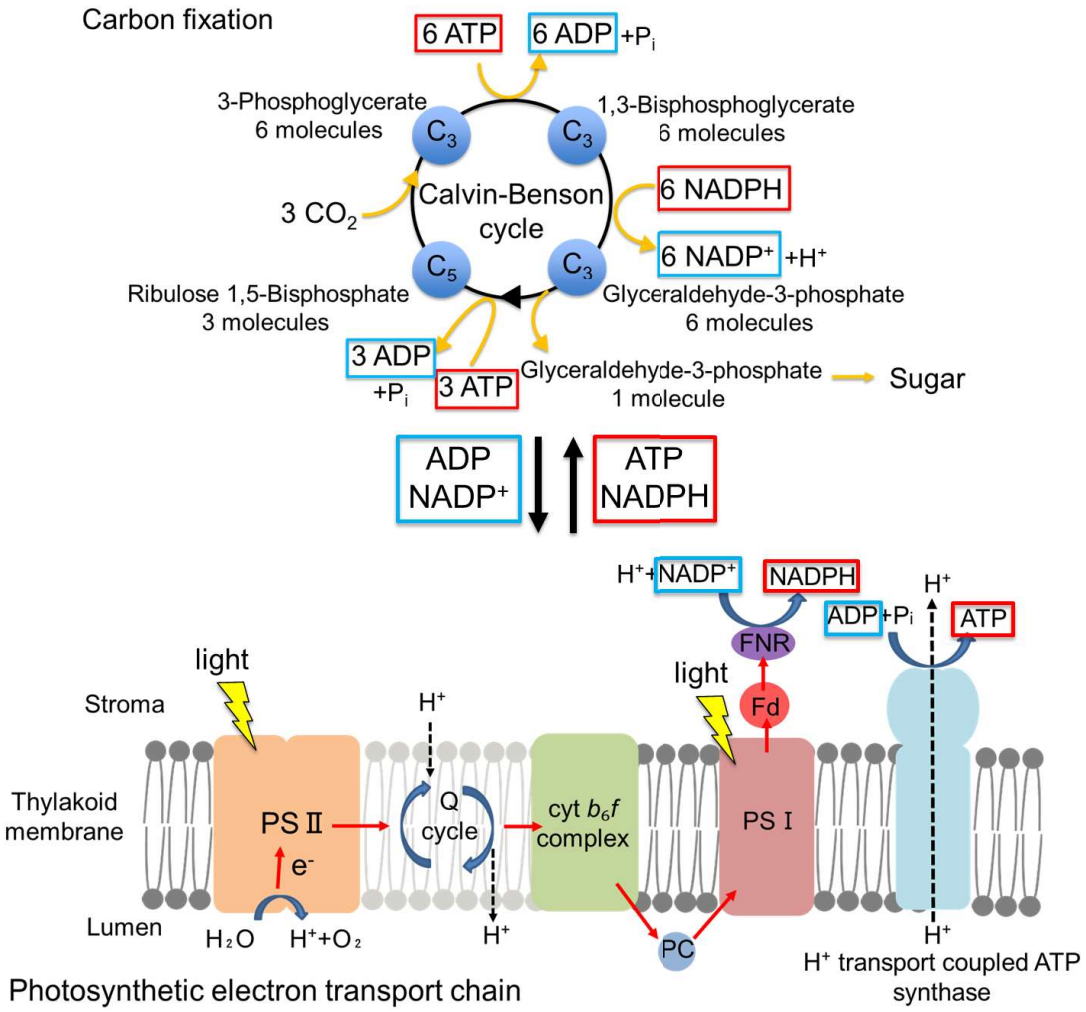


Figure 1. Scheme of photosynthesis in plants

Red arrows and black dotted arrows indicate the direction of electron and proton flows, respectively. PS, Q, cyt, PC, Fd and FNR represent photosystem, quinone, cytochrome, plastocyanin, ferredoxin and ferredoxin-$NADP^+$ reductase, respectively.

Electron transport chain in oxygenic photosynthesis

Photosynthetic electron transport is classified into two types in terms of oxygen evolution. Oxygenic photosynthesis is conducted by oxygenic phototrophs such as plants, algae and cyanobacteria. They utilize water as an electron source. Oxygenic phototrophs were appeared in the ancient ocean about 3.5 billion years ago, and cyanobacteria which contain chlorophyll *a* carry out oxygenic photosynthesis were appeared about 2.8 billion years ago [2].

Oxygenic photosynthetic electron transport chain contains mainly three membrane protein complexes, Photosystem (PS) I, PS II and cytochrome (cyt) b_6f complex (Figure 2). In PSII, light energy causes excitation of P680 which is a special pair of chlorophyll and primary electron donor in this system. Electrons are transferred to quinone by subsequent electron transfer reactions. At the same time, water cleavage is occurred by oxygen evolving complex (OEC). Quinone (Q) is reduced to quinol (QH_2), and then QH_2 is oxidized by cyt b_6f complex. The mechanism which includes oxidoreduction of quinone and quinol is called Q-cycle [3]. With the oxidation of QH_2, two electrons are transferred to cyt b_6f complex. One is utilized for reduction of quinone to QH_2 and the other is transferred to cyt *f* via the Rieske ISP. Then, electron transferred from cyt *f* to PSI by copper protein plastocyanin in plants or cyt c_6 in cyanobacteria. After light absorption of PSI, P700 in PSI is excited, and electron is transferred to iron-sulfur cluster. PSI oxidizes plastocyanin or cyt c_6 and transfers electron to ferredoxin. Electron is transferred to ferredoxin-$NADP^+$ reductase to be utilized for reduction of $NADP^+$ to NADPH. In addition, ATP synthesis is driven by *pmf* at proton transport coupled ATP synthase [4].

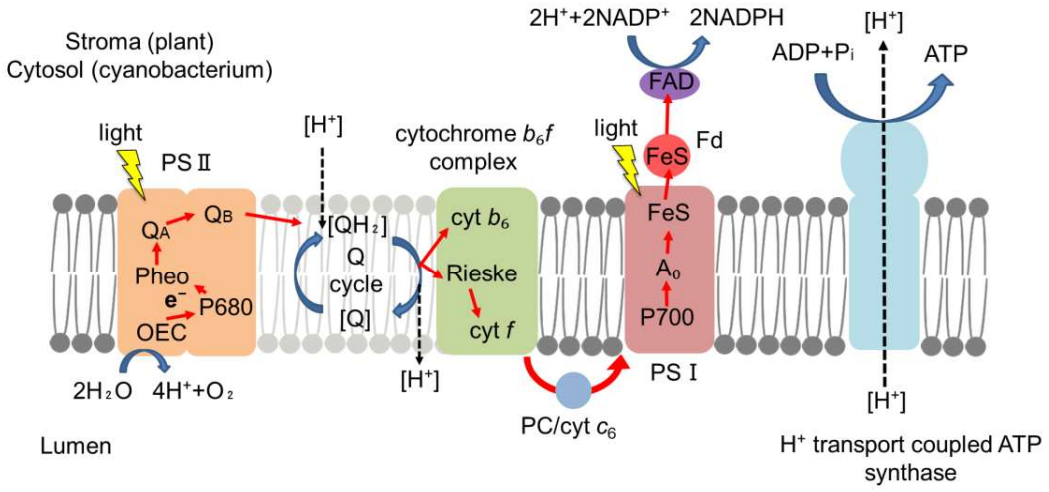


Figure 2. Electron transport chain in oxygenic photosynthesis

Red arrows and black dotted arrows indicate the direction of electron and proton flows, respectively. OEC, Pheo and FeS represent oxygen evolving complex, pheophytin and iron-sulfur cluster, respectively. Copper protein plastocyanin shuttles electron between cyt *f* and PSI in plants, while cyt c_6 does in cyanobacteria.

Electron transport chain in anoxygenic photosynthesis

Anoxygenic photosynthesis is carried by photosynthetic bacteria such as purple bacteria, green sulfur bacteria and heliobacteria [2, 5]. Water is not utilized as electron source in this system; therefore, oxygen does not evolve. Electron transport chain of anoxygenic photosynthesis is composed with two transmembrane protein complexes, cyt *bc* complex and reaction center (RC), while three complexes are contained in chain of oxygenic photosynthesis. RC can be classified into two types, type I and type II RCs, in terms of terminal electron acceptors. Type II RC contains quinone as terminal electron acceptor and functions in purple bacteria. Electron transport chain in purple bacteria forms cyclic electron flow (Figure 3). Electrons are utilized to reduction of Q to QH_2 at type II RC. QH_2 is oxidized by cyt bc_1 complex in Q-cycle mechanism. Then, electron is transferred from cyt bc_1 complex to type II RC via cyt c_2 [6].

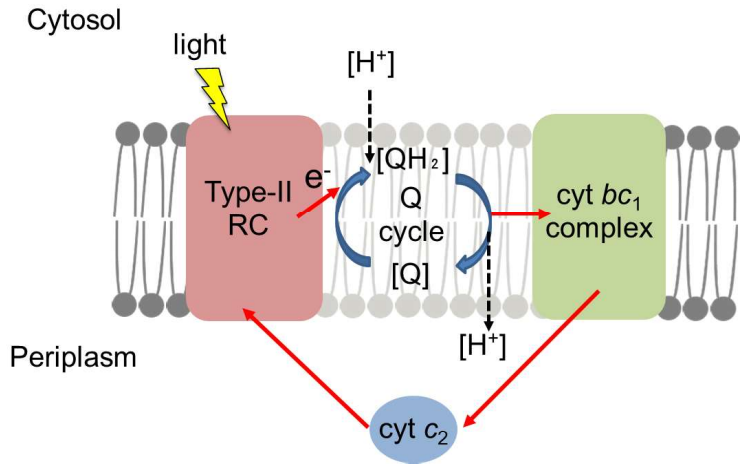


Figure 3. Scheme of electron transport chain in purple bacteria

Red arrows and black dotted arrows indicate the direction of electron and proton flows, respectively. Cyt bc_1 complex and type II RC form cyclic electron transport chain.

Type I RC contains iron-sulfur cluster as final electron acceptor and functions in electro transport chain of anoxygenic photosynthesis in green sulfur bacteria and heliobacteria. Green sulfur bacteria have two electron transfer pathways (Figure 4). One use sulfide for electron donor and the other use thiosulfate. Sulfide-quinone reductase (SQR) accepts electrons from sulfide and transfer them to the Rieske/cyt*b* complex via Q-cycle, resulting in the production of *pmf* for ATP synthesis [7]. Electron transfer from the Rieske/cyt*b* complex to type I RC is conducted by membrane-anchored cyt *c*-556. This protein is thought to accept an electron from the Rieske ISP and transfer it to transmembrane cyt c_Z in type I RC. Finally, an electron is transferred FNR via ferredoxin and utilized to reduce $NADP^+$. An electron from thiosulfate is transferred to soluble cytochrome *c*-554 located in periplasmic side via sulfur oxidation (Sox) system [8]. Cyt *c*-554 transfer an electron to cyt c_Z as cyt *c*-556.

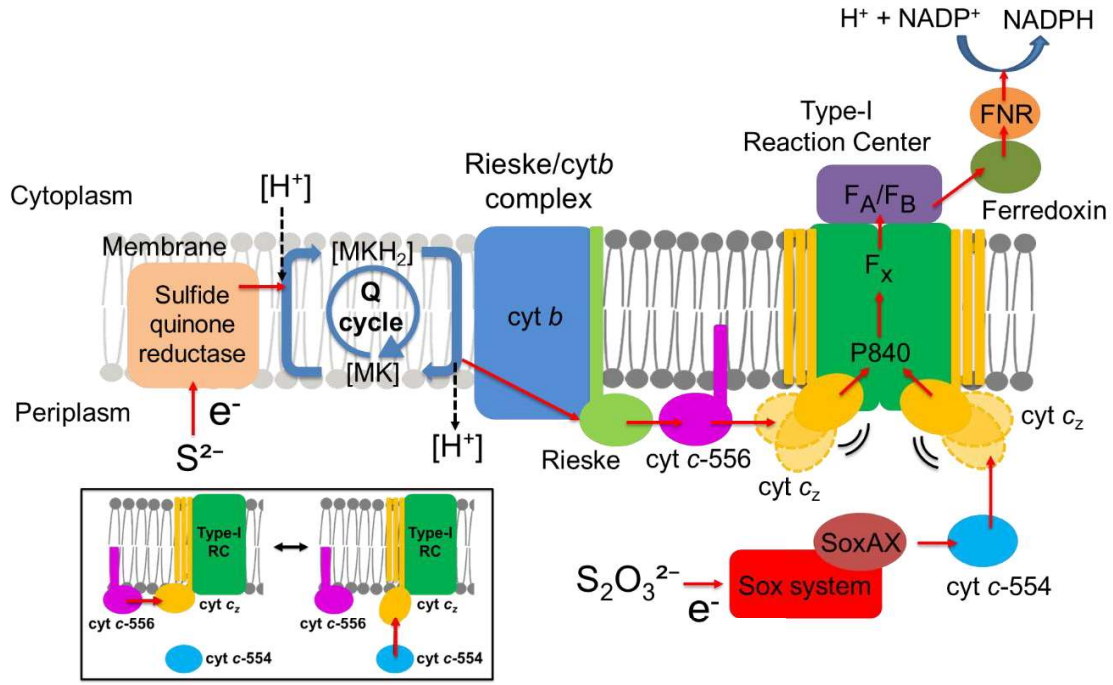


Figure 4. Scheme of electron transport chain in green sulfur bacteria

Red arrows and black dotted arrows indicate the direction of electron and proton flows, respectively. Menaquinone (MK) is used for Q-cycle mechanism in green sulfur bacteria. A heme-binding portion of membrane-bound cyt c_z is assumed to be exposed into the solvent and fluctuates during reaction to contact with its reaction partners, cyt *c*-556 and cyt *c*-554. Sulfide and thiosulfate serve as the electron sources for photosynthesis in *C. tepidum*. Sox represents sulfur oxidation and F_X and F_A/F_B represent iron-sulfur cluster. (Inset) A model to represent two different orientations of the C-terminal domain of cyt c_z, which associate with cyt *c*-556 and cyt *c*-554, respectively.

Cytochrome *bc* complexes

Outlines of cytochrome *bc* complexes

Cytochrome (cyt) *b*c complexes are multi-subunit membrane-bound enzymes that play central roles in respiratory and photosynthetic electron transport chains functioning in energy transducing systems of many organisms, including bacteria, archaea, eukaryotic mitochondria and chloroplasts [9]. Plants and cyanobacteria have cyt b_6f type complex, and mitochondrion and α-proteobacteria have cyt bc_1 type complex. These complexes consist of at least three catalytic subunits: Rieske ISP with a [2Fe-2S] cluster, cyt *b* with two *b*-type (one low potential (b_L) and one high potential (b_H)) hemes, and cyt c_1 or *f* ,with a *c*-type heme (Figure 5). In addition to these, cyt b_6f complex contains other cofactors as heme c_n, chlorophyll *a* and β-carotenoid, however, their functions have not been clarified in detail.

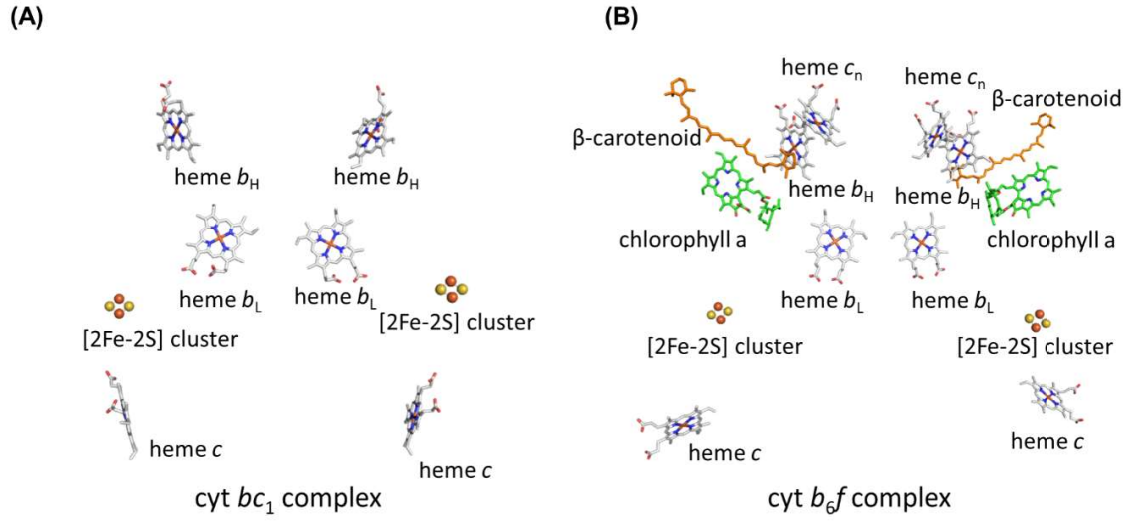


Figure 5. Cofactors in cyt *bc* complexes

Cofactors in (A) cyt bc_1 complex from purple bacterium, *Rhodobacter sphaeroides* (PDBID: 2QJP) [10] and (B) cyt b_6f complex from cyanobacterium, *Mastigocladus luminosus* (PDBID: 1VF5) [11]. Cyt b6f complex contains three other cofactors, heme c_n, chlorophyll *a* and β-carotenoid, in addition to the cofactors which this complex contains as well as cyt bc_1 complex.

Q-cycle mechanism in cyt *bc* complex

The Q-cycle mechanism is a well-known explanation for the function of cyt *b*c complexes, which catalyze oxidation of QH_2 to Q at the Q_o site and transfer the resultant two electrons in a bifurcation manner to opposite sides across the membrane [12]. Figure 6 shows the scheme of Q-cycle in cyt bc_1 complex. One electron moves to the high-potential chain of the [2Fe-2S]-type Rieske iron-sulfur center and the other via the low-potential chain of two *b*-type hemes to the Q_i site. A semiquinone produced at the Q_i site is then re-reduced to QH_2, following a second turnover at the Q_o site. Consequently, these electron transport reactions are coupled to proton transfer from the electrochemically negative to the positive side across the membrane, contributing to the production of *pmf* which is essential for a variety of cellular activities such as ATP synthesis [13]. Heme c_n supposed to be involved in Q-cycle mechanism of cyt b_6f complex. Some reaction mechanism models of Q-cycle in cyt b_6f complex have been proposed, however their details are still not clear.

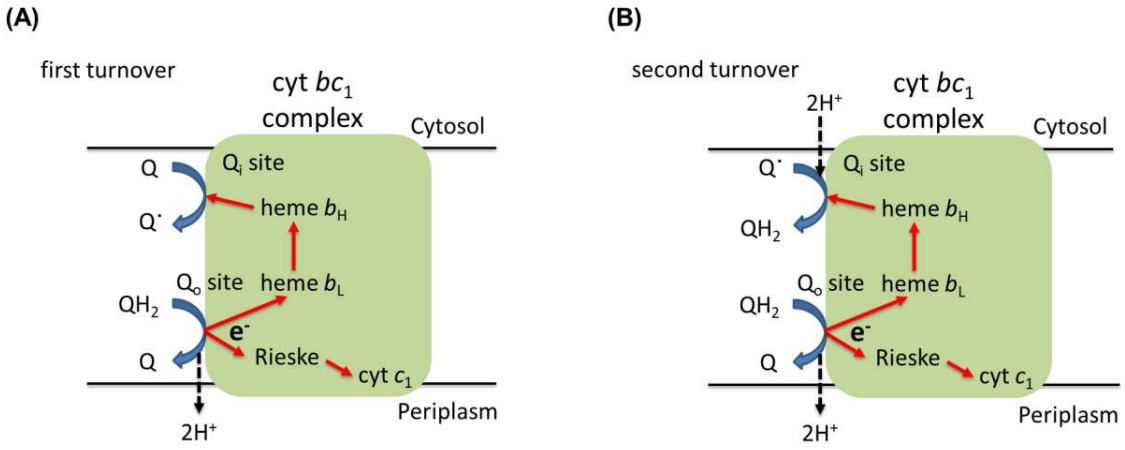


Figure 6. Q-cycle mechanisms in cyt *bc*1 complexes

Red arrows and black dotted arrows indicate the direction of electron and proton flows, respectively. (A) In first turnover, quinol (QH_2) was oxidized to quinone (Q) at Q_o site and electrons transferred to heme b_L and the Rieske ISP. An electron transferred to Q at Q_i site via heme b_H, and is utilized for reduction of Q to semiquinone ($Q^{\cdot}$). (B) In second turnover, electron transfer reaction as first turnover is carried out at Qo site. An electron transferred by heme b_L and b_H is utilized for reduction of $Q^{\cdot}$ to QH_2. These reaction result in the formation of *pmf*.

Diversity of cytochrome *bc* complexes

Cyt *bc* complex has been diverse among species during evolutionary process (Figure 7). Recent genome-wide analyses have clearly revealed that cyt *bc* and other related complexes, all of which are involved in QH_2 oxidation coupled with the proton pumping have a pair of *b*-type hemes and a Rieske iron-sulfur center in common as the catalytic core [14, 15]. This invariant functional unit is thought to have diverted into different types of Q-cycle-driven energy transducing complexes by incorporating structurally variable and evolutionally non-conserved electron carriers. For example, cyt bc_1 complex found in α-proteobacteria and mitochondria, and cyt b_6f complex found in photosynthetic cyanobacteria and chloroplasts assemble membrane-bound cyt c_1 and *f* to accept electrons from the Rieske center [14]. Moreover, di-heme cyt *c* in ε-proteobacteria, which belongs to the cyt c_4 family and is derived from a tandem repeat of two mono-heme class I-type cyts *c*, is integrated into the membrane to form the complex [16]. The C-terminal heme-binding motif (CxxCH) in this di-heme cyt *c* has recently been shown to be disrupted, resulting mono-heme cyt c_1 in α-proteobacteria and the hyperthermophilic bacterium *Aquifex aeolicus* [17]. In the case of *Bacillus* cytochrome *c*, the three membrane-spanning segments, which are equivalent to subunit IV split from cyt *b*, are fused to small mono-heme cyt *c* reminiscent of cyt *c*-551 on the N-terminal side [18]. Cyt *b* in the cyt b_6f complex is also divided into cyt b_6 and subunit IV by operon split. While two-*b* type hemes are contained in cyt b_6, PEWY (-Pro-Glu-Trp-Tyr-) motif which supposed to be essential for proton release at Q_o site in cyt bc_1 complex is located in subunit IV [19]. The Rieske/cyt*b* complex was found in green sulfur bacteria and archaea, which contains two catalytic subunits, The Rieske ISP and cyt *b*, while the other complexes contain at least three subunits, The Rieske ISP, cyt *b* and *c*-type cytochrome. This complex is thought to be a most primitive structural and functional complex [20].

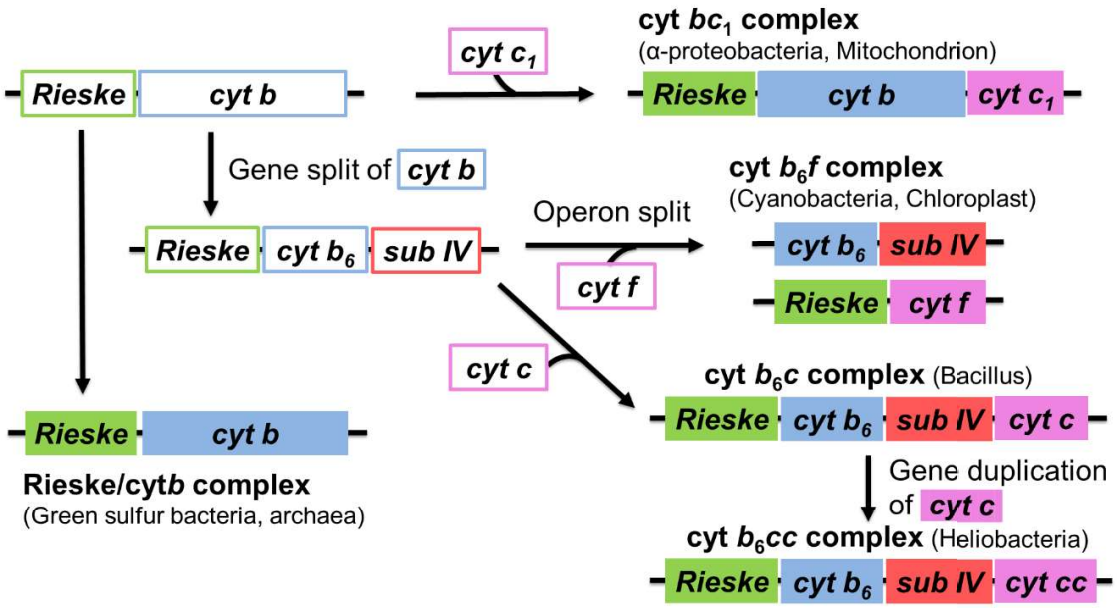


Figure 7. Predicted evolutionary paths of gene clusters encoding cyt *bc* complexes

The Rieske/cyt*b* complex found in green sulfur bacteria and archaea has been supposed to be the ancestral type of modern cyt *bc* complexes.

Rieske/cyt*b* complex in green sulfur bacteria

The genes encoding three subunits of the cyt bc_1 complex, the *fbcF* for the Rieske ISP, the *fbcB* for cyt *b* and the *fbcC* genes for cyt c_1, exist as a single transcriptional unit of the *fbc* operon in α-proteobacteria including purple bacteria (e.g., *Rhodobacter capsulatus* and *R. sphaeroides*) [21]. However, no *petA* gene (equivalent to *fbcC*) has been found either downstream or upstream of the unit housing the *petC* and *petB* genes (equivalent to *fbcF* and *fbcC*, respectively) in the green sulfur bacterium *Chlorobium limicola* (Chlorobiaceae) [22]. A Rieske/cyt*b*-type complex was therefore proposed to function by donating electrons directly to the P840 photosynthetic reaction center (RC) complex via the mono-heme cyt *c*-551 subunit (cyt c_z or PscC subunit) [23]. Contrary to this, spectroscopy data using membranes from *Chlorobaculum tepidum* have strongly indicated that another membrane-associated cyt *c* with an α-absorption peak at 556 nm, designated cyt *c*-556, was involved in the direct electron transfer reaction between the Rieske ISP and cyt c_z by playing the role as if cyt c_1 [24]. The *CT0073* gene is considered the most probable candidate encoding cyt *c*-556, judging from its location upstream of *CT0075* encoding water-soluble cyt *c*-554, because both products appeared to be functionally related to each other in that they both donate electrons independently to the P840 RC complex (Figure 4) [25]. However, the subunit composition of the complex involved in QH_2 oxidation coupled with *pmf* formation across the membrane is still unknown in green sulfur bacteria, despite its pivotal importance from both mechanistic and evolutionary perspectives.

Outline of the dissertation

Biochemical and structural information of the Rieske/cyt*b* complex, which is thought to be the most primitive type of cyt *bc* complex, is important for clarification of the electron transfer mechanisms and also for consideration of the evolutionary process of cyt *bc* complexes. However, it is difficult to extract the Rieske/cyt*b* complex from strictly anaerobic bacterium *C. tepidum* because it must be solubilized and purified under anaerobic conditions. Therefore, the biochemical and structural analyses of this complex has not progressed. Thus, I aimed to clarify the structure-function relationships between the Rieske ISP, cyt *c*-556 and cyt c_z which conduct electron transfer from the Rieske/cyt*b* complex to RC.

In this study, the C-terminal domains of CT0073 and Rieske ISP, both of which were expected to bind redox cofactors and be exposed to the periplasmic space, were successfully overexpressed in *Escherichia coli* cells. The resultant proteins, recovered in soluble states, were designated as CT0073$_{sol}$ and Rieske$_{sol}$ proteins, respectively. The biochemical and physicochemical properties of the CT0073$_{sol}$ agreed with the spectroscopy data on cyt *c*-556, obtained using membranes. The crystal structures of both CT0073$_{sol}$ (which more appropriately, should be referred to as cyt *c*-556$_{sol}$) and the Rieske$_{sol}$ protein were determined to explore their molecular interaction mechanism, as the Rieske ISP was supposed to transfer electrons from cyt *b* to cyt *c*-556 by swinging its head domain containing a [2Fe-2S] center. Nuclear magnetic resonance (NMR) measurements provided concrete evidence for their direct contact and identified interaction sites on the Rieske$_{sol}$ protein when the complex was formed with cyt *c*-556$_{sol}$. A molecular reaction model by which the electron transfer reaction mechanism could be explained from the Rieske/cyt*b*-type complex to the P840 RC complex via membrane-anchored cyt *c*-556 is presented.

Chapter I. Biochemical analyses of cyt *c*-556$_{sol}$

Introduction

In electron transport chain of green sulfur bacteria, electron transfer between cyt *bc* complex and RC by soluble *c*-type cytochrome or plastocyanin is not conducted. Instead of these soluble protein, membrane-anchored cytochrome *c*-556 has been suggested to be encoded by *CT0073* gene and transfer an electron between the Rieske/cyt*b* complex and RC by spectroscopic data. This protein was supposed to be anchored to membrane by fatty acid bonded cysteine residue in N-terminal domain. In order to analyze biochemical and structural properties of CT0073, the soluble C-terminal domain of it (CT0073$_{sol}$) which contains heme *c* was expressed in *E. coli*. In order to synthesize *c*-type cytochromes *in vivo*, cytochrome *c* maturation (ccm) system is essential (Figure 8). In the first step apo-cytochrome *c* and heme *c* are synthesized in cytoplasm. Then, they are transported to periplasm, and heme *c* is inserted to apo-cytochrome *c* by post-translational maturation pathway with proteins encoded by *ccm* gene clusters, resulting in synthesis of holo-cytochrome *c*. pEC86 plasmid contains *ccm* gene clusters and has been reported to be required for expression holo-cytochrome *c* in *E. coli* [26]. Therefore, the plasmid was designed to transport the target protein to the periplasm of *E. coli* and co-expressed with the pEC86.

In this chapter, I first examined whether CT0073$_{sol}$ exhibited the similar biochemical characteristics as cyt *c*-556, which had been observed *in vivo*. Then, I verified whether the CT0073 is actually expressed in the plasma membrane of *C. tepidum* by mass spectrometry. It was demonstrated previously that cyt c_Z, which is an electron acceptor in RC, efficiently receives an electron from the membrane anchored cyt *c*-556 and soluble *c*-

554 [24, 27]. There, I measured flash-induced absorption spectra to estimate the rate of electron transfer from CT0073$_{sol}$ to cyt c_z. Based on these results, CT0073 is designated as cyt *c*-556 in the following chapters.

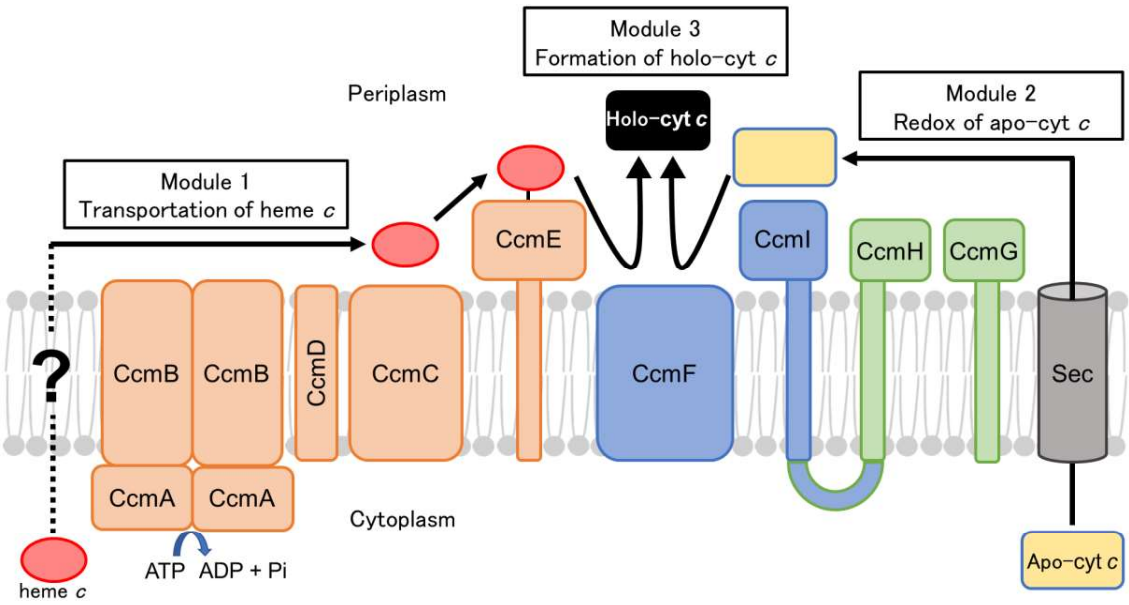


Figure 8. Biosynthesis of cytochrome *c* with cytochrome *c* maturation (ccm) system

Ccm system in *E. coli* is composed with nine proteins (CcmA-I). CcmH and CcmI are fused. Sec represents secretion protein. Ccm system is composed with three modules [28, 29]. CcmA-E in module 1 transport heme *c* to CcmF. CcmG and H in module 2 reduced reduce cysteine residues in heme-binding motif. Ccm F, I in module 3 form thioether bonds between heme *c* and cysteine residues in heme-binding motif. CcmH also functions at module 3. Mechanisms of heme *c* transportation from cytoplasm to periplasm are unknown.

Materials and Methods

Construction of truncated cyt *c*-556 expression plasmid

The truncated cyt *c*-556 expression plasmid was constructed as previously described [30]. A fragment from 193 to 429 bp in the *CT0073* gene encoding the C-terminal heme-containing moiety of cyt *c*-556 from Ala65 to Lys143 (designated C-cyt *c*-556) was amplified by PCR using the following primer pairs based on the sequence of the *CT0073* gene: (forward) 5'-AAACCATGGCGGAAGGCAAGACCATTTA-3' and (reverse) 5'-AAAGGATCCTTATTTCGAGATGCTGATCAGG-3' (restriction sites are underlined). Primers corresponding to the 5' ends were designed to introduce a NcoI site in the forward primer and a BamHI site in the reverse primer. The PCR fragment was digested with NcoI/BamHI restriction enzymes (TaKaRa Bio Inc., Shiga, Japan) and inserted into the multiple cloning site of the expression vector pET-20b(+) (Novagen Inc., Madison, WI, USA) which carries an N-terminal pelB signal sequence for the potential periplasmic localization of the target proteins. Cloning results were confirmed by nucleotide sequencing of the entire coding region.

Overexpression and purification of cyt *c*-556$_{sol}$

For expression of cyt *c*-556$_{sol}$, constructed plasmid was co-transformed with pEC86 plasmid (a generous gift from Dr. Linda Thöny-Meyer) into *E. coli* C41(DE3) [31, 32]. LB media were supplemented with 100 μg ml^{-1} ampicillin and 33 μg ml^{-1} chloramphenicol. A 7.5 ml pre-culture was prepared by growing at 37 °C for 7 h in a LB medium supplemented with 100 μg ml^{-1} ampicillin and 33 μg ml^{-1} chloramphenicol. After the inoculation into a 750 ml LB medium supplemented with the same concentrations of antibiotics, cells were grown at 30 °C for 60 h by gently stirring at 60-75 rpm using a non-

bladed Erlenmeyer flask avoiding foaming. Cells were harvested by centrifugation (10,000 x g) at 4°C for 10 min. Isopropyl-1-thio-β-D-galactopyranoside (IPTG) induction to overexpress the cyt *c*-556$_{sol}$ was not performed. This is because the addition of IPTG failed its expression and resulted in the accumulation of the apo-cyt *c*-556$_{sol}$ in a cytoplasmic space probably due to hinderance into the periplasmic space. Cyt *c*-556$_{sol}$ was extracted by osmotic shock following the procedure described in the Novagen pET System Manual (11th Edition). After the concentration using the Viospin 6-3K with ultrafiltration method (Sartorius AG, Göttingen, Germany), the cyt *c*-556$_{sol}$ was purified by size exclusion chromatography using HiLoad 26/600 Superdex 75 pg resin (GE Healthcare, Piscataway, NJ, USA) equilibrated with 50 mM Tris-HCl (pH 8.0) and 150 mM NaCl.

Redox titration

The redox titration was performed to determine the redox midpoint potential (E_m) of cyt *c*-556$_{sol}$ according to the method as previously described by Dutton (1978) with a double-beam spectrophotometer UV-3101 PC (Shimadzu, Kyoto, Japan) [33]. A continuous flow of argon gas was used to keep the vessel anaerobic. The protein solution for measurements contained 10 μM cyt *c*-556 in 100 mM Potassium phosphate buffer (pH 7.0). The redox mediators used were 10 μM 2,3,5,6-tetramethyl-1,4-phenylenediamine (DAD), 10 μM Phenazine ethosulfate (PES), 10 μM Phenazine methosulfate (PMS), and 10 μM 2-methyl-1,4-naphthoquinone (Vitamin K3). At the beginning of the measurements, the protein solution was reduced by the addition of sodium dithionite. Subsequently, the redox potential was raised stepwise by the addition of potassium ferricyanide.

Isolation of Chlorosome-depleted membranes

A deletion mutant of cyt *c*-554 of *C. tepidum* was constructed in previous study

[34]. Cells 2 days old were harvested by centrifugation and treated immediately to isolate their membranes to avoid damage to the cytochrome activity [27]. Chlorosome-depleted membranes were prepared according to the procedure described previously in an anaerobic chamber (Coy Laboratory Products, USA) [24].

SDS-PAGE and heme staining

Sodium dodecyl sulfate-polyacrylamide gel electrophoresis (SDS-PAGE) was performed by the method of Laemmuli [35], and the separated protein bands were stained with Coomassie brilliant blue. Heme-containing proteins were also revealed by peroxidase activity with 3,3',5,5'-tetramethylbenzidine (TMBZ). A kit of molecular-mass markers was purchased from Bio-Rad Laboratories (USA).

nLC/MS/MS

After the SDS-PAGE analysis of chlorosome-depleted membranes, the six different and consecutive gel spots, which were electrophoresed around 14-24 kDa in molecular mass, were excised out with Pasteur pipettes. These small gels were subjected to in gel-digestions with 0.1 μg of Trypsin Gold (Promega) at 37 °C overnight. The resultant peptides from extracts were separated by nanoscale liquid chromatography (nLC) using EASY-nLC (Proxeon, Denmark), and its mass spectra were analyzed with micrOTOF-QII (Bruker Daltonics, USA).

Flash-induced absorption changes

Flash-induced absorption changes were measured with a single-beam spectrophotometer at 295 K as described previously [36]. Chlorosome-depleted membrane preparations were suspended in 50 mM Tris–HCl (pH 8.0) supplemented with 1 mM

EDTA, 2 mM dithiothreitol, and 10 mM sodium ascorbate. The concentration of the membranes was adjusted to give an absorbance of 1.5 at 810 nm (equivalent to a 0.3 μM P840 concentration) by assuming the antenna size in the RC (BChl a/P840 ratio) to be 50 and the extinction coefficient (ε_{810}) for BChl a at 810 nm to be 100 mM^{-1} cm^{-1} [37, 38]. For the reconstitution experiments, the purified cyt *c*-556_{sol} was added to the membrane suspension to give a final concentration of approx.10 μM (an excess amount). Samples were placed in air-tight anaerobic cuvettes to avoid oxidative degradation. All of the buffers used in the present study were prepared and stored under anaerobic conditions.

Results

Biochemical properties of cyt *c*-556$_{sol}$

Truncated CT0073, which was expressed in the presence of the pEC86 plasmid in *E. coli*, was a soluble protein and harbored a *c*-type heme showing an α absorption peak at 556 nm (Figure 9A). Therefore, this protein is referred to as cyt *c*-556$_{sol}$ henceforth. The redox titration curve of cyt *c*-556 was obtained by plotting the peak heights of its α-absorption band against the ambient potential (E_h) (Figure 9B). The data points were fitted with a Nernst curve when the presence of one redox component was postulated, indicating that cyt *c*-556 has a single heme *c* as deduced from its amino acid sequence information. The redox midpoint potential (E_m) of heme was calculated to be +190 mV, which was almost the same as that reported previously for *c*-type cyt responsible for the electron transfer reaction between the Rieske ISP and cyt c_z [24, 39, 40]. Furthermore, the presence of CT0073 was confirmed to be expressed as cyt *c*-556 in chlorosome-depleted membranes by nLC/MS/MS analysis of peptides produced by tryptic digestion of heme-bound proteins (Figure 10).

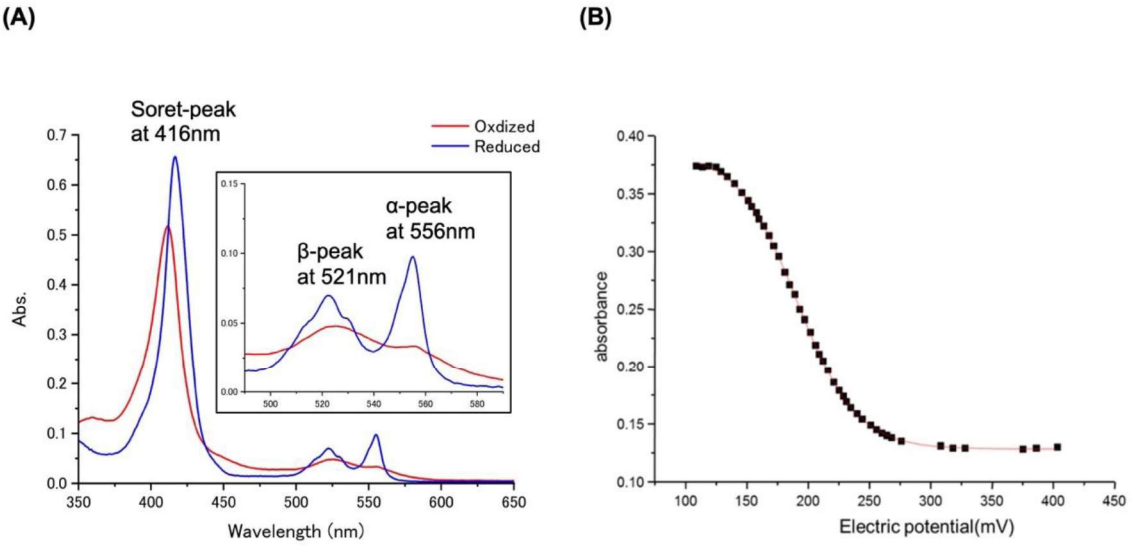


Figure 9. Biochemical properties of cyt *c*-556$_{sol}$

(A) Absorption spectra of cyt *c*-556$_{sol}$ in oxidized (red line) and ascorbate-reduced states (blue line). The α- an β-regions were enlarged in the inset. (B) Redox titration curve of cyt *c*-556$_{sol}$. The titration curve was obtained by plotting the absorbance at 556 nm against the ambient redox potentials. The fitting curve is shown by red line.

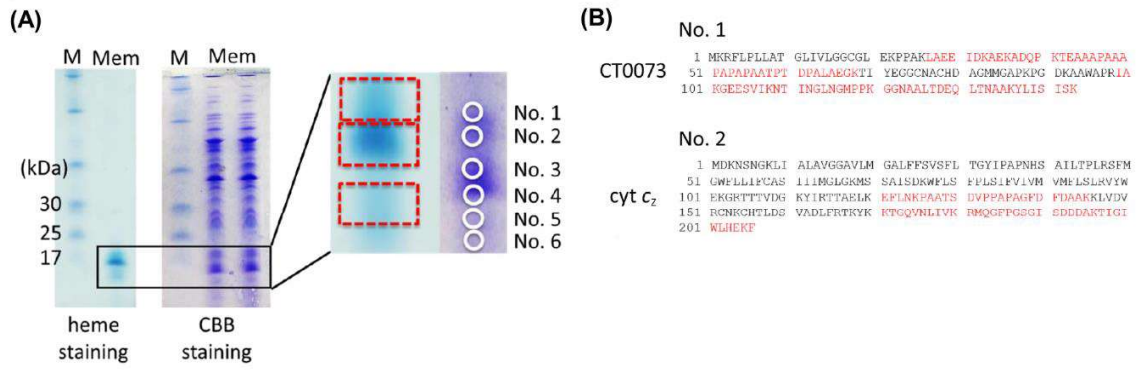


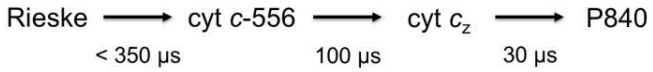
Figure 10. SDS-PAGE and LC-MS/MS analyses of membrane fraction

(A) SDS-PAGE analysis of membrane-bound *c*-type cytochromes stained with TMBZ and Coomassie brilliant blue. M, protein marker; Mem, chlorosome-depleted membranes from

C. tepidum deficient of the *CT0075* gene. Several heme-staining protein bands were detected around the 14-24 kDa region in molecular mass, as shown in an enlarged scale on the right side. The six bands marked by circles (No. 1-6) were excised and subjected to the nLC/MS/MS analysis and two bands of which, No.1 and 2, were found to be the CT0073 and cyt c_z, respectively. (B) Peptide fragments detected by mass spectrometry were 27–36 (1144.5975 kDa), 37–68 (2966.4985 kDa), 42–68 (2427.2281 kDa), 109–120 (1270.6340 kDa), 121–136 (1572-7743 kDa) and 137–143 (822.4851 kDa) for the CT0073 and 121–145 (2575.2595), 171–180 (1098.6761 kDa), 172–180 (970.5811 kDa), 172–181 (1126.6822 kDa), 182–196 (1523.6562 kDa) and 197–206 (1242.6761 kDa) for cyt c_z, resulting in the total protein sequence coverages of 61% and 30%, respectively. Sequence stretches, thus identified, are indicated by red letters in the bottom part of the figure.

Flash-induced absorption changes

An electron transfer scheme from the Rieske center to the RC P840 demonstrated previously, as follows [24]:



The E_m values of P840, cyt c_z and the Rieske center were reported to be +230 to +240, +170 to +180 mV (or +188 mV as determined as an isolated protein), and +130 to +150 mV, respectively. That of cyt *c*-556 was presently determined to be +190 mV (see Figure 9B) [39, 41-43]. After flash excitation, the oxidized $P840^+$ was re-reduced by a primary electron donor, cyt c_z, with a time constant of 30 µs ($t_{1/e}$ = 30 µs). Equilibration between cyts c_z and *c*-556 was immediately attained with $t_{1/e}$ = 100 µs. Therefore, the relative amounts of oxidized cyts c_z and *c*-556 were calculated to be approximately 0.45 : 0.55 by the Nernst equation (ΔE_m = RT/F ln K). Finally, both partially oxidized cyt c_z and cyt *c*-556 were reduced within 350 µs by the subsequent electron transfer reaction from the Rieske center [24, 27].

At the present time resolution of 1 ms, rapid absorption decreases were detected at 552 and 556 nm immediately after flash excitation (Figure 11), indicating that the redox equilibration between hemes c_z and *c*-556 was attained within 1 ms. Then, they were re-reduced slowly with $t_{1/2}$ = 50–100 ms by ascorbate added to the reaction medium and/or the back reaction from the terminal electron acceptor(s) in the RC, due to the presence of stigmatellin which inhibited the electron transfer reaction from the Rieske center by binding to the Q_o-site [44]. However, after the addition of excess cyt *c*-556_{sol}, the absorption intensity at 556 nm showed an additional increase of approximately 20-30% within the first several milliseconds ($t_{1/2}$ = ~ 3 ms) (Figure 11B). This implies that the additional cyt *c*-556_{sol} transferred electrons independently to cyt c_z with $t_{1/2}$ = ~ 3 ms. The finding also

implies that equilibration among three hemes, heme c_z in cyt c_z, heme *c*-556 in the intrinsic membrane-anchored cyt *c*-556, and heme *c*-556 in the exogenously added cyt *c*-556_{sol}, was also attained within this time range. None that the rest molecules of cyt *c*-556_{sol}, which did not directly donate electrons to cyt c_z, were out of this equilibration. The relative amounts of oxidized cyt c_z^+, cyt *c*-556^+, and cyt *c*-556_{sol}^+ were estimated to be 0.30 : 0.35 :0.35, respectively, using the Nernst equation, which exactly reflected a 20-30% increase in absorption intensity at 556 nm. In contrast, the absorption intensity at 552 nm hardly changed because of the isosbestic point between cyt c_z and cyt *c*-556 [24].

In the present study, the electron-transfer rate from cyt *c*-556_{sol} to cyt c_z in the membranes yielded a $t_{1/2}$ = ~ 3 ms at 10 μM cyt *c*-556_{sol}. It is rational to consider that its second-order rate constant would be approximately the close value to that reported for soluble cyt *c*-554 to cyt c_z (1.7×10^7 M^{-1} s^{-1}), because the latter electron transfer rate was almost the same ($t_{1/2}$ = ~ 3 ms) when measured under similar experimental conditions [27, 45].

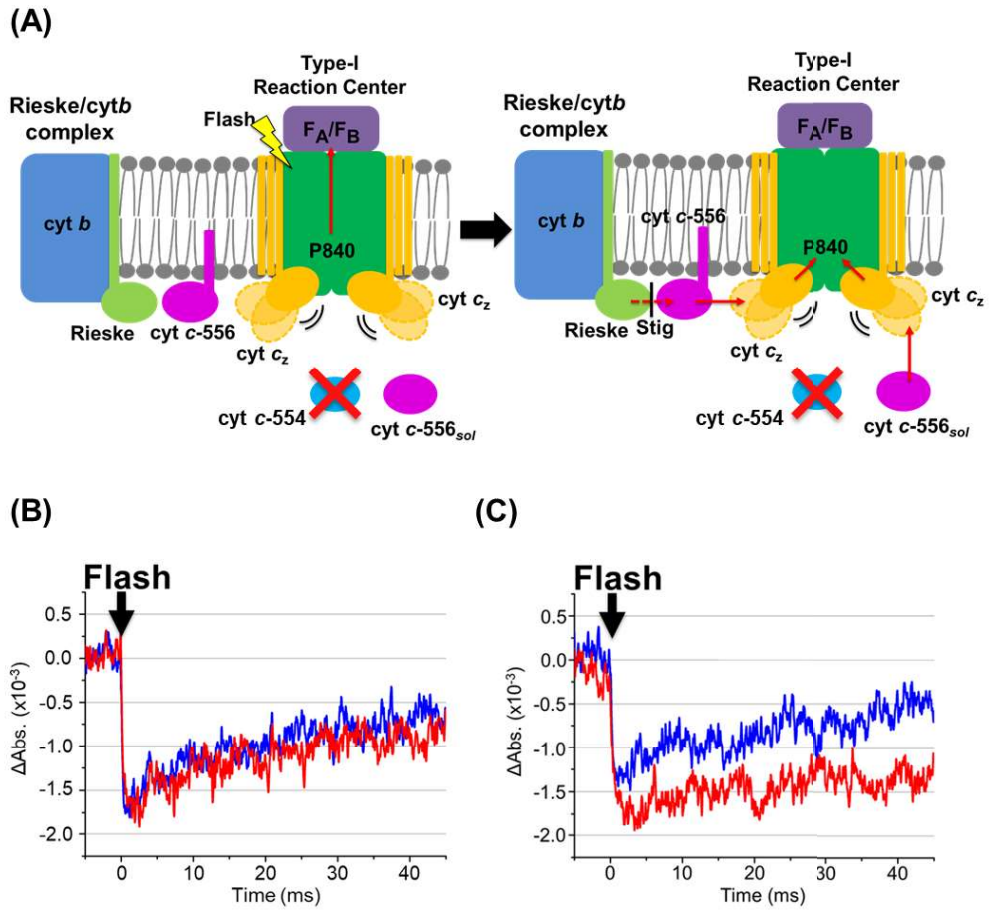


Figure 11. Flash-induced absorption changes in membrane

Flash-induced absorption changes were measured using chlorosome-depleted membranes of *C. tepidum* deficient of the *CT0075* gene with/without excess amount of the additional cyt *c*-556$_{sol}$. Electron transfer pathway after flash in membrane with cyt c-556$_{sol}$ are indicated with red arrow (A). Stig represents stigmatellin which inhibit electron transfer from the Rieske ISP. Absorption changes were measured at (B) 552nm and (C) 556nm in the presence of stigmatellin without any other addition (blue line) or after addition of the excess amount of the cyt *c*-556$_{sol}$ (red line).

Discussion

The presence of membrane-anchored cyt *c*-556 was initially suggested by the discovery of the *c*-type heme with α peak wavelength at 556 nm when the chemically reduced-minus-oxidized difference spectrum was measured in purified membranes from *C. tepidum*. Furthermore, measured redox potential was +190 mV, which was appropriate for accepting an electron from the Rieske ISP and transferring it to RC [24, 39, 40].

Measurements of flash-induced absorption changes also revealed the appearance of a clear shoulder at 556 nm along with a peak at 552 nm, which is responsible for cyt c_z oxidation in the presence of stigmatellin, an inhibitor of the Q_o-site of the cyt *bc* complex [44]. This was interpreted as evidence of the sequential electron transfer reaction from cyt *c*-556 to cyt c_z after flash excitation; that is, cyt *c*-556 seemed to serve as a cyt c_1-like protein [24, 25, 27]. In contrast, soluble cyt *c*-554 donated electrons directly to cyt c_z in the RC complex in an independent manner from cyt *c*-556 [27]; cyt *c*-554 did not act like a shuttle-like electron carrier between menaquinol:cyt *c* oxidoreductase (cyt *bc* complex) and the P840 RC complex, as seen in the case of cyt c_2 in purple bacteria [46]. These are seemed to be due to differences in the intermolecular interactions of cyt *c*-556 and cyt *c*-554. Therefore, structures of cyt *c*-556_{sol} and cyt *c*-554 was compared to verify it in Chapter II.

The reconstitution experiment showed that cyt *c*-556_{sol} efficiently donated electrons to cyt c_z in this study (Figure 11). The finding supports the view that the protein encoded by the *CT0073* gene corresponds to the membrane-anchored cyt *c*-556. It was also supported by the result of nLC/MS/MS analysis that demonstrated expression of CT0073 in

plasma membrane of *C. tepidum*. In addition, NMR measurements provided firm evidence for the direct interaction between cyt *c*-556$_{sol}$ and Rieske$_{sol}$ as described in Chapter IV. Therefore, I conclude that CT0073 is definitely the membrane-anchored cyt *c*-556.

Chapter II. Structural analyses of cyt *c*-556$_{sol}$

Introduction

Membrane-anchored cyt *c*-556 transfer an electron efficiently between the Rieske/cyt*b* complex and RC. However, rate of electron transfer between cyt *c*-556$_{sol}$ and cyt c_z was lower than it between membrane-anchored cyt *c*-556 and cyt c_z and it between soluble cyt *c*-554 and cyt c_z. Besides, soluble cyt *c*-554 is supposed not to conduct electron transfer between the Rieske/cyt*b* complex and RC as soluble cytochromes *c* in cyanobacteria and purple bacteria which transfer an electron from cyt *bc* complex to RC or PSI. These suggest there are differences in the interactions formed with cyt c_z in electron transfer reaction of membrane-anchored cyt *c*-556, cyt *c*-556$_{sol}$ and cyt *c*-554. Their structural information is essential to discuss it, however, the 3D-structure of cyt *c*-556 has not been determined while it of cyt *c*-554 and cyt c_z were determined [47, 48].

Therefore, I performed X-ray crystallography to determine the 3D-structure of cyt *c*-556$_{sol}$. In order to verify structural similarities and differences, 3D-structure of cyt *c*-556$_{sol}$ was compared with structures of other *c*-type cytochromes including cyt *c*-554. In this chapter, I mainly showed the structural differences of cyt *c*-556$_{sol}$ and cyt *c*-554. The differences in the electron transfer mechanisms of these cytochromes and Rieske ISP is discussed in Chapter IV.

Materials and Methods

Preparation of cyt *c*-556$_{sol}$

Cyt *c*-556$_{sol}$ was purified as described in Chapter I.

Crystallization of cyt c-556$_{sol}$

The purified cyt *c*-556$_{sol}$ was concentrated to 30 mg ml^{-1}. Crystallization was carried out using hanging-drop vapor-diffusion method at 293 K. Each drop consisted of 1 μl of protein solution and 1 μl of the reservoir solution. Initial trials were performed using the commercially available sparse-matrix screening kits Crystal Screens I and II, and PEG/Ion Screen (Hampton Research, Aliso Viejo, CA, USA). The initial conditions that produced crystals were optimized by varying the concentrations of protein, precipitants, buffer systems, and pH. The crystallization conditions finally established consisted of a protein solution of 30 mg ml^{-1} in 20mM Tris-HCl (pH 8.0) containing 150 mM NaCl and a reservoir solution consisting of 0.1 M sodium acetate trihydrate pH4.4 and 1.8 M ammonium sulfate. The crystals were soaked in a cryoprotectant solution containing 0.1 M sodium acetate pH4.6, 2.0M ammonium sulfate and 20% (v/v) glycerol for ten seconds and then flash-cooled at 100 K.

X-ray diffraction experiment and structure determination of cyt *c*-556$_{sol}$

Diffraction data were collected at 100 K using a synchrotron radiation beam at the SPring-8 BL44XU synchrotron beamline at the Japan Synchrotron Radiation Research Institute (JASRI, Hyogo, Japan). Complete data set was collected from a single crystal. The diffraction data were processed and scaled using the HKL-2000 program package [49]. The crystal structure of cyt *c*-556$_{sol}$ was determined by the single anomalous dispersion (SAD)

method using anomalous signals from the heme iron. The structure was refined using PHENIX, Refmac5 and COOT [50-52]. The final structure included 79 (Ala45-Lys143) residues excluding the plasmid-derived Met and original N-terminal moiety of a membrane-anchor domain could be determined.

Results

Crystallization and structure determination of cyt *c*-556$_{sol}$

Cyt *c*-556$_{sol}$ protein was highly purified by gel filtration chromatography and confirmed to have sufficient purity for crystallization by SDS-PAGE (Figure 12A). Crystals of cyt *c*-556$_{sol}$ were obtained by hanging-drop vapor diffusion method at 293K. A hanging drop was prepared by mixing equal volumes of protein solution and reservoir solution containing 0.1 M sodium acetate trihydrate (pH4.4) and 1.8M ammonium sulfate. The dimensions of typical crystals were approximately 0.3 μm × 0.3μm × 0.3μm (Figure 12B). For Cryoprotection, the crystals were transferred to a solution containing 0.1M sodium acetate (pH4.6), 2.0M ammonium sulfate and 20% (v/v) glycerol.

Data for Fe-SAD phasing were collected at 100K on beamline BL44XU at SPring-8 (JASRI). These crystals diffracted up to 1.65 Å resolution (Figure 12C) and belong to space group $P6_422$ with unit-cell parameters a = 85.02 Å, b = 85.02 Å, c = 123.93 Å, $\alpha = \beta = 90°$, and $\gamma = 120°$. The diffraction data were processed and scaled using the program HKL-2000 [49]. The initial phase was determined by Fe-SAD method with the program AutoSol in PHENIX program suite at 1.65 Å resolution [53, 54] (Figure 12D). Cyt *c*-556$_{sol}$ had single iron atom in heme *c*. The initial electron density map revealed most of the main chains and side chains. Molecule and crystallographic asymmetric unit contained two molecules of cyt *c*-556$_{sol}$. The initial phase obtained by SAD was transferred to native data for refinement. The structure model was manually built using the program COOT in CCP4 [52], and refined using REFMAC5 in CCP4 and PHENIX refine [50, 51, 53] . The statistics for the data collection and refinement are presented in Table 1. The whole structures of two molecules in crystallographic asymmetric unit are similar (RMSD of 0.4), with slight differences in the terminus.

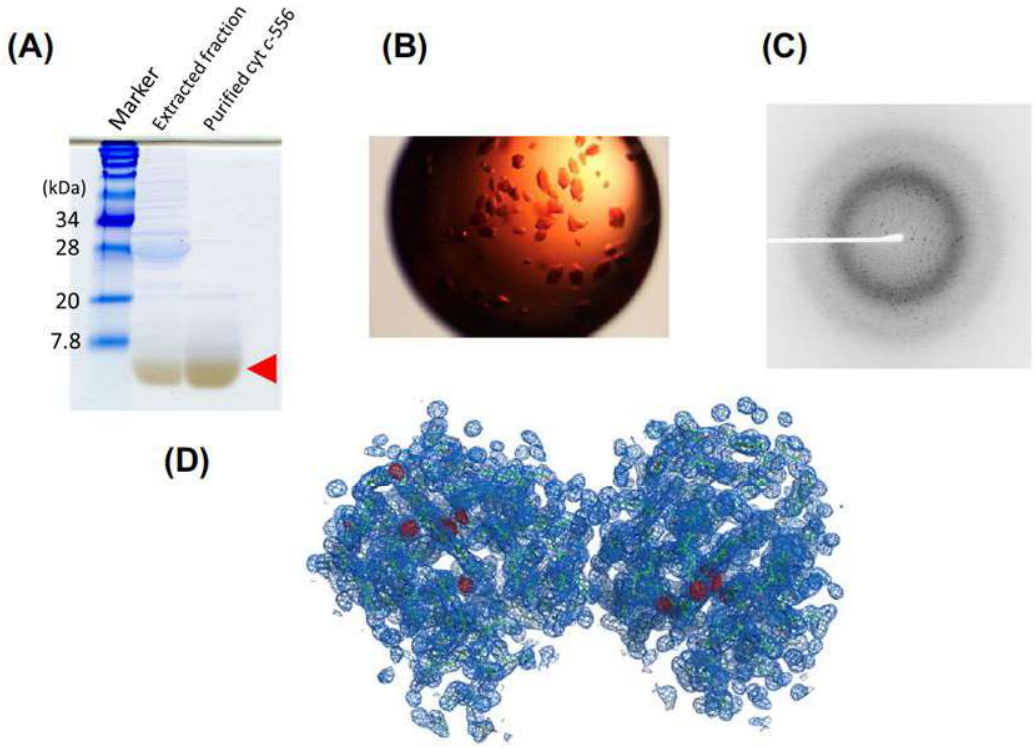


Figure 12. X-ray crystallography of cyt *c*-556$_{sol}$

(A) SDS-PAGE analysis of the purified cyt *c*-556$_{sol}$. The extracted fraction by osmotic shock was applied to gel filtration chromatography to obtain the purified cyt *c*-556$_{sol}$. The protein band of cyt *c*-556$_{sol}$ showed a brown color derived from heme *c* due to its high concentration. (B) Crystals of cyt *c*-556$_{sol}$ formed under the condition with 0.1 M sodium acetate trihydrate pH 4.4, 1.8 M ammonium sulfate. (C) X-ray diffraction pattern of cyt *c*-556$_{sol}$ obtained with BL44XU at SPring-8. (D) Electron density map of cyt *c*-556$_{sol}$ calculated with Phenix.

Table 1. Crystallographic data and refinement statistics for cyt *c*-556$_{sol}$

	cyt *c* -556$_{sol}$	
	native	**SAD**
Crystallographic data		
X-ray source	SPring-8 BL44XU	SPring-8 BL44XU
Wavelength (Å)	0.90000	1.70000
space group	$P6_422$	$P6_422$
Unit cell parameters		
a (Å)	85.02	85.02
b (Å)	85.02	85.02
c (Å)	123.93	123.93
α (deg)	90	90
β (deg)	90	90
γ (deg)	120	120
Resolution range (Å)	50.00-1.65 (1.68-1.65)[a]	50.00-1.90 (1.93-1.90)[a]
Total no. of reflections	675134	435345
No. of unique reflections	32195 (3113)	21625 (1045)
Completeness (%)	99.9 (100)[a]	100 (100)[a]
R_{merge} (I) (%)[b]	0.056 (0.240)[a]	0.092 (0.503)[a]
I / σ	95.6 (23)[a]	47.1 (4.8)[a]
Redundancy	20.7 (21.2)[a]	20.2 (19.5)[a]
Refinement statistics		
Resolution range (Å)	36.82-1.65 (1.71-1.65)	—
Reflections used in refinement	32194 (3113)	—
R_{work}[c]	0.153	—
R_{free}[d]	0.173	—
Mean B value (Å^2)	20.115	—
No. of non-hydrogen atoms		
protein	1130	—
heme / metal cluster / ion	106	—
water	192	—
RMSD from ideal values		
bond length (Å)	0.033	—
bond angles (deg)	3.306	—

[a] Values in parentheses are for the highest resolution shells. [b] $R_{merge}(I) = \Sigma|I(k) - \langle I \rangle|/\Sigma I(k)$ representing the k value of an intensity measurement of a reflection, $\langle I \rangle$ the mean intensity value of that reflection, and Σ the summation across all measurements. [c] R-factor = $\Sigma||F_{obs}(hkl)| - |F_{calc}(hkl)||/\Sigma|F_{obs}(hkl)|$. [d] R_{free} is the R-factor computed for the test set of reflections that were omitted from the refinement process.

Overall structure of cyt *c*-556$_{sol}$

The scaffold of the molecule was formed by four α-helices holding the heme prosthetic group without any β-sheets (Figure 13A). Its overall structure followed the topology of typical class I *c*-type cytochromes [55]. According to the criteria proposed by Kabsch and Sander [56], Gly72 divides the N-terminal helix into two parts. The polypeptide consists of α1 (residues 66-71), α1' (residues 75-79), α2 (residues 92-100), α3 (residues 103-112), and α4 (residues 128-140) helices. The iron-ion of heme *c* is coordinated to His79Nε2 of the α1' helix and Met117S of the loop region between the α3 and α4 helices as the fifth and sixth ligands, respectively (Figure 13B). In addition, two vinyl groups of heme *c* are covalently bonded to Cys75Sγ and Cys78 Sγ of the α1' helix. The heme prosthetic group is almost entirely buried within a hydrophobic crevice, leaving only a slight edge of the heme ring II and the propionate sidechain of ring III exposed to solvent. These structural features of cyt *c*-556$_{sol}$ are similar to those of other class I *c*-type cytochromes as mentioned in next section.

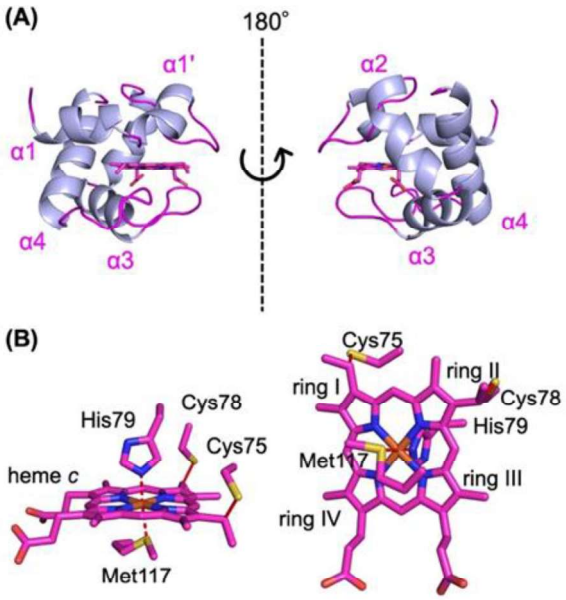


Figure 13. 3D-structure of cyt *c*-556$_{sol}$

(A) Ribbon representation of cyt *c*-556$_{sol}$. The α -helices are shown in light blue. (B) Close-up views of heme *c* from the horizontal (left) and the sixth ligand sides (right). Coordinate bonds between heme *c* and ligands are shown as red dotted lines and thioether bonds red solid lines. These figures were created with The PyMOL Molecular Graphics System, Version 2.0.

Structural similarities to other cytochromes *c*

The overall structural comparisons of the presently determined *C. tepidum* cyt *c*-556$_{sol}$ using the Dali server [57] revealed extensive similarities to those of cyt c_5 from the nitrogen-fixing soil bacterium *Azotobactor vinelandii* (PDBID: 1CC5, Z-score of 11.9) [58], cyt *c*-551 from the halophilic purple photosynthetic bacterium *Halorhodospira halophila* (PDBID: 1GKS, Z-score of 11.5) [59], cyt c_6 from the cyanobacterium *Phormidium laminosum* (PDBID: 2V08, Z-score of 9.7) [60], and cyt *c*-554 from a green sulfur bacterium *C. tepidum* (PDBID: 4J20, Z-score of 15.5) [47] (see Figure 14). All these cyts *c* contained four α-helices in common without any β-sheets, as expected from the structural characteristics of class I *c*-type cyts, although the N-terminal helix, α1', was missing in the case of cyt c_5. The loop structures also seemed to be slightly different among them; the loop between α1 and α1' in cyt *c*-551 was longer than others, and the loops between α3 and α4 in both cyt *c*-551 and cyt c_6 were bent and protruding in different directions. The additional 3_{10}-helices were found between α2 and α3 in both cyt *c*-551 and cyt c_6, but each was in a spatially different location.

Root-mean-square deviation (RMSD) values were also calculated using Pairwise structure comparison on the Dali server to estimate the degree of structural deviation from each other [57]. Interestingly, the structure of *C. tepidum* cyt *c*-556$_{sol}$ exhibited the highest similarity to cyt *c*-554 with an RMSD value of 1.0. In both cytochromes, the heme groups are exposed to their surfaces at the sides of pyrrole rings II and III. However, the longer loop connecting the α3 and α4 helices in cyt *c*-554, compared to that in cyt *c*-556, covers most of the pyrrole ring III, leaving only the oxygen atom of propionate exposed to the solvent (Figure 14E). Because both cyts *c* donate electrons directly to the P840 in the photosynthetic RC independently; the cyt *c*-556 serves as a membrane-anchored mediator from the Rieske/cyt*b* complex to the P840 [25, 27], while cyt *c*-554 does as a water-soluble

one from the Sox-related enzymes in a periplasmic space [45, 61-64]. Therefore, the different protein surface natures around the heme-exposed edges between cyt *c*-556 and cyt *c*-554 might be involved in the reaction specificity to the P840.

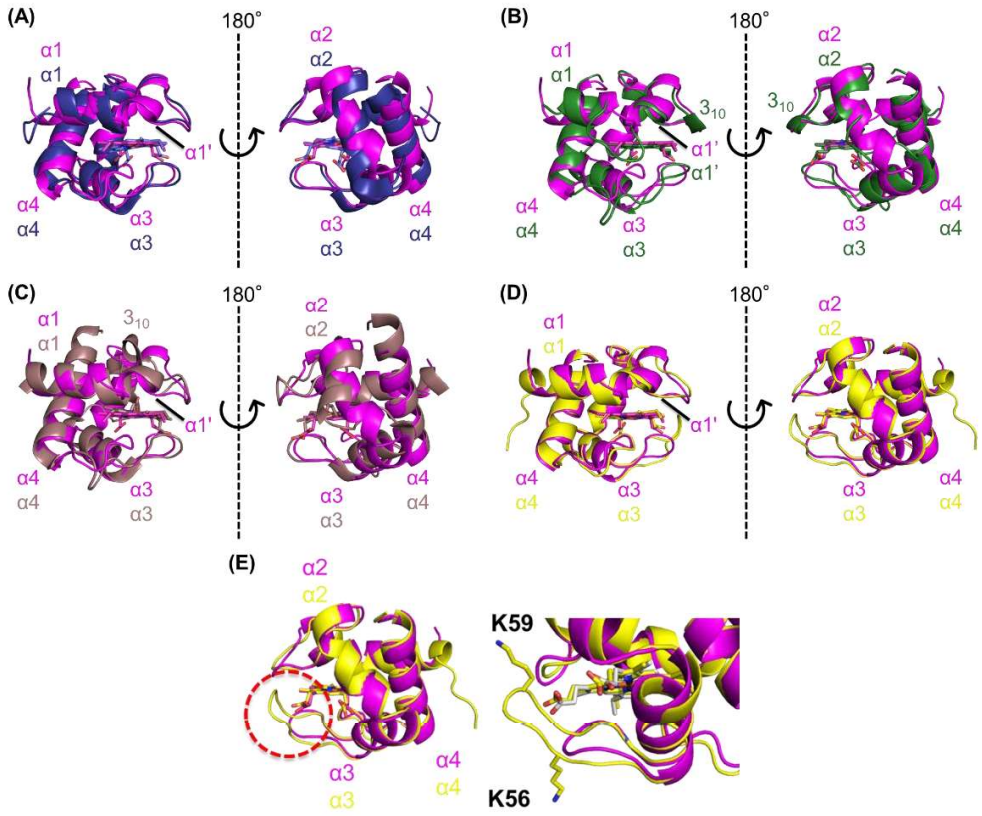


Figure 14. Structure comparison of cyt *c*-556$_{sol}$ with cytochromes *c*

Structure comparison of the *C. tepidum* cyt *c*-556 (magenta) with (A) cyt c_5 from *Azotobactor vinelandii* (dark blue; PDBID 1CC5), (B) cyt *c*-551 from *Halorhodospira halophila* (dark green; PDBID 1GKS), (C) cyt c_6 from *Phormidium laminosum* (light blown; PDBID 2V08) and (D) cyt *c*-554 from *C. tepidum* (yellow; PDBID 4J20) by superposition of their polypeptide chains with PyMOL. The structures in left of each figure are shown from vinyl-group side and those in right are shown from propionate-group side. (E) Structural differences between cyt *c*-556$_{sol}$ and cyt *c*-554.

Surface properties of cytochromes *c*

Most of the protein surface area of cyt *c*-556 was covered with charged and polar residues (Figure 15), and the heme group was largely embedded in the hydrophobic interior. The only parts that are solvent accessible in heme are the edges at the sides of the pyrrole ring II in vinyl-group side and III in propionate-group side. The protein surface around the pyrrole ring II edge consists of several non-polar residues and is relatively hydrophobic, as seen in cyt *c*-554. The hydrophobic patch is considered an electron transfer gate, and the hydrophilic area around the patch is responsible for complex formation, as reported in detail for water-soluble cyt c_6 functioning as an electron donor in photosystem I and cyt c_2 in the RC of purple bacteria [65, 66].

Conversely, the protein surface around the pyrrole ring III edge is a less positively charged and rather non-polar area, compared to that in cyt *c*-554, especially in the portion flanking pyrrole ring II in vinyl-group side (Figure 16). As discussed later, this non-polar region is important for the formation of electron transfer complex with the Rieske ISP, as determined from the NMR experimental data demonstrated in Chapter IV. Two positively charged residues (Lys56 and Lys59) in cyt *c*-554, one (Lys56), which resides in a unique long loop between the α3 and α4 helices, would therefore be involved in its specific interaction with cyt c_z of the P840 RC complex. Cyt *c*-554 has been demonstrated to donate electrons to cyt c_z from the sulfur oxidation pathway and not to mediate the electron transfer reaction between the Rieske/cyt*b* complex and the P840 RC complex [27].

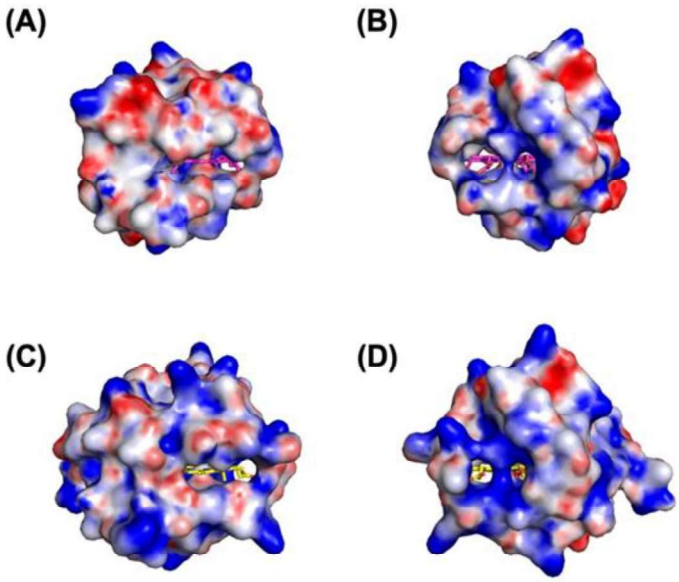


Figure 15. Electrostatic properties of the surfaces of cyt *c*-556$_{sol}$ and cyt *c*-554

The distribution is colored according to the electrostatic potential from -10K_BT (red) to +10 K_BT (blue) calculated with PyMOL APBS (the Adaptive Poisson-Boltzmann Solver) Tools [67, 68]. (A) and (B) represent the surfaces of the vinyl- and propionate-group sides, respectively, of heme *c* (shown in magenta) in cyt *c*-556. (C) and (D) represent those of heme *c* (shown in yellow) in cyt *c*-554 in the same way.

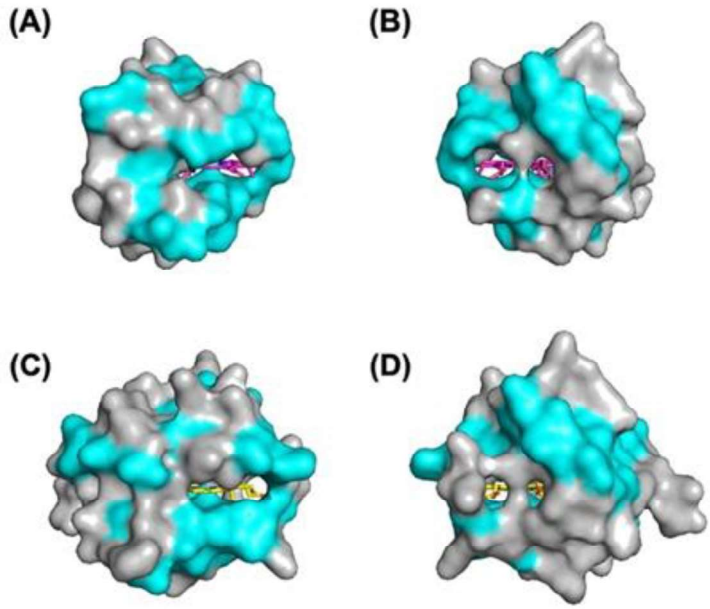


Figure 16. Non-polar amino acid residues in cyt *c*-556$_{sol}$ and cyt *c*-554

The non-polar amino acid residues in cyts *c*-556$_{sol}$ and *c*-554 were colored by cyan. (A) and (B) represent the surfaces of the vinyl- and propionate-group sides, respectively, of heme *c* (shown in magenta) in cyt *c*-556$_{sol}$. (C) and (D) represent those of heme *c* (shown in yellow) in cyt *c*-554 in a same way.

Discussion

Cyt *c*-556 was supposed to accept an electron from Rieske ISP in the Rieske/cyt*b* complex, that is, it would function as cyt c_1 in cyt bc_1 complex or cyt *f* in cyt b_6f complex. Green sulfur bacteria belong to green clade, and structures of cyt *b* and Rieske ISP in the Rieske/cyt*b* complex were thought to be similar to those of cyt b_6/subunit IV and Rieske ISP in cyt b_6f complex of cyanobacteria, respectively [15]. However, the results of X-ray crystallography showed that cyt *c*-556_{sol} was composed with α-helices as cyt c_1 while cyt *f* was composed with β -sheets. This structural property is corresponded to it of soluble cytochromes *c* which function in electron transport chain. Although a little structural difference was observer in comparison of these structures, cyt *c*-556_{sol} contained four α-helices without any β -sheets as other class I *c*-type cytochromes. In particular, structure of cyt *c*-556_{sol} was remarkably similar to it of soluble cyt *c*-554 which also function in electron transport chain in *C. tepidum*. The protein surface around of pyrrole ring II which is one of the solvent accessible parts in heme *c* consists of several non-polar residues, that is relatively hydrophobic as cyt *c*-554. This hydrophobic region is thought to be an electron transfer gate, while hydrophilic region around it functions in formation of complex. This is also consistent with the previous report of soluble cyt c_6 in cyanobacteria and cyt c_2 in purple bacteria [65, 66].

The process of protein-protein interaction and subsequent complex formation in solution can be understood by a two-step model [69, 70]. In the first step, long-range electrostatic interactions steer dynamic encounter to form a loose-binding complex for a short period of time. Then, in the second step, the proteins glide on their surface to form well-defined single-orientation complex by hydrogen bonds and non-polar interactions in the positions optimal for electron transfer, and subsequently electrons are transferred.

Because of that, cyt *c*-556$_{sol}$ would have to approach by long-range electrostatic interactions and form loose complex in order to transfer an electron to cyt c_z. In this study, it was revealed that the major structural difference between cyt *c*-556$_{sol}$ and cyt *c*-554 was the longer loop connecting the α3 and α4 helices in cyt *c*-554. This loop contains two lysine residues, which can form electrostatic interactions with cyt c_z. Conversely, it is improbable that cyt *c*-556$_{sol}$ form similar electrostatic interactions as cyt *c*-554 because it does not contain this loop. The lower rate of electron transfer between cyt *c*-556$_{sol}$ and cyt c_z may be due to the inability of cyt *c*-556$_{sol}$ to transfer an electron to cyt c_z by two-step model resulting in electron transfer reaction conducted by diffusion. In the membrane of *C. tepidum*, cyt *c*-556 is anchored to the membrane by fatty acid [25]. Therefore, it is located closer to RC than cyt *c*-554 which diffuses in the periplasmic space. That is, cyt *c*-556 would form a loose complex with cyt c_z by moving of their soluble domains, while cyt *c*-554 would forms with cyt c_z by electrostatic interactions (Figure 17).

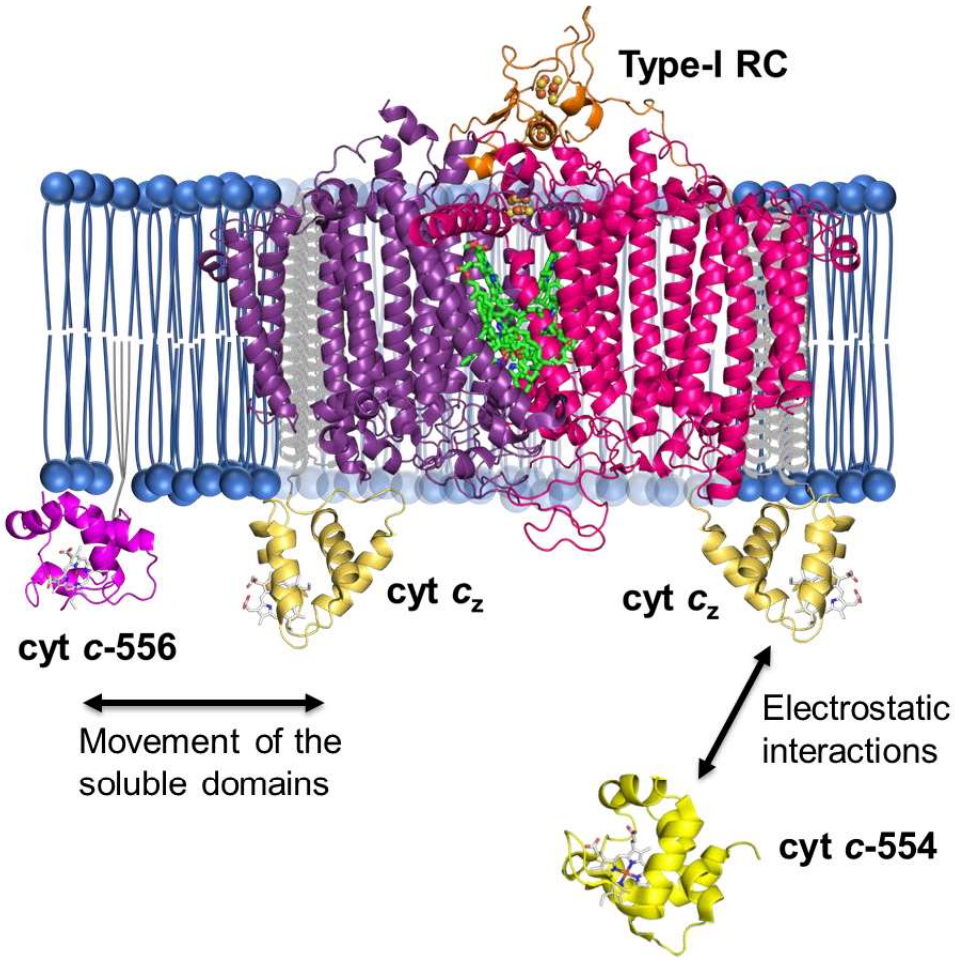


Figure 17. Interaction scheme of cyt c_z with cyt *c*-556 and cyt *c*-554

Cyt *c*-556 in membrane and soluble cyt *c*-554 (PDBID: 4J20) [47] would form loose complex with cyt c_z (PDBID: 3A9F) [42] in the RC (PDBID: 8GWA) [71] to transfer electron in different way.

Chapter III. Structural analyses of the Rieske$_{sol}$

Introduction

In the cyt *bc* complex, the Rieske ISP receives an electron from quinol bound to Q_o site in cyt *b* and transfer it to cyt c_1 or cyt f. The Rieske ISP in the Rieske/cyt*b* complex also transfer an electron to cyt *c*-556. Cyt bc_1 and cyt b_6f complex are homodimeric complexes. Quinols bind to each monomer unit and electrons are transferred to each *c*-type cytochrome. Electron transfer pathway of cyt *bc* complex is unique. The Rieske ISP is bound in one monomer by single transmembrane helix, while soluble domain containing [2Fe-2S]-cluster is located in the other monomer [72, 73]. Electron transfer from quinol to *c*-type cytochrome in one monomer is not conducted by the Rieske ISP in the same monomer but by it in the other monomer (Figure 18). Therefore, cyt *bc* complex cannot transfer electrons in monomer structure, and dimeric structure enable the complex to transfer electrons.

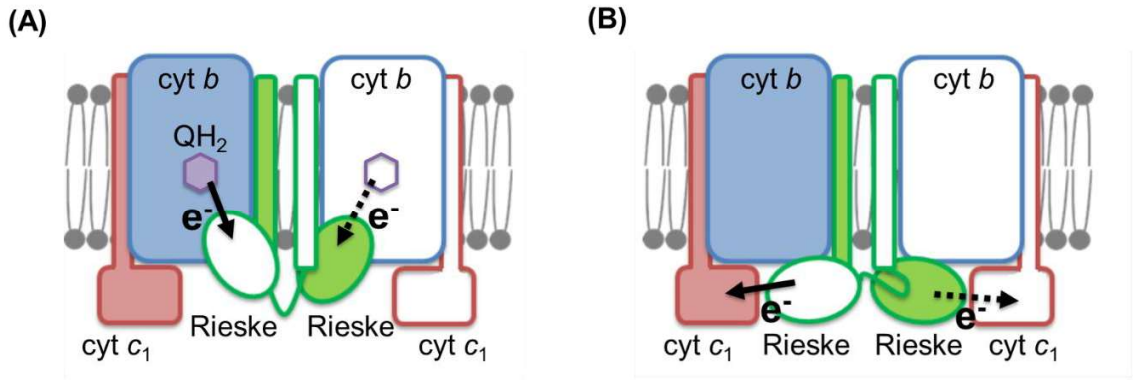


Figure 18. Electron transfer pathway in cyt bc_1 complex

Black solid arrow and black dotted arrow present electron flow in left and right monomer unit, respectively. Proteins filled in each color belong to left monomer unit. (A) Quinol in left unit transfers an electron to the Rieske ISP in right unit (dotted arrow). In right unit, the Rieske ISP in left unit receives an electron from quinol (solid arrow). (B) The Rieske ISP in left unit transfers an electron to cyt c_1 in right unit (dotted arrow). The Rieske ISP in right unit does to cyt c_1 in left unit (solid arrow)

The Rieske ISP is composed with three domains, transmembrane, linker and soluble domains (Figure 19). [2Fe-2S]-cluster for electron transfer is located in the soluble domain. In order to electron transfer, this cluster has to be moved to the vicinity of Q_o site and heme *c* in *c*-type cytochrome. Flexible linker domain enables to move the soluble domain for shuttling electrons between Q_o site and *c*-type cytochrome. In this chapter, I showed the results of structural determination of the soluble domain of Rieske ISP ($Rieske_{sol}$) for interaction analysis and structural comparison with the soluble domains of Rieske ISP in other species.

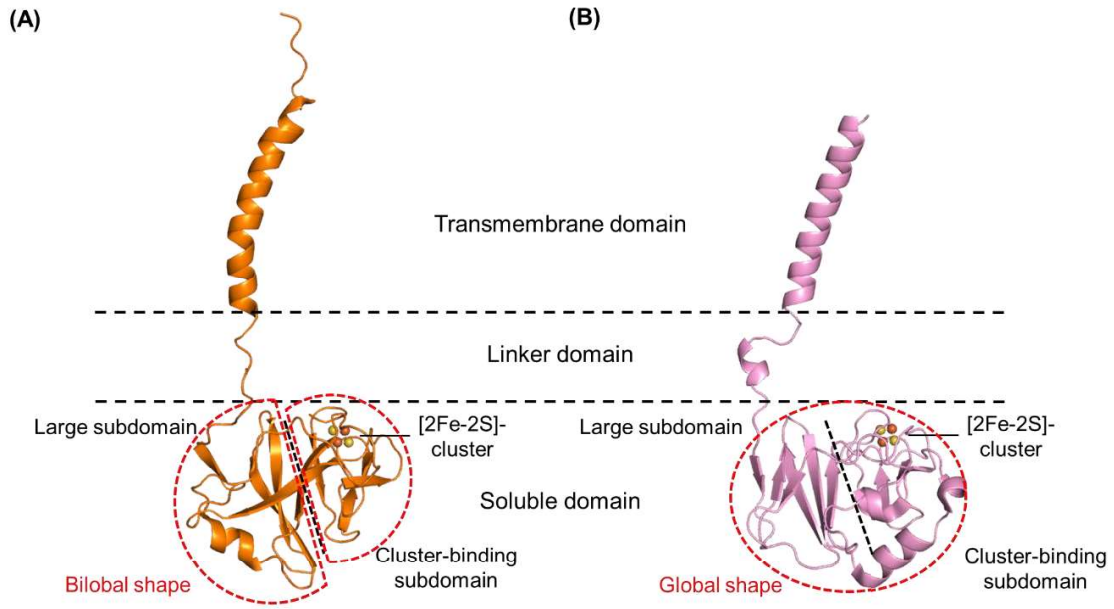


Figure 19. Domains of the Rieske ISP

Structures of the Rieske ISP from (A) cyt b_6f complex from cyanobacterium *Mastigocladus laminosus* (PDBID: 1VF5) [11] and (B) cyt bc_1 complex from α-proteobacterium *Paracoccus denitrificans* (PDBID: 2YIU) [74]. Domains and subdomains are divided by black dotted lines. Red dotted line represents the shapes of soluble domain.

Materials and Methods

Construction of truncated Rieske ISP (PetC) expression plasmid

A fragment from 226 to 543 bp in the *petC* gene encoding the soluble domain of the Rieske ISP from Ala26 to Ala181 was amplified by PCR using the following primer sets: (forward) 5′-AAACATATGGCCAAAAAGATCAAGATCGTC-3′ and (reverse) 5′-AAAAAGCTTCGCTATCGAAACAACAATCTTA-3′ (restriction site underlined). Primers corresponding to the 5′ ends were designed to introduce an NdeI site in the forward primer and a HindIII site in the reverse primer. The PCR product was digested with NdeI/HindIII restriction enzymes (Toyobo Inc., Osaka, Japan), subcloned into pUC118, and the sequence was confirmed. Following digestion of pUC118-*petC*$_{sol}$ with NdeI/HindIII, the DNA fragment containing the *petC*$_{sol}$ gene was ligated into the pET21a(+) vector (Novagen, Madison, WI, USA), and pET21a(+)-*petC*$_{sol}$-His6 was generated.

Overexpression and purification of the Rieske$_{sol}$

The pET21a(+)-*petC*$_{sol}$-His6 expression vector was transformed into *E. coli* C41(DE3) cells harboring the plasmid pRKISC, which contains the *isc* gene cluster involved in the assembly of the iron-sulfur cluster [75]. The cells were cultivated at 37 °C in Terrific broth containing 100 μg ml^{-1} ampicillin and 10 μg ml^{-1} tetracycline to an absorbance of approximately 0.3 at 600 nm. The expression of the Rieske$_{sol}$ in pET21a(+)-*petC*$_{sol}$-His6 vector was induced with 0.1 mM IPTG after supplementation with 0.1 mg ml^{-1} ferric ammonium citrate, and the cells were grown for 20 h at 25 °C.

The cells were harvested by centrifugation, resuspended in 50 mM Tris-HCl buffer (pH 7.5) containing 10% (w/v) glycerol, 4 mg lysozyme and 400 mM phenylmethyl

sulfonyl fluoride, and disrupted by sonication. After removal of undisrupted cells and insoluble matters by centrifugation, the supernatant was applied to Ni^{2+}-*NTA* affinity column (QIAGEN, Carlsbad, CA, USA) equilibrated with 50mM Tris-HCl (pH8.0) and 300 mM NaCl. The C-terminal His-tagged Rieske$_{sol}$ was eluted with 50 mM Tris-HCl (pH8.0), 300 mM NaCl and 250 mM imidazole, and further purified by gel filtration chromatography using HiLoad 26/600 Superdex 75 pg resin (GE Healthcare) equilibrated with 20 mM Tris-HCl pH7.5 and 50 mM NaCl.

Overexpression of the SeMet-Rieske$_{sol}$

For Se-SAD analysis, Met139 in the Rieske$_{sol}$ was substituted with selenomethionine (SeMet), according to the method previously described [76, 77]. Since it was unknown whether *E. coli* B834(DE3) cells can harbor the pRKISC, cells harboring only the pET21a(+)-*petC*$_{sol}$-His6 vector were grown at 37 °C in LeMaster medium containing 50 μg ml^{-1} ampicillin to an absorbance of approximately 0.3 at 600 nm. The expression of SeMet-Rieske$_{sol}$ was induced with 0.1 mM IPTG, and the cells were grown for 19 h at 20 °C. SeMet-Rieske$_{sol}$ was purified in the same methods of the Rieske$_{sol}$.

Crystallization of the Rieske$_{sol}$

The purified Rieske$_{sol}$ was concentrated to 45 mg ml^{-1} with ultrafiltration of Vivaspin 5 k (Sartorius, Germany). Crystallization was performed using the hanging-drop vapor-diffusion method at 293K, each drop consisting of 1 μl of protein solution and 1 μl of the reservoir solution. Initial trials were performed using the commercially available sparse-matrix screening kits Crystal Screens I and II (Hampton Research), and Wizard I and II (Emerald Biostructures). The initial conditions that produced crystals were optimized by varying the concentrations of protein, precipitants and buffer systems and the pH. The

crystallization conditions finally established consisted of a protein solution of 10 mg ml^{-1} in 20 mM Tris–HCl pH 7.5 containing 50 mM NaCl and a reservoir solution consisting of 0.2M ammonium sulfate, 0.1M ammonium citrate (pH5.0), 28% (w/v) polyethylene glycol 2,000. Although the X-ray diffraction data of the crystals were collected, their initial phase were not determined using the molecular replacement method. Therefore, I aimed to solve the structure using the SAD technique with selenium as the anomalous scattering atom. SeMet-Rieske$_{sol}$, thus obtained, was crystallized under conditions slightly different from that of the Rieske$_{sol}$: crystals were grown in drops containing a 1:1 mixture of protein (10 mg ml^{-1} in 20 mM Tris–HCl (pH 7.5) containing 50 mM NaCl) and a reservoir solution (0.2M ammonium sulfate, 0.1M ammonium citrate (pH5.0), 22% (w/v) Polyethylene Glycol 2,000, 10%(v/v) ethanol). Crystals were soaked in a reservoir solution containing 20% (v/v) ethanol and dipped into liquid nitrogen for cryo-protection. Crystals were soaked in a cryoprotectant solution containing 0.2M ammonium sulfate, 0.1M ammonium citrate (pH5.0), 22% (w/v) polyethylene glycol 2,000, 20%(v/v) ethanol for ten seconds and then flash-cooled at 100 K.

X-ray diffraction experiment and structure determination of SeMet-Rieske$_{sol}$

Diffraction data were collected at 100 K using a synchrotron radiation beam on BL44XU at SPring-8. Complete data set was collected from a single crystal. The diffraction data were processed and scaled using the HKL-2000 program package [49]. The crystal structure of Rieske$_{sol}$ was determined by SAD method using anomalous signals from the selenium ion in Se-labeled methionine. The structure was refined using Refmac5 and COOT [50-52]. The final structure was 110 residues long (Lys77-Ala186), including a part of the C-terminal His-tag (Lys182-Ala186).

Results

Crystallization and structure determination of SeMet-Rieske$_{sol}$

The SeMet-Rieske$_{sol}$ obtained after Ni^{2+}-*NTA* affinity column and subsequent gel filtration chromatography was confirmed to have sufficient purity for crystallization (Figure 20A). Crystals of SeMet-Rieske$_{sol}$ were obtained by hanging-drop vapor diffusion method at 293 K.A hanging drop was prepared by mixing equal volumes of protein solution and reservoir solution containing 0.1M ammonium citrate (pH 5.0), 0.2 M ammonium sulfate, 22% (w/v) polyethylene glycol 2,000 and 10% (v/v) ethanol. The crystal showed a truncated square pyramid shape with clear edges, and the dimensions were approximately 0.1 mm x 0.2 mm x 0.1 mm (Figure 20B). For Cryoprotection, the crystals were transferred to a solution containing the same buffer as crystallization buffer with 20% (v/v) ethanol. Data for Se-SAD phasing were collected at 100K on beamline BL44XU at SPring-8 (JASRI, Japan). These crystals diffracted up to 2.1 Å resolution (Figure 20C) and belong to space group *C*2 with unit-cell parameters a = 130.8 Å, b = 58.7 Å, c = 49.8 Å, $\alpha = \gamma = 90°$, and $\beta = 112.1°$. The diffraction data were processed and scaled using the program HKL-2000 [49]. The initial phase was determined by Se-SAD method with the program AutoSol in PHENIX program suite at 2.3 Å resolution [53, 54] (Figure 20D). The SeMet derivative protein had single SeMet residue and single site were found. The initial electron density map revealed most of the main chains and side chains. Molecule and crystallographic asymmetric unit contained two molecules of the Rieske$_{sol}$. The structure model was manually built using the program COOT in CCP4 [52], and refined using REFMAC5 in CCP4 [50, 51]. The statistics for data collection and refinement are presented in Table 2. The whole structures of two molecules in crystallographic asymmetric unit are similar (RMSD of 0.5), with slight differences in the terminus.

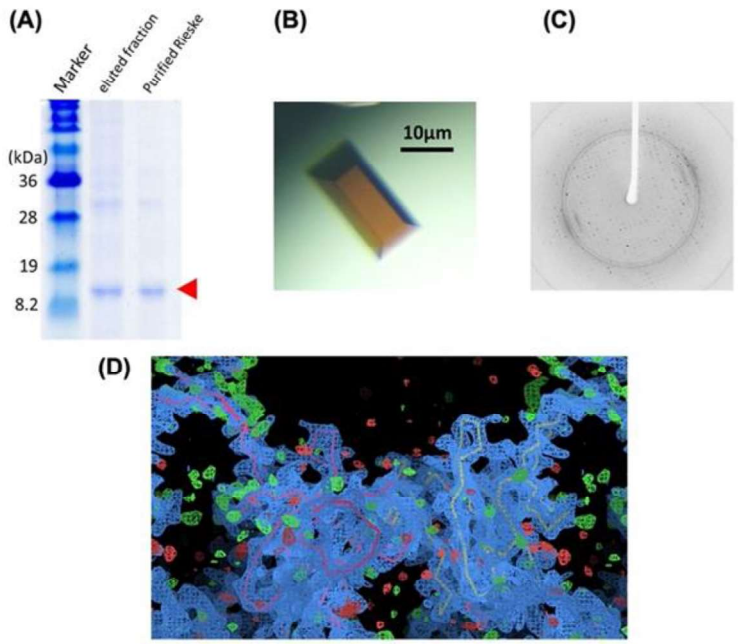


Figure 20. X-ray crystallography of the Rieske$_{sol}$

(A) SDS-PAGE analysis of the purified SeMet-Rieske$_{sol}$. The eluted fraction purified Rieske$_{sol}$ were obtained after Ni^{2+}-*NTA* affinity chromatography and gel filtration chromatography, respectively. Protein bands of the SeMet-Rieske$_{sol}$ were marked with red triangle. (B) Crystal of the SeMet-Rieske$_{sol}$ formed under the condition with 0.2M ammonium sulfate, 0.1M sodium acetate pH5.0 and 28% PEG2000. (C) X-ray diffraction pattern of the SeMet-Rieske$_{sol}$ obtained with BL44XU at SPring-8. (D) Electron density map of the SeMet-Rieske$_{sol}$ calculated with Phenix.

Table 2. Crystallographic data and refinement statistics for the Rieske$_{sol}$

	Rieske$_{sol}$ protein
	SAD
Crystallographic data	
X-ray source	SPring-8 BL44XU
Wavelength (Å)	0.97919
space group	$C2$
Unit cell parameters	
a (Å)	130.64
b (Å)	58.70
c (Å)	49.68
α (deg)	90
β (deg)	112.04
γ (deg)	90
Resolution range (Å)	60.55-2.13 (2.24-2.13)[a]
Total no. of reflections	74670
No. of unique reflections	35928 (5585)
Completeness (%)	99.8 (99.0)[a]
R_{merge} (I) (%)[b]	0.112 (0.604)[a]
I / σ	8.9 (2.7)[a]
Redundancy	7.4 (7.1)[a]
Refinement statistics	
Resolution range (Å)	60.55-2.30 (2.36-2.30)
Reflections used in refinement	15648 (1580)
R_{work}[c]	0.200
R_{free}[d]	0.241
Mean B value (Å^2)	55.524
No. of non-hydrogen atoms	
protein	1634
heme / metal cluster / ion	34
water	78
RMSD from ideal values	
bond length (Å)	0.021
bond angles (deg)	2.233

[a] Values in parentheses are for the highest resolution shells. [b] $R_{\mathrm{merge}}(I) = \Sigma|I(k) - \langle I \rangle|/\Sigma I(k)$ representing the k value of an intensity measurement of a reflection, $\langle I \rangle$ the mean intensity value of that reflection, and Σ the summation across all measurements. [c] R-factor = $\Sigma ||F_{\mathrm{obs}}(hkl)| - |F_{\mathrm{calc}}(hkl)|| / \Sigma |F_{\mathrm{obs}}(hkl)|$. [d] R_{free} is the R-factor computed for the test set of reflections that were omitted from the refinement process.

Overall structure of the soluble domain of the Rieske ISP

The soluble domain of Rieske ISP is divided in two subdomains, small cluster-binding subdomain and large subdomain (see Figure 19). Cluster-binding subdomain is formed with three loops, loop 1, loop 2 and Proline-loop, and [2Fe-2S]-cluster binds with two cysteine and two histidine residues in loop 1 and 2. Other two cysteine residues which are not ligands of cluster form a disulfide bond to stabilize the structure [78, 79]. These features are found in both cyt bc_1 and cyt b_6f complex, and structure of cluster-binding subdomain of these are similar. Conversely, structural differences were observed in the large domains between the Rieske ISP of the cyt bc_1 and b_6f complexes. The Rieske ISP in cyt bc_1 complex contains a loop with single α-helix in this subdomain which was not observed in the Rieske ISP in cyt b_6f complex. The soluble domain of Rieske ISP in cyt bc_1 complex is a global shape, whereas it in cyt b_6f complex is a bilobal shape [80].

The Rieske$_{sol}$ shows a globular elliptical molecular structure with dimensions of approximately 30 × 40 × 40 Å. The scaffold of the molecules is formed by three antiparallel β-sheets. Sheet 1 is formed by β-strands β1 (residues 82–88), β8 (residues 168–172) and β9 (residues 175–181), sheet 2 by β-strands β2 (residues 96–103), β3 (residues 106–113) and β4 (residues 116–121), and sheet 3 by β-strands β5 (residues 132–134), β6 (residues 138–141) and β7 (residues 146–149) (Figure 21A). The structure does not contain any α-helix in its scaffold as usually present in the Rieske ISPs so far determined, however, two 3_{10} helices (residues 90–92 and 135–137) are present between β1 and β2, and β5 and β6 instead.

The structure of Rieske$_{sol}$ can be divided into two subdomains as like other Rieske ISPs [81, 82]. One is a small cluster-binding subdomain that contains a [2Fe-2S] cluster constituted on a scaffold β-sheet 3 (β5–β7) along with ligand loops 1 and 2 and the proline loop. The other is a large subdomain that consists of β-sheet 1 (β1, β8, β9) and 2 (β2–β4).

Each subdomain appears to constitute an incomplete antiparallel barrel structure, whereas the overall folding motif of β-strands is regarded as a common feature of the Rieske ISPs.

The cluster-binding site is formed by the cluster-binding loops β4–β5 (loop1, residues 122–131) and β6–β7 (loop2, residues 143–145) and the proline loop (P-loop, β8–β9, residues 158–165). Iron-ion Fe1 is coordinated by Cys124Sγ from loop1 and Cys142Sγ from loop2, and iron-ion Fe2 is liganded by His126Nδ1 from loop1 and His145Nδ1 from loop2 (Figure 21B). The cluster-binding loops 1 and 2 are stabilized by a disulfide bridge between Cys129 and Cys144. The atomic structure provides direct evidence for the correct insertion of the iron-sulfur cluster into the Rieske$_{sol}$ apoprotein during heterogeneous expression in *E. coli*, as indicated from our previous electron spin resonance (ESR) measurements [83].

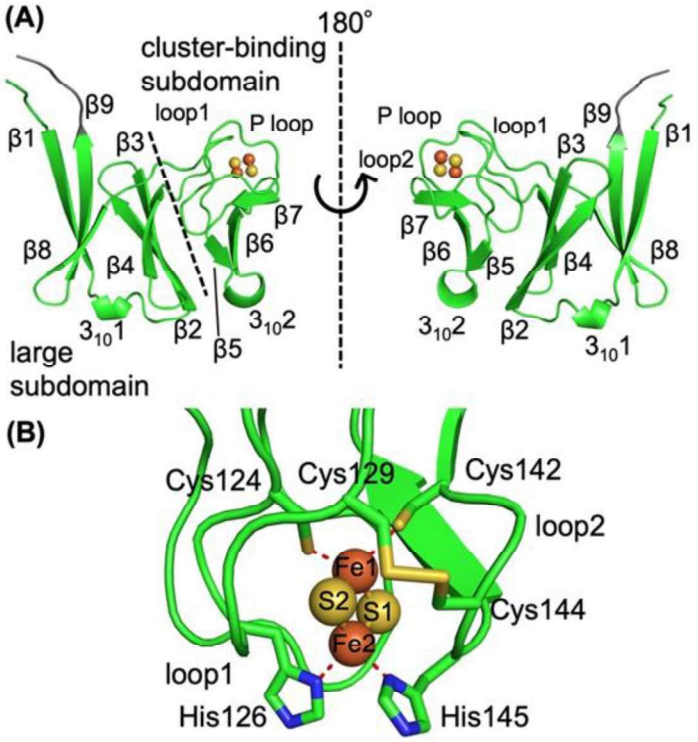


Figure 21. 3D-structure of the Rieske$_{sol}$

(A) Structure of the soluble domain of the Rieske ISP (Rieske$_{sol}$) from *C. tepidum*. His-tag region in the C-terminus was colored with grey. It contains nine β-sheets and two 3_{10} helices. (B) Close-up view of the [2Fe-2S] cluster in (A). Bonds between [2Fe-2S] cluster and ligand residues are shown in red dotted line. Cys129 in loop1 and Cys144 in loop2 form a disulfide bond (shown in yellow) to stabilize the structure around [2Fe-2S] cluster.

Structure of the [2Fe–2S] cluster

The geometries of the [2Fe-2S] cluster of the Rieske$_{sol}$ were compared with those of various Rieske ISPs from spinach chloroplast (PDBID 1RFS) [80], *Mastigocladus laminosus* (PDBID 1VF5) [11], bovine heart (PDBID 1RIE) [78], *Paracoccus denitrificans* (PDBID 2YIU) [74] and PetC3 protein (PDBID 5CXM) [82]to determine any difference in their bond lengths and bond angles (Table 3). Although the number of hydrogen bonds was different among these five species, no significant differences were observed in respective bond lengths and bond angles in the [2Fe-2S] cluster. Only slightly different bond lengths were found between the iron atom Fe2 and His126Nδ in the Rieske$_{sol}$ of *C. tepidum*, which might have been distorted by SeMet displacement at residue 129.

Table 3. Geometry of the [2Fe-2S] cluster of Rieske ISPs

	C. tepidum	Spinach	*M. laminosus*	Bovine heart	*P. denitrificans*	PetC3
Complex type	Rieske/cyt*b*	cyt b_6f	cyt b_6f	cyt bc_1	cyt bc_1	
[2Fe-2S] cluster						
Bond length (Å)						
Fe1-S1	2.2	2.4	2.2	2.2	2.2	2.2
Fe1-S2	2.3	2.3	2.2	2.2	2.2	2.2
Fe2-S1	2.3	2.3	2.2	2.2	2.2	2.2
Fe2-S2	2.2	2.3	2.2	2.3	2.2	2.3
Bond angle (deg)						
Fe1-S1-Fe2	77.2	71.7	77.0	74.7	88.7	73.4
Fe1-S2-Fe2	77.8	71.4	75.1	74.0	89.1	73.7
S1-Fe1-S2	102.5	105.7	103.8	105.6	90.7	106.9
S1-Fe2-S2	101.8	109.1	104.1	105.6	91.3	106.0
Cluster ligands						
Bond length (Å)						
Fe1-Cys124/107/108/139/132/77 Sγ	2.2	2.3	2.3	2.3	2.2	2.3
Fe1-Cys142/125/126/158/152/95 Sγ	2.5	2.2	2.3	2.2	2.1	2.3
Fe2-His126/109/110/141/134/79 Nδ1	2.4	2.2	2.3	2.2	2.0	2.2
Fe2-His145/128/129/161/155/98 Nδ1	2.1	2.2	2.3	2.1	2.1	2.1
Bond angle (deg)						
Cys124/107/108/139/132/77 Sγ-Fe1-Cys142/125/126/158/152/95 Sγ	109.6	110.2	104.8	105.6	114.5	112.6
His126/109/110/141/134/79 Nδ1-Fe2-His145/128/129/161/155/98 Nδ1	96.9	90.5	78.6	90.8	104.0	99.4
Hydrogen bonds						
Donor-acceptor distance (Å)						
S1-His145/128/129/161/155/98 N	3.2	3.2	3.7	3.2	3.1	3.7
S1-Ala147/Ser130/131/163/157/Ala100 N	4.0	3.4	3.9	3.6	3.8	3.6
S1-－/Ser130/131/163/157/－ Oγ	—	3.2	3.1	3.2	3.2	—
S2-Leu127/110/111/142/135/Asn80 N	3.3	3.4	3.8	3.1	3.3	3.2
S2-Cys129/112/113/144/137/82 N	3.9	3.6	3.6	3.6	4.0	3.7
Cys124/107/108/139/132/－ Sγ-Tyr149/132/133/165/159/－ Oη	3.4	3.1	3.6	3.1	3.2	—
Cys124/107/108/139/132/77 Sγ-His126/109/110/141/134/79 N	3.5	3.6	4.3	3.5	3.2	3.5
Cys142/125/126/158/152/95 Sγ-Cys144/127/128/160/154/97 N	3.8	3.6	3.8	3.8	3.8	3.5

These values were measured by PyMOL. The atom numbering corresponds to that of Figure 9B.

Structural similarities with other Rieske ISPs

The structure of the Rieske$_{sol}$ determined in the present study was compared with those of soluble domains of the Rieske ISPs from spinach chloroplast (PDBID 1RFS, RMSD of 2.6) [80], *Mastigocladus laminosus* (PDBID 1VF5, RMSD of 4.6) [11], bovine heart (PDBID 1RIE, RMSD of 2.9) [78] and *Paracoccus denitrificans* (PDBID 2YIU, RMSD of 3.7) [74] by superimposition using PyMOL (Figure 22). The RMSD values were also calculated using Dali server [57]. Ligand loops 1 and 2 and the proline loop in the cluster-binding domain were nearly identical, but the folding in the large subdomain seemed to be somewhat dissimilar. The structure of the *C. tepidum* Rieske$_{sol}$ exhibited the highest similarity to that of the PetC3 protein (PDBID 5CXM, RMSD of 1.9) (Figure 23) [82]. The PetC3 protein is thought to be located in a periplasmic fraction and to anchor to the plasma membrane through the fatty acid chain covalently bound to the N-terminal cysteine residue. Although proteomic analysis of the PetC3-defected strain indicated a disorder in the nitrogen-related metabolic system, the distinct functions of this protein have not yet been revealed.

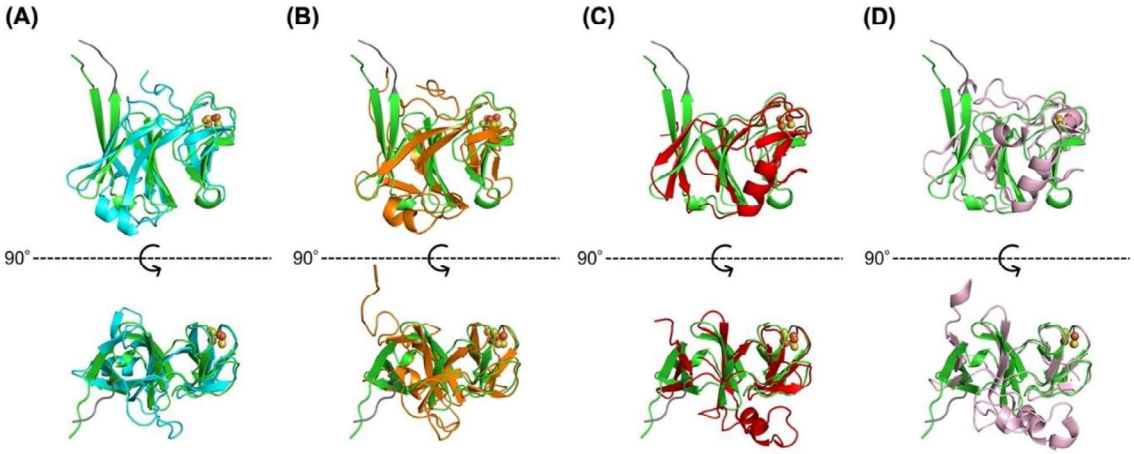


Figure 22. Structure comparison of the soluble domain of Rieske ISPs

Structure comparison of the *C. tepidum* Rieske$_{sol}$ (yellow green) with the soluble domain of Rieske ISPs from (A) spinach chloroplast (cyan; PDBID 1RFS), (B) *Mastigocladus laminosus* (orange; 1VF5), (C) bovine heart (red; 1RIE) and (D) *Paracoccus denitrificans* (light pink; 2YIU), respectively, by superposition of their polypeptide chains with PyMOL. Amino acid sequences of the soluble domains of Rieske ISPs are aligned in Figure 24.

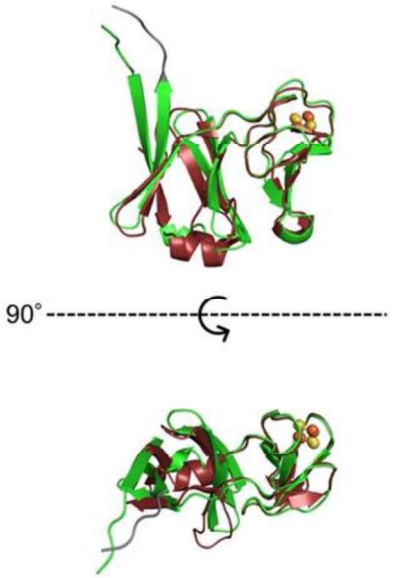


Figure 23. Structure comparison of the *C. tepidum* Rieske$_{sol}$ with PetC3 protein

Structure of the *C. tepidum* Rieske$_{sol}$ (yellow green) and it of PetC3 protein from *Synechocystis* sp. PCC 6803 (dark red; PDBID 5CXM) were compared by superposition of their polypeptide chains with PyMOL. The value of RMSD calculated by Dali server was 1.9.

The three-dimensional structures of the Rieske ISP soluble domains demonstrate that the proteins from cytochrome b_6f and bc_1 complexes could be related to each other, when their sequence alignment was constructed based on not only a simple pair-to-pair comparison of the amino acid sequences, but also the similarity of the secondary structure (Figure 24). The *C. tepidum* Rieske$_{sol}$ belongs to b_6f-type proteins, and its architecture was bilobal as indicated for b_6f-type proteins (see Figure 19) [80]. However, the insertion between β-2 and β-3 was relatively shorter (only two residues) and the C-terminal

extension of 14-15 residues was missing. The linker region of only six residues was also relatively shorter than typical b_6f- and bc_1-type proteins (approximately 13-15 residues). As the linker regions were involved in flexible movements of soluble domains, this might suggest a close spatial distance between cyt *b* and membrane-anchored cyt *c*-556.

Sequence alignment showed that amino acid residues as well as secondary structures in the cluster-binding subdomain are highly conserved between b_6f and bc_1 Rieske ISPs, while those in large subdomains are highly variable. The conservation of the small subdomains can be explained by a constraint due to a similar interaction mode with *b*-type cytochromes and plastoquinol/ubiquinol-binding sites. In contrast, the large subdomains are thought to have evolved to react properly with various membrane-bound *c*-type cytochromes, that is, cyt *f* and c_1 in b_6f and bc_1 complexes, respectively, or other electron acceptors, in the p-side aqueous phase. It is supposed that the Rieske ISPs would arise from a common ancestor as a redox center functioning in energy conversion systems. The large subdomain would also have diverged considerably between cytochrome b_6f and bc_1 complexes while the cluster-binding subdomain was highly conserved during evolution.

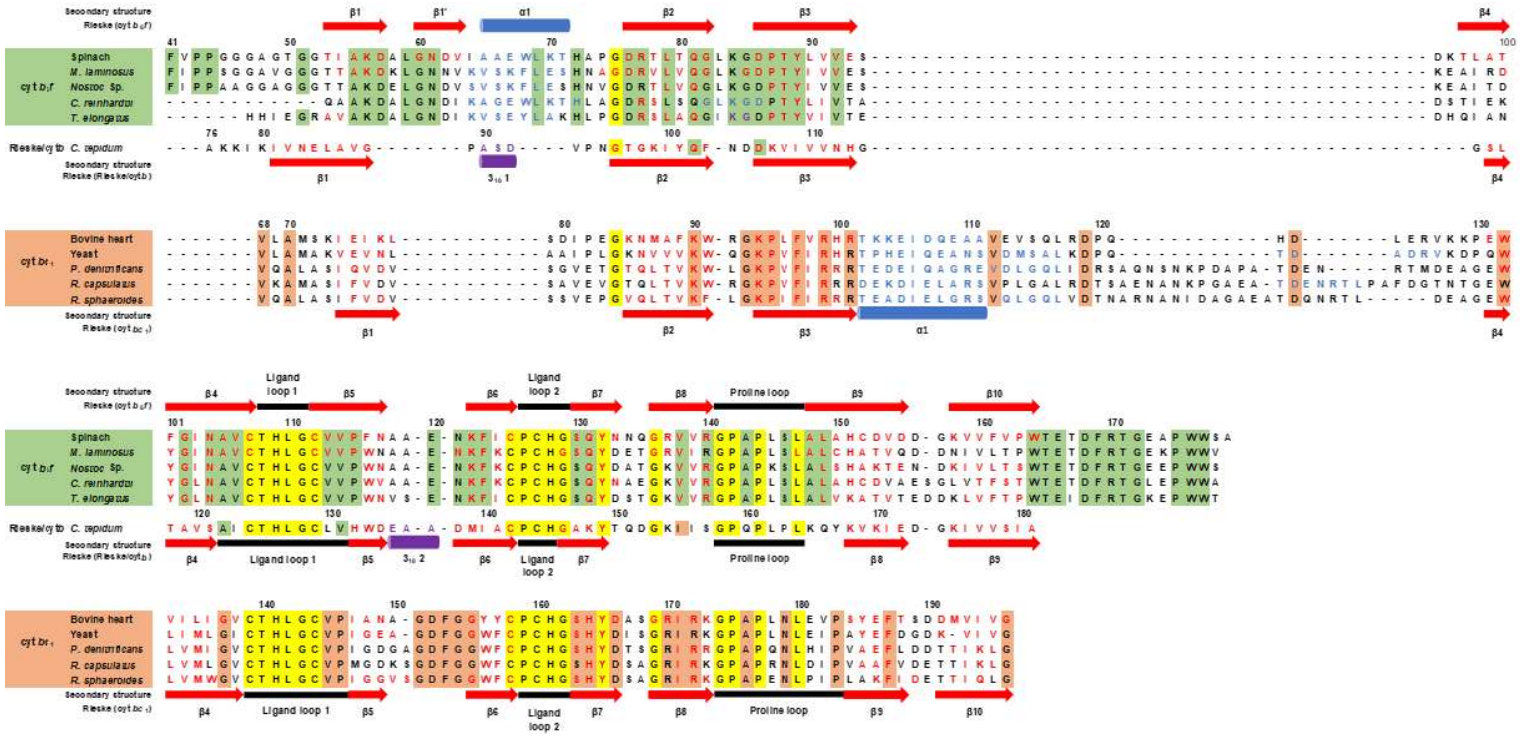

Secondary structure
Rieske (cyt b6f)
β1
β1'
α1
β2
β3
β4
Spinach
M. laminosus
Nostoc Sp.
C. reinhardtii
T. elongatus
cyt b6f
Rieske/cyt b
C. tepidum
Secondary structure
Rieske (Rieske/cytb)
β1
310 1
β2
β3
β4
Bovine heart
Yeast
P. denitrificans
R. capsulatus
R. sphaeroides
cyt bc1
Secondary structure
Rieske (cyt bc1)
β1
β2
β3
α1
β4
Ligand loop 1
Ligand loop 2
Proline loop
β4
β5
β6
β7
β8
β9
β10
Spinach
M. laminosus
Nostoc Sp.
C. reinhardtii
T. elongatus
cyt b6f
Rieske/cyt b
C. tepidum
Secondary structure
Rieske (Rieske/cytb)
β4
Ligand loop 1
β5
310 2
β6
Ligand loop 2
β7
Proline loop
β8
β9
Bovine heart
Yeast
P. denitrificans
R. capsulatus
R. sphaeroides
cyt bc1
Secondary structure
Rieske (cyt bc1)
β4
Ligand loop 1
β5
β6
Ligand loop 2
β7
β8
Proline loop
β9
β10

Figure 24. Sequence alignments of soluble domains of the Rieske ISPs

Alignments was constructed using sequences of the soluble domain of Rieske ISPs from cyt b_6f complex of spinach chloroplast (PDBID: 1RFS), *M. laminosus* (1VF5), *Nostoc* Sp. (4OGQ) [84], *C. reinhardtii* (1Q90) [85] and *T. elongatus* (3AZC) [86], cyt bc_1 complex of bovine heart (1RIE), yeast (1KYO) [87], *P. denitrificans* (2YIU), *R. capsulatus* (1ZRT) [88] and *R. sphaeroides* (2QJP), and the Rieske/cyt*b* complex of *C. tepidum*. Sequences were aligned primarily with ClustalW and then manually by checking with eyes [89]. Invariant positions of sequences in the Rieske ISPs of cyt b_6f and the Rieske/cyt*b* complexes are highlighted in green, and those in cyt bc_1 and the Rieske/cyt*b* complexes are highlighted in orange. Yellow highlights are for residues invariant in all groups of the Rieske ISPs. Residues of the Rieske ISPs from spinach, *C. tepidum* and bovine heart are numbered at the top of each sequence. Secondary structures of these three Rieske ISPs are indicated with blue cylinders for α helices, purple cylinders for 3_{10} helices and red arrows for β strands. Colored letters in each sequence also indicate secondary structures; blue for α helices, purple for 3_{10} helices and red for β strands.

E_m of the Rieske ISP in *C. tepidum* and PetC3 protein in *Synechocystis* sp. PCC 6803 have been shown to be +160mV and +135mV, respectively [43, 82, 90]. These values are relatively lower than those of other Rieske ISPs in cyt bc_1 or b_6f complex (E_m = approximately +300mV) [91-93]. The numbers of hydrogen bonds formed around the [2Fe-2S] clusters are considered to be related to the redox potentials of the Rieske ISPs (Figure 25). The high-redox-type Rieske ISPs of cyt bc_1 or b_6f complexes from spinach chloroplast, cyanobacterium *M. laminosus*, bovine heart and α-proteobacterium *P. denitrificans* have

eight hydrogen bonds. In low-redox-type one of *C. tepidum*, a serine residue was replaced with an alanine residue, resulting in seven hydrogen bonds. In PetC3 protein, a tyrosine residue was further replaced with a phenylalanine residue, resulting in only six hydrogen bonds (Figure 25). Therefore, the redox potentials of the [2Fe-2S] clusters decreased when the number of hydrogen bonds around them decreased, as previously demonstrated [93, 94].

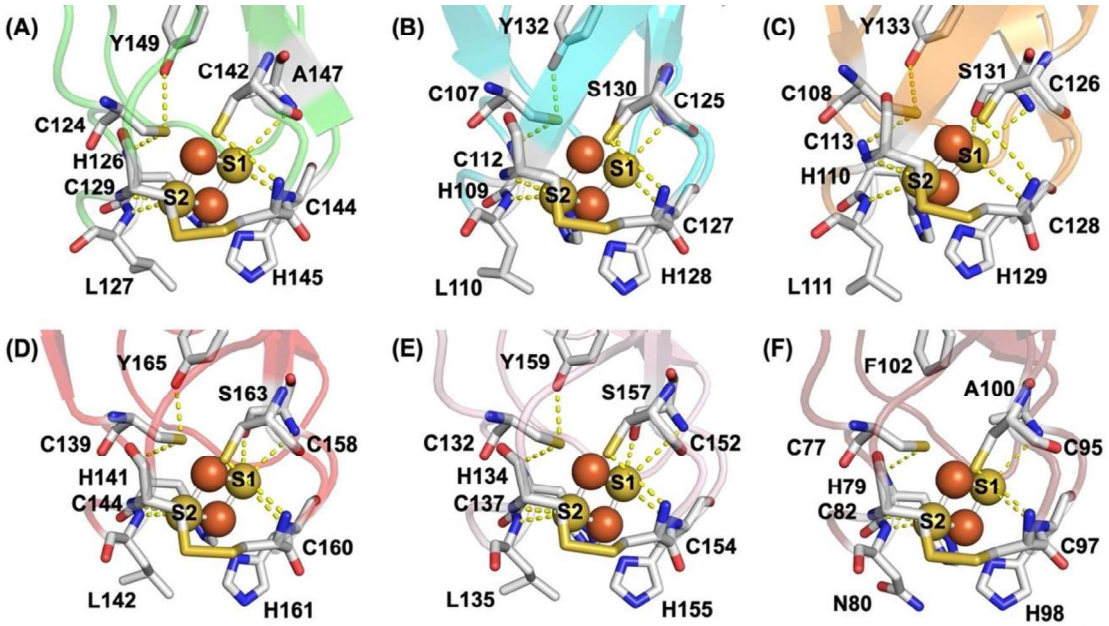


Figure 25. Hydrogen bonds formed around the [2Fe-2S] cluster of the Rieske ISP

Hydrogen bonds are indicated by yellow dotted lines: seven hydrogen bonds in *C. tepidum* (A), eight in spinach chloroplast (B), cyanobacterium *M. laminosus* (C), bovine heart (D) and α-proteobacterium *P. denitrificans* (E), and six for the case of PetC3 protein from *Synechocystis* sp. PCC 6803 (PDBID 5CXM) (F). See Table 3 for details of residues involved in the hydrogen-bond formations.

Surface properties of the Rieske ISPs

The soluble domains of Rieske ISP from b_6f and bc_1 complexes have different surface charges at neutral pH (Figure 26). The numbers of acidic and basic residues in each soluble domain are summarized along with those in their respective subdomains in Table 4. The values of pI calculated with ExPASy Compute pI/MW tool for overall structures were also different among species [95]. The pI values are 8.4 in *C. tepidum*, 5.4 in Spinach chloroplast, 6.5 in *M. laminosus*, 7.1 in bovine heart and 4.9 in *P. denitrificans*.

The differences in acidic and basic residue numbers in large subdomains primarily contribute to the pI value of each Rieske ISP. Although the β-barrel-like structures are highly conserved in large subdomains, their surface charges seem to have no relevance to either the interactions of the Rieske ISP soluble domains with their redox partners or the pHs in local areas where they function in the electron transport pathways. In fact, the pI of *C. tepidum* Rieske ISP is basic while the other proteins, regardless of whether they are bc_1- or b_6f-type, are weakly acidic or at least neutral (Table 4). In contrast, cluster-binding subdomains have considerably fewer charged residues than large subdomains and are characterized by nearly equal numbers of acidic and basic residues, thus resulting in almost neutral surface properties. In particular, the peripheral regions just adjacent to surface-exposed clusters are non-polar and are supposed to interact with both the quinone binding site of cyt *b* and the prosthetic group of the electron acceptor, heme *c* or *f*, as discussed in detail at discussion section.

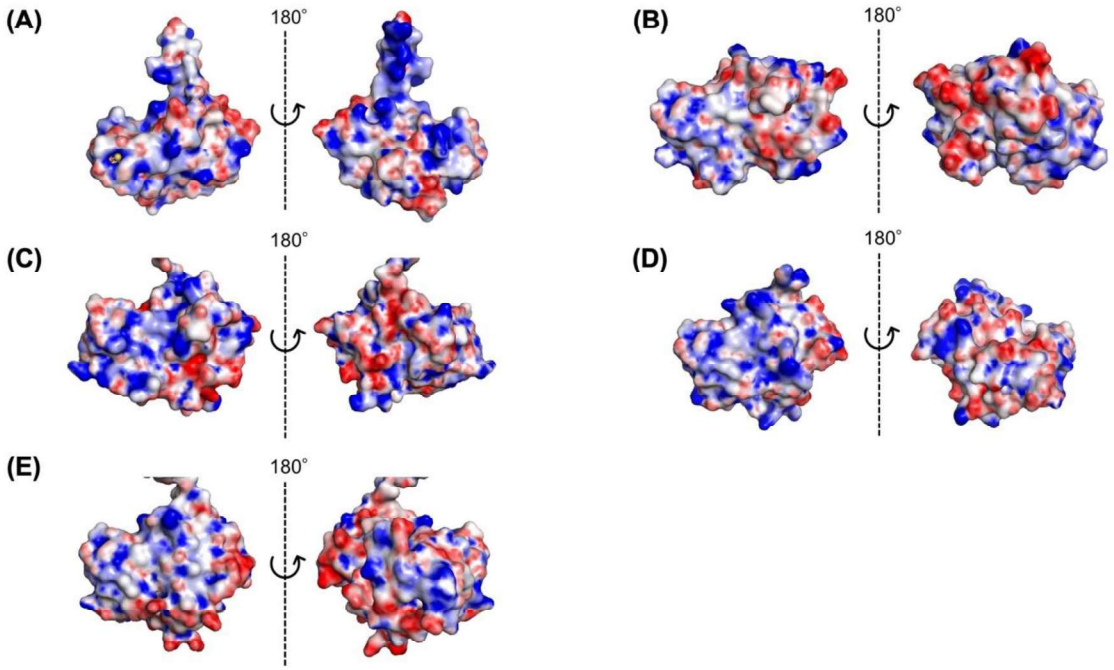


Figure 26. Electrostatic properties of the surfaces of soluble domains of Rieske ISPs

Surface charge of the Rieske ISPs from *C. tepidum* (A), spinach chloroplast (B), cyanobacterium *M. laminosus* (C), bovine heart (D) and α-proteobacterium *P. denitrificans* (E) were calculated by PyMOL APBS tool. The distribution is colored according to the electrostatic potential from $-10k_BT$ (red) to $+10k_BT$ (blue).

1 **Table 4. Electrostatic properties of the soluble domain of Rieske ISPs**

Complex type		**pI**		**Acidic residues**	Asp	Glu	**Basic residues**	Arg	Lys
cyt *b*$_6$*f*	Spinach	**5.42**	*large*	**13**	9	4	**7**	2	5
			cluster	**1**	0	1	**3**	2	1
				14	9	5	**10**	4	6
	M. laminosus	**6.46**	*large*	**12**	7	5	**10**	3	7
			cluster	**3**	1	2	**4**	2	2
				15	8	7	**14**	5	9
	Nostoc Sp.	**5.50**	*large*	**15**	7	8	**8**	2	6
			cluster	**2**	1	1	**5**	1	4
				17	8	9	**13**	3	10
	C. reinhardtii	**5.74**	*large*	**12**	7	5	**7**	2	5
			cluster	**2**	0	2	**4**	1	3
				14	7	7	**11**	3	8
	T. elongatus	**6.05**	*large*	**14**	8	6	**10**	3	7
			cluster	**2**	1	1	**3**	1	2
				16	9	7	**13**	4	9
Rieske/cyt*b*	*C. tepidum*	**7.88**	*large*	**6**	4	2	**9**	0	9
			cluster	**4**	3	1	**2**	0	2
				10	7	3	**12**	1	11
cyt *bc*$_1$	Bovine heart	**7.10**	*large*	**14**	6	8	**14**	5	9
			cluster	**3**	2	1	**3**	2	1
				17	8	9	**17**	7	10
	Yeast	**6.20**	*large*	**11**	7	4	**10**	3	7
			cluster	**4**	2	2	**3**	2	1
				15	9	6	**13**	5	8
	P. denitrificans	**4.94**	*large*	**17**	9	8	**10**	6	4
			cluster	**3**	3	0	**3**	3	0
				20	12	8	**13**	9	4
	R. capsulatus	**6.33**	*large*	**15**	7	4	**13**	7	6
			cluster	**4**	4	4	**5**	3	2
				19	11	8	**18**	10	8
	R. sphaeroides	**5.08**	*large*	**14**	7	7	**9**	6	3
			cluster	**3**	2	1	**3**	2	1
				17	9	8	**12**	8	4

The number of acidic and basic residues in large subdomain (*large*), cluster-binding subdomain (*cluster*). The entirety of the Rieske$_{sol}$ showed in the lines below them. The range of cluster-binding subdomains is between Ligand loop 1 and Proline loop.
2 The values of pI were calculated with ExPASy Compute pI/Mw tool.

3

4

Discussion

The structure of Rieske$_{sol}$ from *C. tepidum* determined in this study is composed with β-sheets as other Rieske ISPs. Structure of the soluble domain is classified into cyt bc_1 type and cyt b_6f type in terms of their sequences and structures. As reported previously, the Rieske$_{sol}$ has a bilobal shape as well as the soluble domains of Rieske ISP in cyt b_6f complex have [80]. Cluster-binding subdomains are highly conserved in the Rieske ISPs including the Rieske$_{sol}$. This conservation may be due to similar modes of interaction with Q_o sites and *c*-type cytochromes during electron transfer in each Rieske ISP. On the other hand, large subdomain is different in terms of structure and sequence between cyt bc_1 type and cyt b_6f type including the Rieske$_{sol}$ in *C. tepidum*. Electron acceptor of cyt bc_1 and b_6f type Rieske ISP is cyt c_1 and cyt *f*, respectively. They are different in structures that cyt c_1 is composed with α-helices and cyt *f* is β-sheets, resulting in different interaction sites or modes with the Rieske ISP. The large subdomain is supposed to be evolved to adapt in order to react with electron acceptor including specific *c*-type cytochromes in each species at the positive side of membranes.

In the cluster-binding subdomain, the number of hydrogen bonds around the cluster is related to the redox potential of the Rieske ISP. It has been reported that redox potential becomes lower as the number of hydrogen bonds decreases [93, 96, 97]. Cyt bc_1 and b_6f complexes receive electrons from high potential ubiquinone or plastoquinone (E_m = +100mV), whereas the Rieske/cyt*b* complex receive electrons from low potential menaquinones (E_m = -70mV) [14, 98]. The E_m of Rieske ISP in *C. tepidum* is +160mV, which accept an electron from low potential menaquinone. It is lower than the E_m of high-potential Rieske ISP in cyt bc_1 and b_6f complexes (E_m = +300mV) which accept an electron

from high potential quinones [43, 91-93]. Structural analysis in this study showed the Rieske$_{sol}$ contains one less hydrogen bond than high-potential Rieske ISP. Furthermore, the low-potential membrane-anchored PetC3 protein, which is structurally similar to the Rieske$_{sol}$, also forms the lower number of hydrogen bonds. These results suggest that the Rieske ISP evolved from a low-potential ancestral type to high-potential type by acquiring a transmembrane helix, regulating redox potential in the cluster-binding subdomain, and altering the amino acid residues and structures in large subdomains to adapt to the mode of electron transfer in the positive side of the membrane (Figure 27).

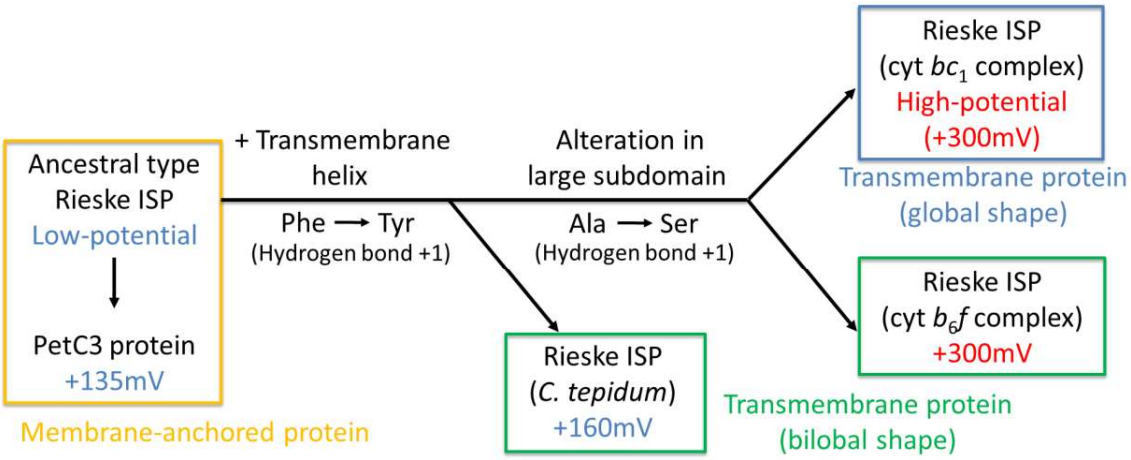


Figure 27. Evolution model of the Rieske ISPs

The low-potential membrane-anchored ancestral Rieske ISP might evolve into the high-potential transmembrane Rieske ISP that functions in cyt bc_1 and b_6f complexes. The ancestral Rieske ISP is thought to be a protein involved in the primitive energy conversion mechanism.

The length of the linker domain of Rieske ISP in *C. tepidum* would be shorter than those of cyt bc_1 and b_6f type Rieske ISPs, resulting in movement limitation of the soluble domain. In cyt bc_1 and b_6f complexes, the *c*-type cytochrome is fixed in position, whereas cyt *c*-556 can move its soluble domain. Therefore, electron transfer can be conducted in spite of movement limitation of the soluble domain because both proteins can move their soluble domains and approach each other.

Chapter IV. NMR analysis of the interactions between the Rieske$_{sol}$ and cyt *c*-556$_{sol}$

Introduction

Having determined the structures of the Rieske$_{sol}$ and cyt *c*-556$_{sol}$, interaction analysis between them was carried out. I tried to analyze by co-crystallization and pull-down assay, however, could not obtain the results to clarify their interactions. In electron transfer reaction, proteins do not always form interactions, but switch the bound and dissociated states. That is, the interactions between the Rieske ISP and cyt *c*-556 is supposed to be weak. Therefore, these methods are not suitable for analysis of weak interactions. Because of it, interaction sites on the Rieske$_{sol}$ were tried to detect by NMR measurement.

NMR measurement can observe interacting proteins in solution at an equilibrium of bound and dissociated state. Therefore, it is suitable for analysis of weak interactions in electron transfer reactions. On the other hand, the NMR measurement has several weak points. Firstly, the protein for measurement has to be low molecular weight (<30 kDa). This is because the number of signals and line width of them are increased in the measurement of higher molecular weight protein, resulting in preventing the analysis of NMR spectra. In this study, the transmembrane and linker domains of Rieske ISP were not expressed, but only the soluble domain containing [2Fe-2S]-cluster was, thus molecular weight was reduced. Secondly, the protein for NMR measurement has to be labeled with stable isotopes. In the previous study, I have successfully purified the uniformly ^{15}N-labeled Rieske$_{sol}$ ([U-^{15}N]-Rieske$_{sol}$) for ESR measurement [83]. I purified [U-^{15}N] and [U-^{13}C,

^{15}N]-labeled Rieske$_{sol}$ in the same methods in this study. In addition, paramagnetic iron atoms in the [2Fe-2S]-cluster prevents the observation of signals of the amino acid residues located in the vicinity of the cluster. Therefore, in addition to the measurements of Rieske$_{sol}$, I also tried to purify the Rieske$_{sol}$ with gallium substituted for iron in the [2Fe-2S]-cluster following the previous report [99].

In this chapter, I presented the results of detection of interaction sites with cyt *c*-556 on the Rieske$_{sol}$ by chemical shift perturbation method. Based on these results, a docking model of the Rieske$_{sol}$ and cyt *c*-556$_{sol}$ was constructed and their interactions were verified. As described in chapters I and II, soluble cyt *c*-554 would not be involved in electron transfer from the Rieske ISP, despite its structural similarity to cyt *c*-556$_{sol}$. I also discussed the cause of this difference in the reaction mechanisms by comparing the structures of docking model and cyt *c*-554.

Materials and Methods

Overexpression of the uniformly ^{13}C, ^{15}N-labeled Rieske$_{sol}$

The pET21a(+)-*petC*$_{sol}$-His6 vector was transformed into in *E. coli* strain C41(DE3) cells harboring plasmid pRKISC. The [U-^{15}N]- and [U-^{13}C,^{15}N]-labeled Rieske$_{sol}$ were overexpressed in M9 minimum medium containing 1.0 g L^{-1} $^{15}NH_4Cl$ in the absence or presence of 4.0 g L^{-1} [U-^{13}C]-D-glucose (Cambridge Isotope Laboratories, Inc., Tewksbury, MA, USA). The cells were cultivated at 37 °C to an absorbance of approximately 0.3 at 600 nm. The expression of the labeled Rieske$_{sol}$ was induced with 0.1 mM IPTG. The cells were grown for 20 h at 25 °C, and labeled Rieske$_{sol}$ was purified as described in Chapter III.

Preparation of cyt *c*-556$_{sol}$

Cyt *c*-556$_{sol}$ was purified as described in Chapter I and II.

NMR measurement and docking models

NMR experiments were conducted on Avance III HD 600 spectrometer using QCI-P cryogenic probes with ^{1}H resonance frequency of 600 MHz (Bruker, Billerica, MA, USA). Sequence-specific assignments were made from the 2D ^{1}H-^{15}N heteronuclear single-quantum coherence (HSQC) and 3D HNCA, HN(CO)CA, HNCO, HN(CA)CO, HNCACB, and CBCA(CO)NH spectra of 1.36 mM [U-^{13}C, ^{15}N]-Rieske$_{sol}$ dissolved in 20 mM Tris-HCl buffer (pH 7.5) containing 50 mM NaCl at 298 K. Spectrum data was analyzed by NMRFAM-Sparky and I-PINE web server [100, 101]. The gene for the Rieske$_{sol}$ encodes 114 amino acids including 6 Pro residues which cannot be assigned because these do not contain an NH group.

The 80 ^{1}H-^{15}N peaks were assigned to the ^{1}H-^{15}N HSQC spectrum of the Rieske$_{sol}$

(Figure 28). The peaks of amino acid residues which detected and not detected were shown in Table 5. In particular, peaks of residues in loop 2 (distance from cluster is approximately 4Å to 20Å) could not be detected because of paramagnetic iron atoms of the [2Fe-2S] cluster.

Chemical shift perturbation experiments were performed by recording 2D ^{1}H-^{15}N HSQC spectra of 100 μM [U-^{15}N]-Rieske$_{sol}$ dissolved in 20 mM Tris-HCl buffer (pH 7.5) containing 50 mM NaCl in the absence and presence of 300 μM of cyt *c*-556$_{sol}$ at 298 K. The spectra were measured with ^{1}H and ^{15}N acquisition periods of 106.5 and 45.7 ms, respectively. The experiment time for each spectrum was 1h with 16 scans accumulated for each FID. The redox states of both proteins were confirmed by measuring their absorption spectra with a model UV-3101PC spectrophotometer (Shimadzu).

All NMR data were processed using TopSpin (Bruker), and spectra were analyzed using NMRFAM-Sparky [100]. The weighted averages of ^{1}H and ^{15}N chemical shift changes were calculated using the formula $\Delta\delta = [(\Delta\delta^{1}_{HN})^2 + (0.04\Delta\delta^{15}_{N})^2]^{1/2}$ [99]. The simulated docking models were calculated using ZDOCK by submitting the co-ordinates to the ZDOCK Web server [102]. The binding free energy for each protein complex model was estimated using the PDBePISA on the Protein Data Bank Europe website [103, 104]. Protein-protein interactions were further examined using by Ligplot+ [105].

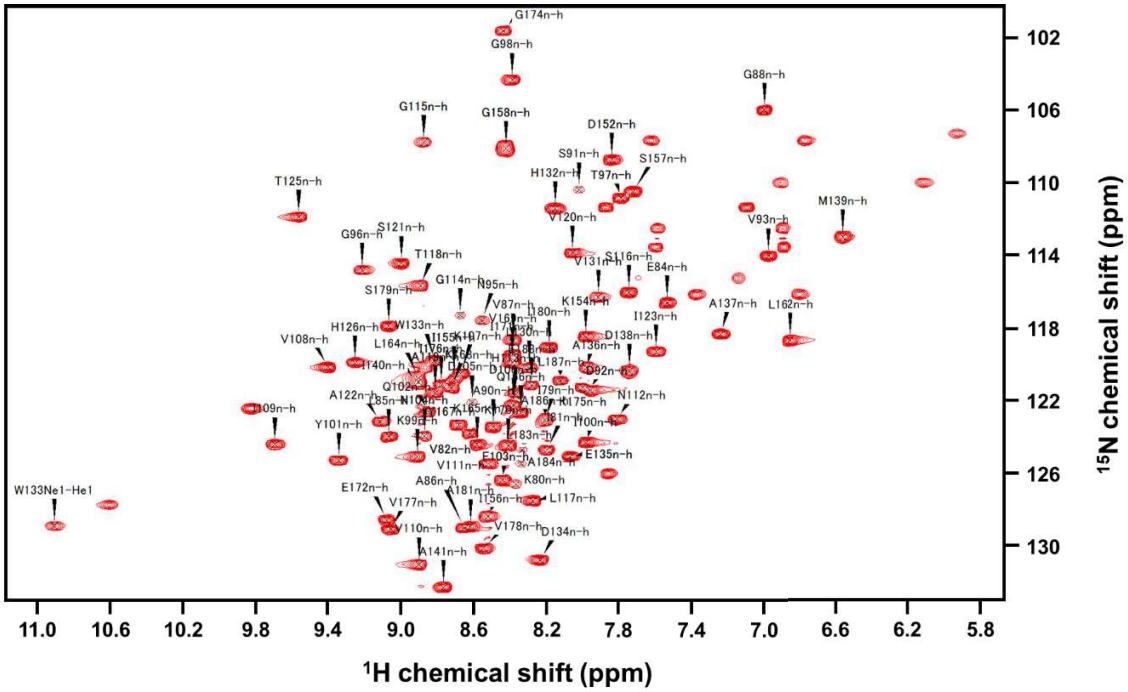


Figure 28. 2D ^{1}H-^{15}N HSQC spectrum of [U-^{13}C, ^{15}N]-labeled Rieske$_{sol}$

2D ^{1}H-^{15}N HSQC spectrum of 1.36mM reduced [U-^{13}C, ^{15}N]-labeled Rieske$_{sol}$ at pH7.5 and 298K. Labeling of peaks was based on analysis of through-bond connectives from the [U-^{13}C, ^{15}N]-labeled Rieske$_{sol}$.

Table 5. Chemical shifts of the Rieske$_{sol}$

Residues	^{15}N (ppm)	^{1}H (ppm)	Residues	^{15}N (ppm)	^{1}H (ppm)	Residues	^{15}N (ppm)	^{1}H (ppm)
A76	nd	nd	N112	123.016	7.807	K148	nd	nd
K77	nd	nd	H113	121.641	8.365	Y149	nd	nd
K78	nd	nd	G114	117.29	8.669	R150	nd	nd
I79	123.064	8.202	G115	107.761	8.87	Q151	nd	nd
K80	126.593	8.365	S116	116.02	7.741	D152	108.736	7.835
I81	124.693	8.191	L117	127.5	8.27	G153	108.106	8.418
V82	123.781	8.616	T118	115.672	8.889	K154	118.489	7.978
N83	nd	nd	A119	121.566	8.807	I155	120.76	8.703
E84	116.607	7.531	V120	113.855	8.052	I156	128.367	8.517
L85	123.974	9.062	S121	114.426	8.993	S157	110.487	7.719
A86	129.008	8.646	A122	123.149	9.11	G158	108.106	8.418
V87	118.682	8.377	I123	119.309	7.592	P159	nd	nd
G88	105.998	6.997	C124	nd	nd	Q160	nd	nd
P89	nd	nd	T125	111.88	9.558	P161	nd	nd
A90	123.43	8.487	H126	119.922	9.248	L162	118.679	6.848
S91	110.37	8.017	L127	nd	nd	P163	nd	nd
D92	121.428	7.958	G128	nd	nd	L164	120.743	8.899
V93	113.996	6.974	C129	nd	nd	K165	124.393	8.577
P94	nd	nd	L130	120.2	8.29	Q166	122.655	8.337
N95	117.579	8.551	V131	116.292	7.91	Y167	123.325	8.679
G96	114.803	9.208	H132	111.418	8.148	K168	121.306	8.719
T97	110.834	7.786	W133	119.816	8.811	V169	119.449	8.38
G98	104.342	8.383	D134	130.76	8.23	K170	124.477	8.405
K99	125.073	8.906	E135	125.068	8.066	I171	119.891	8.384
I100	124.303	7.977	A136	120.186	7.975	E172	128.576	9.073
Y101	125.28	9.338	A137	118.34	7.237	D173	nd	nd
Q102	122.623	8.844	D138	120.385	7.74	G174	101.638	8.433
F103	126.357	8.437	M139	112.98	6.557	K175	121.282	7.995
N104	123.945	8.866	I140	120.971	8.901	I176	121.107	8.773
D105	122.098	8.605	A141	132.281	8.763	V177	129.075	9.051
D106	122.252	8.376	C142	nd	nd	V178	130.107	8.54
K107	120.521	8.669	P143	nd	nd	S179	117.878	9.064
V108	120.153	9.397	C144	nd	nd	I180	119.069	8.18
I109	124.405	9.689	H145	nd	nd	A181	128.917	8.613
V110	131.018	8.897	G146	nd	nd			
V111	125.471	8.515	A147	nd	nd			

nd: not detected

Results

Interaction sites on the Rieske ISP

Electrons can be transferred efficiently from the Rieske ISP to cyt *c*-556 as previously demonstrated [24]. To visualize their direct interaction sites, I attempted to crystallize the Rieske$_{sol}$ complexed with cyt *c*-556$_{sol}$. Unfortunately, I obtained only crystals of the Rieske$_{sol}$ in the mixture drops containing these two proteins. This would be due to weak association properties that allow high turnover numbers by repeating a transient complex formation between them [106]. In fact, the pull-down assay using the His-tagged Rieske$_{sol}$ attached to the Ni-NTA resin did not succeed in holding cyt *c*-556$_{sol}$ by their affinity. In these situations, NMR spectroscopy to explore interaction sites between two soluble proteins is a powerful and definitive tool so far, because the chemical shift perturbations can be detected even if these interactions are relatively weak. In addition, the molecular weight of the Rieske$_{sol}$ is sufficiently small and suitable for NMR analyses. Therefore, NMR measurements were performed using [U-^{15}N]-Rieske$_{sol}$ as a probe to identify its residue-level interaction sites when it formed a complex with cyt *c*-556$_{sol}$.

I first mixed [U-^{15}N]-Rieske$_{sol}$ with cyt *c*-556$_{sol}$. However, almost no chemical shift changes were observed. Both proteins were mostly in the oxidized states when their absorption spectra were measured, and therefore, their different redox states were supposed to be necessary for their interaction to be observed. Then, I prepared fully reduced [U-^{15}N]-Rieske$_{sol}$ and oxidized cyt *c*-556$_{sol}$ by adding a reducing reagent of sodium ascorbate and an oxidizing reagent of potassium ferricyanide, respectively. After mixing, the chemical shift changes due to their interaction could be detected (Figure 29). Nevertheless, some perturbations were suspected to be derived from direct conformation changes upon the reduction and/or oxidation of the [U-^{15}N]-Rieske$_{sol}$ itself, but not upon the specific

interaction with cyt *c*-556$_{sol}$. The cyt *c*-556$_{sol}$ used for the first time in the NMR measurement was fully oxidized during a long-term storage for approximately 2 years at -80 ℃. Fortunately, the freshly prepared cyt *c*-556$_{sol}$ was partially reduced (55%) (Figure 30). The redox potentials were reported to be very close to +160mV for the Rieske ISP and +190mV for cyt *c*-556 [43]. Therefore, when the oxidized [U-^{15}N]-Rieske$_{sol}$ and partially reduced cyt *c*-556$_{sol}$ were mixed, their association was expected to proceed and reach redox equilibrium.

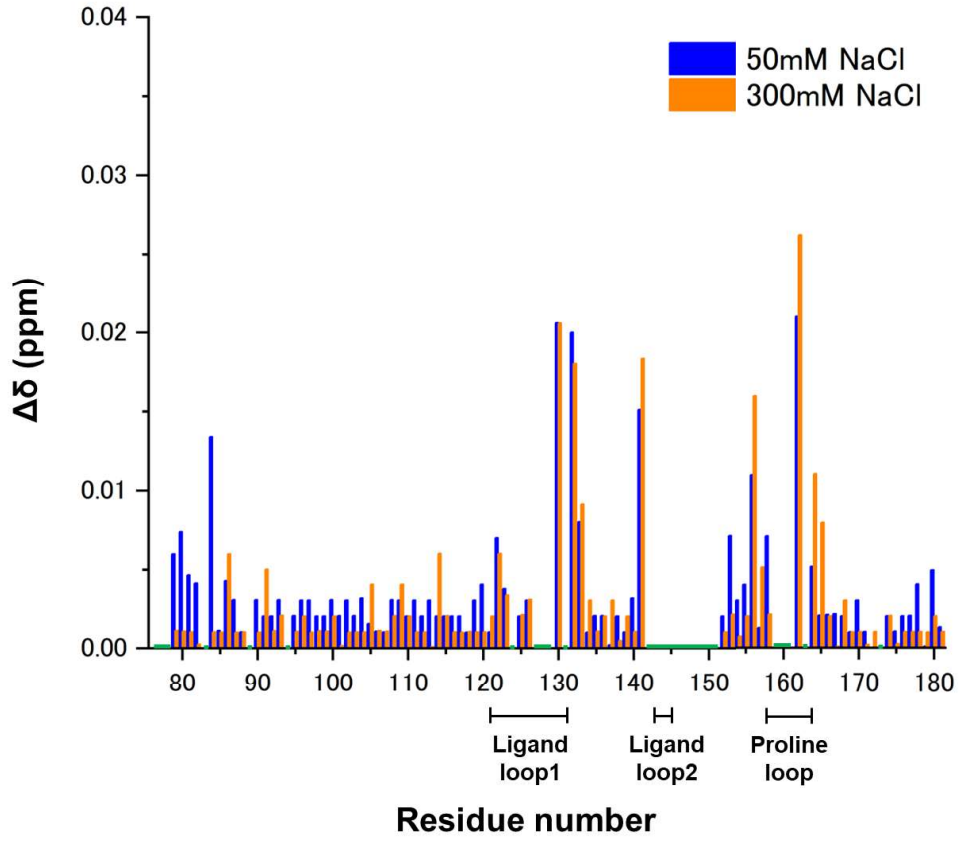


Figure 29. Chemical shift changes of the reduced Rieske$_{sol}$

Chemical shift changes of the chemically reduced [U-^{15}N]-Rieske$_{sol}$ after the addition of chemically oxidized cyt *c*-556 in the presence of 50mM NaCl (blue) and 300mM NaCl

(orange), as described in the text. Residues which could not be assigned are indicated by green lines.

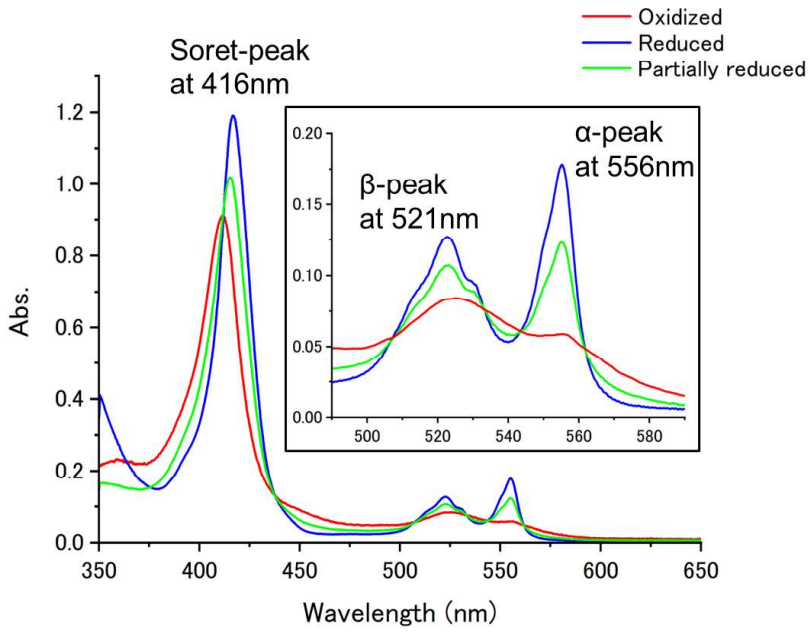


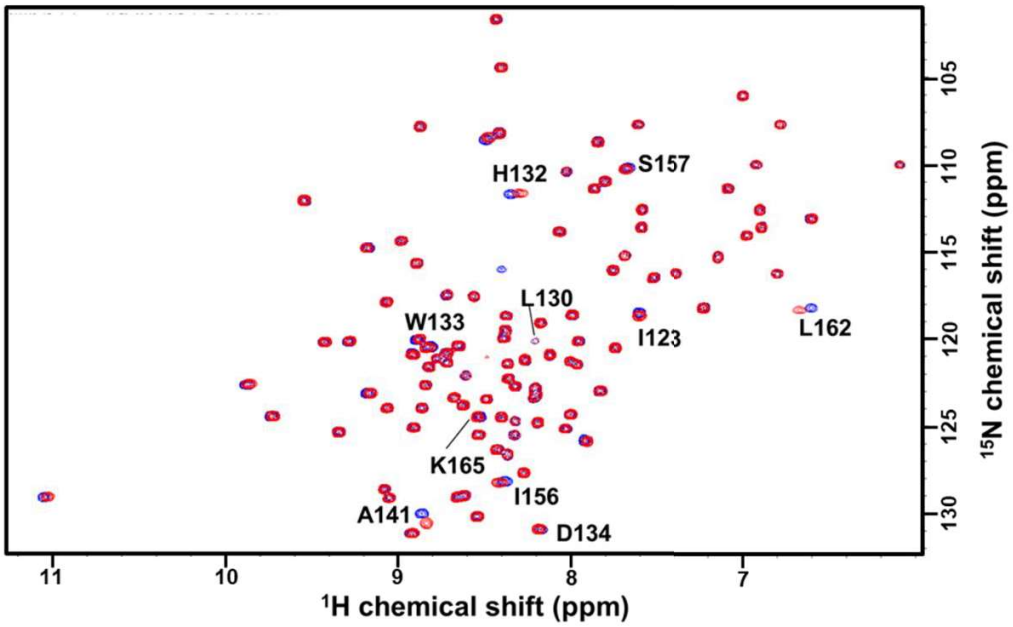
Figure 30. Absorption spectra of cyt *c*-556$_{sol}$

Absorption spectra of cyt c-556sol in oxidized (red line), ascorbate-reduced (blue line) and partially reduced states (green line). The α- an β-regions were enlarged in the inset. The freshly prepared cyt *c*-556$_{sol}$ was partially reduced, while a long-term stored one was fully oxidized.

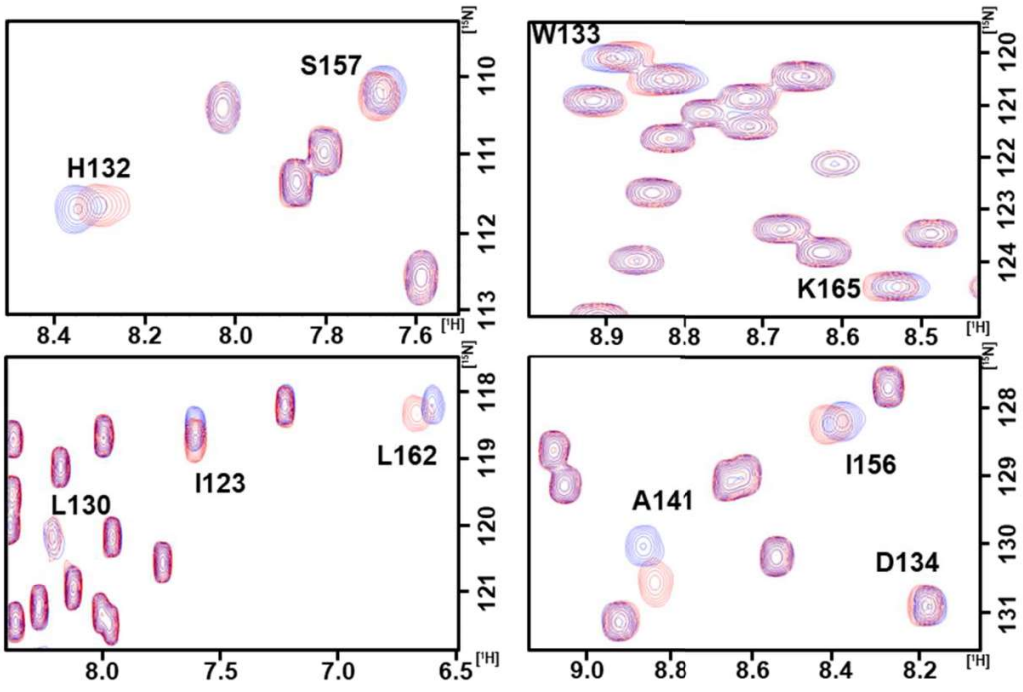
Small but discernible changes in the chemical shifts were observed for the peaks from residues located on the belt region around the cluster-binding subdomain comprising Ile123, Leu130, His132, Trp133, Asp134, Ala141, Ile156, Ser157, Leu162 and Lys165 (Figure 31). These residues were almost the same as those identified in a sample containing chemically reduced [U-^{15}N]-Rieske$_{sol}$ and oxidized cyt *c*-556$_{sol}$ (Figure 29), and thus were considered to be involved in the complex formation between the [U-^{15}N]-Rieske$_{sol}$ and cyt *c*-556$_{sol}$ on the electron transfer reaction. However, the shift signals derived from residues on or close to the cluster-binding portion were invisible due to the paramagnetic effect of Fe(III) of the [2Fe-2S] cluster. The ligand residues of this cluster were expected to be the most promising direct interaction sites with cyt *c*-556$_{sol}$ from the docking model construction as described in next section. I also attempted to prepare Ga-substituted cluster to make it diamagnetic in a similar manner to that reported for plant-type Fd. However, I failed to reconstitute a stable [2Ga-2S] cluster in the Rieske$_{sol}$, probably due to a different combination of ligand residues (two cysteine and two histidine residues) in the Rieske ISP [99, 107].

NMR measurements were also performed at a higher salt concentration of 300 mM NaCl instead of 50 mM NaCl. Although slightly increased intensities were observed in the chemical shift changes for the peaks of Ala141, Ile156, Leu162 and Lys165, no significant differences were observed for other peaks, indicating that the interaction between the [U-^{15}N]-Rieske$_{sol}$ and cyt *c*-556$_{sol}$ was not affected by ionic strength (Figure 29).

(A)

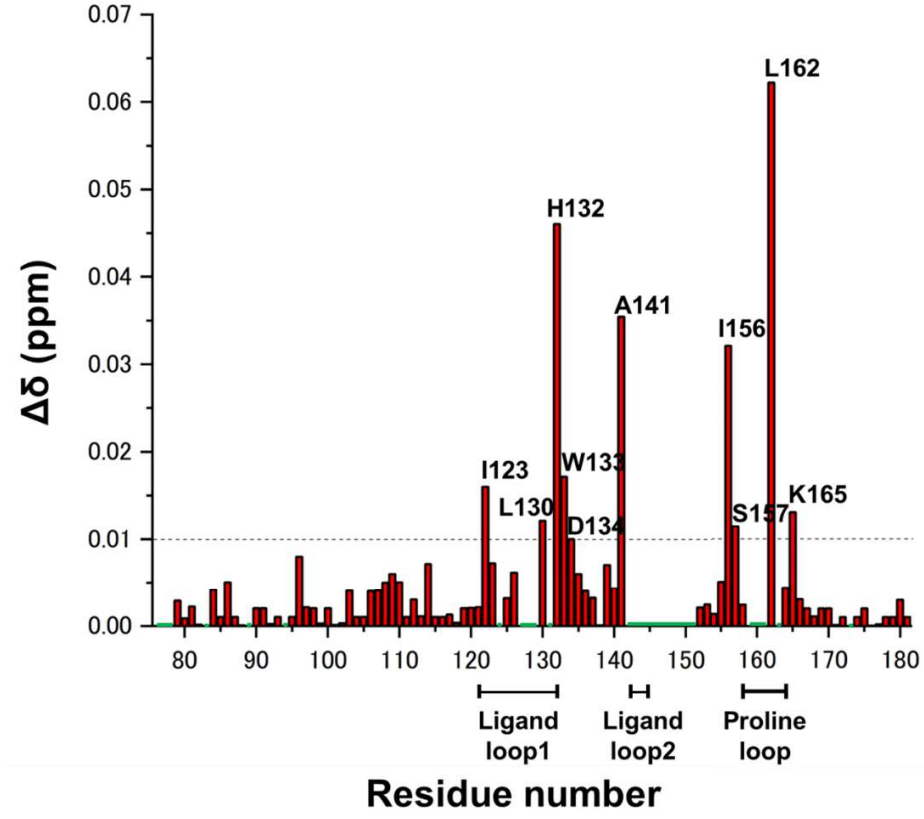

H132
S157
L130
W133
I123
L162
K165
I156
A141
D134
^{15}N chemical shift (ppm)
^{1}H chemical shift (ppm)

(B)

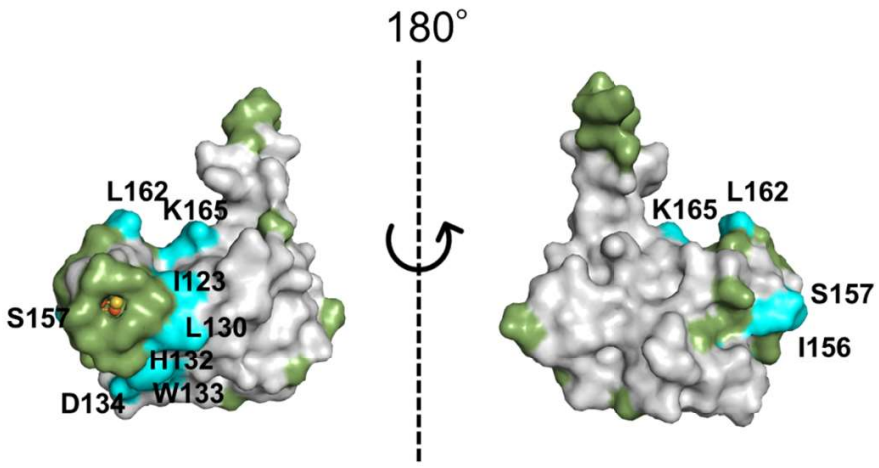

S157
H132
W133
K165
L162
I123
L130
I156
A141
D134

1

(C)


0.07
0.06
0.05
0.04
0.03
0.02
0.01
0.00
Δδ (ppm)
L162
H132
A141
I156
I123
W133
L130
D134
S157
K165
80
90
100
110
120
130
140
150
160
170
180
Ligand loop1
Ligand loop2
Proline loop
Residue number

(D)


180°
L162
K165
I123
S157
L130
H132
D134
W133
K165
L162
S157
I156

1

2

Figure 31. Chemical shift changes of the Rieske$_{sol}$

(A) ^{1}H-^{15}N HSQC spectra of the [U-^{15}N]-Rieske$_{sol}$. Overlay of the HSQC spectra in the absence (shown in blue) and presence (shown in red) of cyt *c*-556. (B) The regions of chemical shifts were enlarged to show slight differences. (C) Chemical shift changes of the [U-^{15}N]-Rieske$_{sol}$ after the addition of cyt *c*-556. Residues unable to be assigned are indicated by green lines. (D) Mapping of the chemical shift changes onto the 3D structure of the Rieske$_{sol}$. The residues show chemical shifts (>0.01 ppm) are colored by cyan and the residues which did not show chemical shifts are colored by grey. The residues which were not assigned are colored by green.

Docking models between the Rieske$_{sol}$ and cyt *c*-556$_{sol}$

A docking model of the Rieske$_{sol}$ and cyt *c*-556$_{sol}$ was constructed using the ZDOCK server [102]. Protein-protein docking calculations were performed by specifying amino acid residues of the Rieske$_{sol}$, to which cyt *c*-556$_{sol}$ should be bound based on the above results of NMR chemical shift perturbation experiments of the [U-^{15}N]-Rieske$_{sol}$. Among the ZDOCK outputs, the top ten docking structures ranked based on their ZDOCK scores were examined to determine whether the [2Fe-2S] cluster and heme *c* faced each other at closer distances for electron transfer. I chose three models which were adopted as favorable models in terms of the locations of each co-factor. The stability of the interaction interface in each model was further assessed in terms of the binding free energy (ΔG_{bind}) estimated by the PDBePISA algorithm in the Protein Data Bank Europe [103, 104]. The estimates indicated a range of ΔG_{bind} of -9.7 to -5.3 kcal/mol. For efficient electron transfer, a turnover of association and dissociation between two proteins is important. Thus, their affinity should be adjusted properly to be not too tight or weak. The ΔG_{bind} between the Rieske ISP and cyt c_1 of bovine cyt bc_1 complex (PDBID: 1BE3) which form complex for electron transfer was estimated as -3.6 kcal/mol. Finally, I obtained the most probable docking model with ΔG_{bind} = -5.3 kcal/mol which showed closest value to it of bovine cyt bc_1 complex (Figure 32).

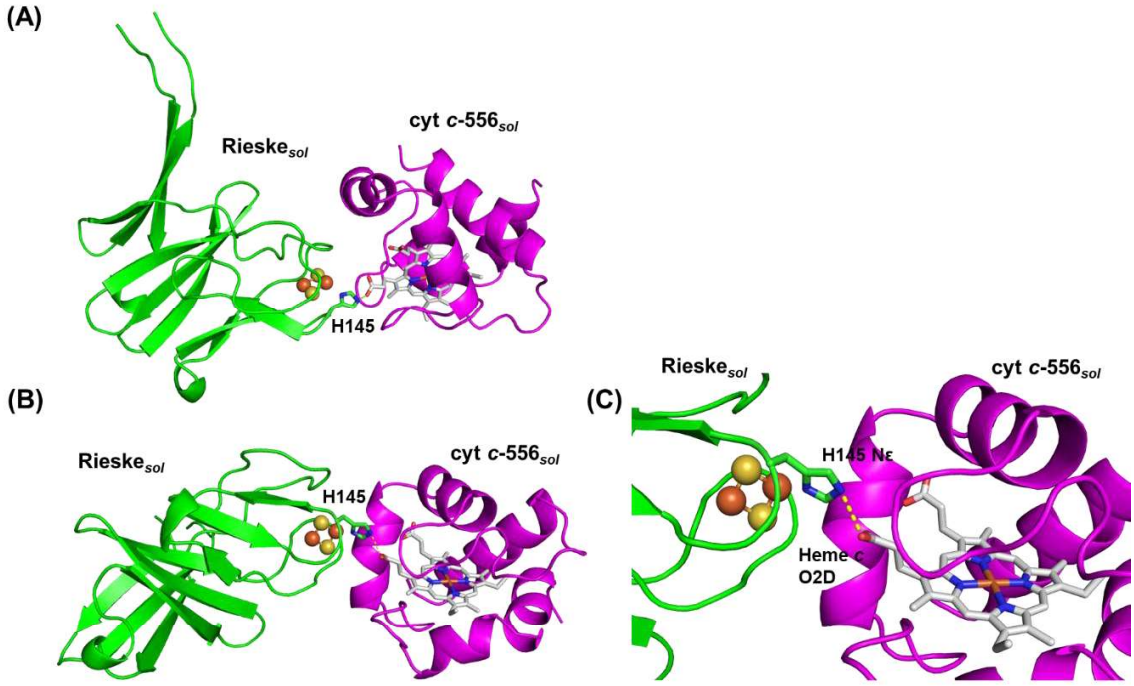


Figure 32. Docking model of the Rieske$_{sol}$ and cyt c-556$_{sol}$

From the top-ten models constructed with the ZDOCK server, the most suitable one was selected judged from the binding free energy (ΔG_{bind}). The model is viewed horizontally to the membrane plane (A) and along with the membrane normal from the periplasmic side (B). A single hydrogen bond is indicated by a yellow dotted line between a nitrogen (Nε) of H145 in the Rieske$_{sol}$ and an oxygen (O2D) of propionate group of heme c in cyt c-556$_{sol}$ (C). His145 is also one of four ligand residues for the [2Fe-2S] cluster.

The molecular interface of the protein-protein interaction site was checked using Ligplot+ [105]. Hydrogen bond formation was observed between the nitrogen atom (Nε) of H145 of the Rieske$_{sol}$, which is a ligand to an Fe ion (Fe2) of the [2Fe-2S] cluster, and an oxygen atom (O2D) of the propionate group in heme *c* (Figure 33A). In the bovine cyt bc_1 complex, a hydrogen bond is formed between the Nε of H161 of the Rieske ISP, which is also a ligand to Fe2 in the cluster, and O1D of the propionate group in heme *c* (Figure 33B) [106]. Although the two oxygen atoms of the propionate group are indistinguishable in the present heme *c* model, it is nevertheless rational to consider that the model complex of the Rieske$_{sol}$ and cyt *c*-556$_{sol}$ exhibits almost the same orientation as the counterpart of the bovine cyt bc_1 complex to carry out high turnover rates of electron transfer reactions. Moreover, the hydrophobic interactions could also be detected around the cluster and the heme pocket of the model complex, whose locations seemed to be analogous to those in the bovine cyt bc_1 complex.

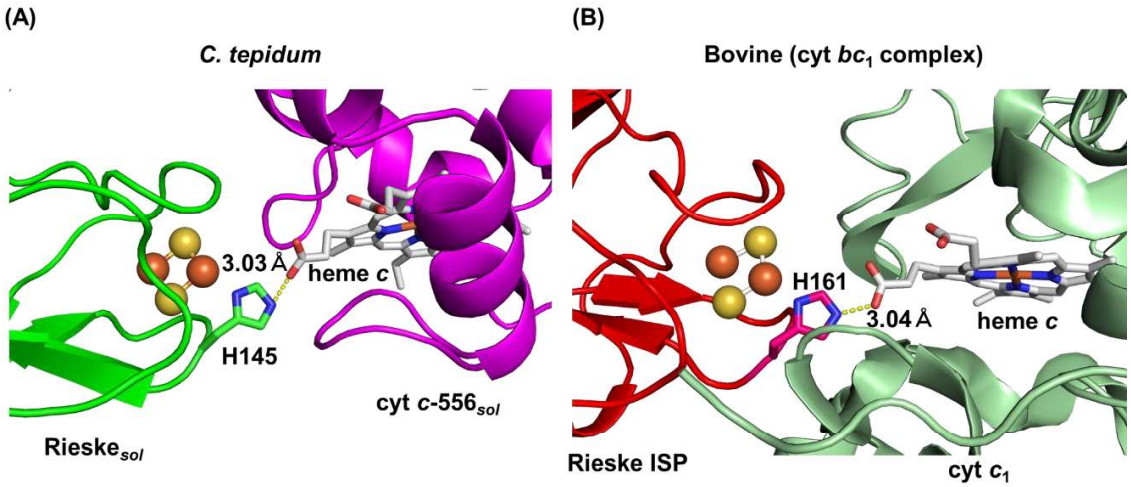


Figure 33. Interactions between the Rieske ISP and *c*-type cytochrome in *C. tepidum* and bovine heart

Hydrogen-bond formation in the docking model of the Rieske$_{sol}$ and cyt *c*-556$_{sol}$ in *C. tepidum* (A) compared with that between the Rieske ISP and cyt c_1 in cyt bc_1 complex of bovine heart (PDBID: 1BE3) (B). Both molecular interfaces are confirmed by Ligplot+. Single hydrogen bonds are formed between Nε of His145 of the Rieske ISP and O2D of propionate group of heme *c*-556 in *C. tepidum* (A), and Nε of His161 of the Rieske ISP and O1D of propionate group of heme c_1 in bovine heart (B), respectively.

Discussion

The *in vitro* results obtained in the present NMR measurements revealed that the Rieske$_{sol}$ and cyt *c*-556$_{sol}$ could form a weakly associated complex, through which electrons could be transferred between the Rieske [2Fe-2S] cluster and heme *c* in cyt *c*-556 by facing their cofactors to each other (Figure 32). The prerequisite for this interaction was the redox-state difference between the two proteins, which enables the electron transfer reaction to take place between them. The interface of the complex was formed by non-polar or hydrophobic interactions, as indicated by the docking model constructed in this study (Figure 34 and 35). No electrostatic attraction from a long-range distance was necessary for both proteins to be close together because the complex was formed even under high ionic strength conditions (Figure 29).

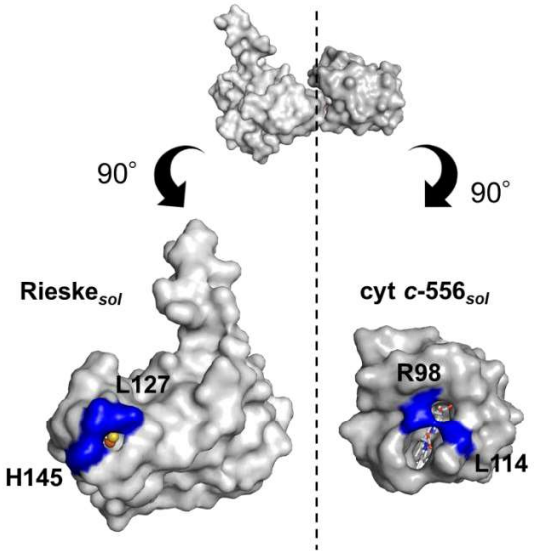


Figure 34. Open book view of non-polar interaction sites of the Rieske$_{sol}$ and cyt *c*-556$_{sol}$

Non-polar interaction formed between them are shown in blue. No electrostatic interactions were observed in this complex model.

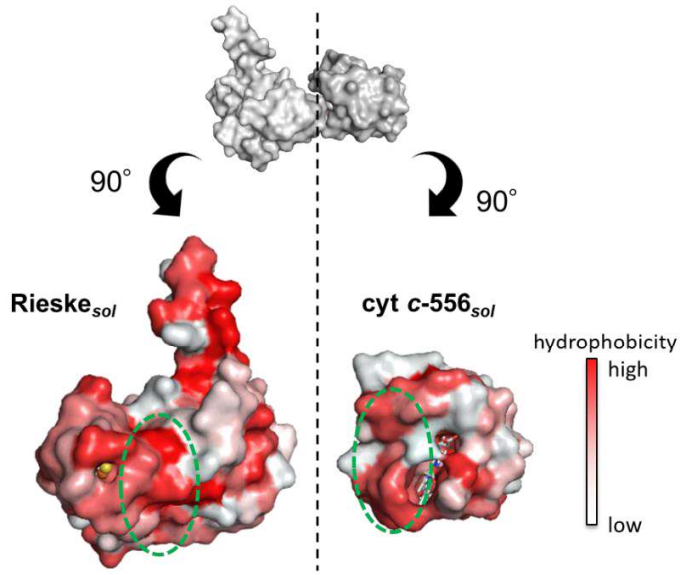


Figure 35. Open book view of hydrophobicity of the Rieske$_{sol}$ and cyt *c*-556$_{sol}$

The intensity of white indicates the greater polarity of the residues, while the intensity of red indicates greater hydrophobicity of the residues. Strong hydrophobic patches are observed in the immediate peripheral regions of co-factors on the surfaces of the Rieske$_{sol}$ and cyt *c*-556$_{sol}$, as indicated by green dotted circles. Hydrophobicity was determined in PyMOL using the "color_h" script [108].

The process of protein-protein interaction and subsequent complex formation in solution can be understood by a two-step model [69, 70]. The formation of the final optimal complex is preceded by the formation of a short-lived, dynamic encounter complex. A stepwise process is a dominant feature of the electron transfer reactions involved in energy conversion systems, such as respiration and photosynthesis, or other metabolic pathways. They have been intensively studied for these two decades with experimental and theoretical methods, focusing on the transiently formed interfaces, for examples, between yeast mitochondrial cyt *c* peroxidase and cyt *c*, between cyt c_1 in the cyt bc_1 complex and cyt *c*, between plant/cyanobacterial cyt *f* in cyt b_6f complex and plastocyanin, and between bacterial RC complex and cyt c_2 [69, 70, 87, 109]. A recent paramagnetic relaxation NMR spectroscopy data has shown that the distinction between the encounter and final complexes, so far assumed previously, is ambiguous actually and that the encounter complex could be electron-transfer active at any time by increasing non-polar interface areas [110].

On the other hand, the electron-transfer active complex between the Rieske$_{sol}$ and cyt *c*-556$_{sol}$ could be formed only by a non-polar interaction and any charge-related process to the complex formation seems precluded, contrary to the interaction process of a two-step model for redox proteins in solution. These two proteins intrinsically function as membrane components that directly transfer electrons to each other, and electrostatic interactions would not be required for their association. The two proteins seem to locate close to each other for easy contact by conformational changes.

As described in chapter I and II, a question would rise as to what factors discriminate the function between cyts *c*-554 and *c*-556 because the structures of these two

proteins exhibit very high similarities to each other [47]. One barely discernible difference is the relatively hydrophobic nature of the protein surface around the pyrrole ring III edge in cyt *c*-556 compared with the positively charged one in cyt *c*-554 (see Figure 15 and 16). This region should be critical for the association with the Rieske ISP through a non-polar interaction in a limited space area within the membranes as supported by the results obtained in the present NMR measurements. Another notable difference was that the longer loop between the α3 and α4 helices of cyt *c*-554 than that of cyt *c*-556. In the docking model between cyt *c*-556$_{sol}$ and the Rieske$_{sol}$, this loop has been shown to be the proper site where the protein surface area surrounding the [2Fe-2S] cluster makes direct contact (Figure 32). In contrast, the longer loop of cyt *c*-554 would prevent heme from getting close to the cluster, thus hindering complex formation with the Rieske ISP (Figure 36). Positively charged residues on this loop, Lys56 and/or Lys59, are expected to be involved in a long-distance electrostatic interaction with cyt c_z in the RC complex, as suggested by the two-step model for the electron transfer mechanism. In fact, the electron transfer rate from cyt *c*-554 to the P840 RC complex was reported to be decreased in high salt concentrations [39].

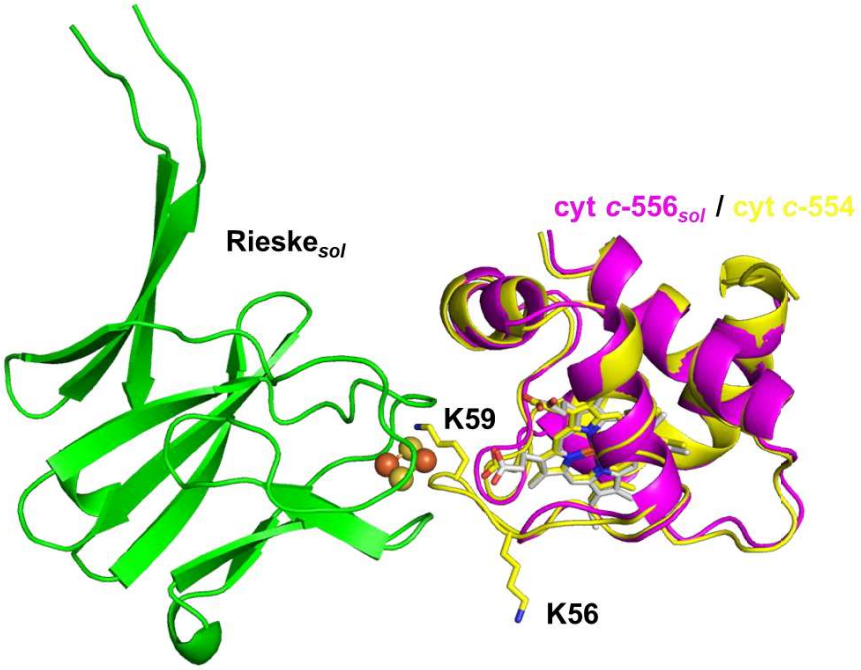


Figure 36. Structure comparison of cyt *c*-556$_{sol}$ and cyt *c*-554 on the docking model

The 3D structure of cyt *c*-554 was also superposed to that of cyt *c*-556$_{sol}$ by PyMOL. The longer loop of cyt c-554 is indicated to be crushed to the Rieske$_{sol}$ when it locates in the same position of cyt *c*-556 on the electron transfer reaction. This loop contains two lysine residues, Lys 56 and Lys59, which are expected to be involved in a long-distance electrostatic interaction between cyt *c*-554 and cyt c_z.

Cyt *c*-556 is supposed to be anchored into membranes with fatty acid chains covalently bound to the thiol group of the N-terminal cysteine residue [25]. This cytochrome serves as an electron carrier, substituting for cyt c_1/*f* in the typical cyt *bc* complexes. Recent comparative genomic studies have demonstrated that cyt c_1 and *f* in cyt *bc* complexes are completely structurally unrelated proteins. The Rieske/cyt*b* complexes have thus been proposed to be core proteins, into which various heme proteins are incorporated during the evolution of bioenergetic membranes to flow electrons to the acceptors, coupled with proton gradient formation [14, 15]. Phylogenetic analysis indicated that soluble cyt *c*-554 and membrane-anchored cyt *c*-556 diverged from a common ancestor, which is also supported by the close location of genes encoding their proteins, CT0075 and CT0073, respectively, in a genome. The two *c*-type cytochromes would have differentiated functions as needed during evolution [25, 27].

General discussion and Conclusion

The menaquinol:cytochrome *c* oxidoreductase in *C. tepidum* is the Rieske/cyt*b* complex which was supposed to have the most primitive type of cyt *bc* complexes. It was also thought to donate electrons directly to cyt c_z in the RC complex without any electron carriers. In 1994, the transcription unit containing *petCB*, which encode for the Rieske ISP and cyt *b*, was reported to lack the third gene of *petC* for cyt c_1 in *C. limicola*, one of the species belonging to the green clade, Chlorobiacea [22]. Since then, an electron carrier which functionally equivalent to cyt c_1 have been searched by using a combination of biochemical and spectroscopic methods [24, 25, 27]. In this study, I tried to examine the electron transfer mechanisms between the Rieske/cytb complex and RC by biochemical and structural methods. I also verified the function of the Rieske/cyt*b* complex whether this complex could function without *c*-type cytochromes as a core unit of cyt *bc* complexes and the evolutionary process from the Rieske/cyt*b* complex to cyt b_6f complex functioning in photosynthetic electron transport chain which obtains cyt *f* later in evolution.

In chapter I, I identify membrane-anchored cyt *c*-556 which was indicated to involve in electron transfer between the Rieske/cyt*b* complex and RC by spectroscopic studies, encoded by the *CT0073* gene in *C. tepidum* (see Figure 10). It also supposed this cytochrome transfers electrons specifically to cyt c_z in the RC. In chapter II and III, I determine the structures of cyt *c*-556_{sol} and $Rieske_{sol}$. Cyt *c*-556_{sol} is composed with α-helices as cyt c_1, while the $Rieske_{sol}$ shows biolobal shape as well as the soluble domains of the b_6f type Rieske ISP show [42]. The structure of cyt *c*-556_{sol} is similar to it of soluble cyt *c*-554 which transfer electron from the Sox system to RC. The difference of these two cytochromes is the loop which only cyt *c*-554 has. The structural information of $Rieske_{sol}$ support that the Rieske ISP evolved from low-potential type to high-potential type by

regulating redox potential in the cluster-binding subdomain to adapt to the electron donor and also to Z-scheme of photosynthetic electron transport chain. In chapter IV, I detect the interaction between the Rieske$_{sol}$ and cyt *c*-556$_{sol}$ to form a weakly associated complex for electron transfer by NMR measurements. I also construct the docking model of these proteins. The model shows that the interface of the complex is formed by non-polar interactions without electrostatic interactions. It indicates that they use electron transfer mechanism which does not need the long-range electrostatic interactions and is specific for membrane-associated proteins. A question would rise as to what factors discriminate the function that cyt *c*-554 cannot accept electrons from the Rieske ISP but cyt *c*-556 can because the structures of these cytochromes exhibit high similarities to each other. The docking model indicated that the longer loop in cyt *c*-554 would prevent heme *c* from getting closer to the cluster of Rieske$_{sol}$ because of physical crash.

Based on these results, I propose electron transfer model between the Rieske/cyt*b* complex and RC (Figure 37). Membrane-anchored cyt *c*-556 approaches and transfer electrons efficiently to cyt c_z in the RC by movement of the soluble domains, while soluble cyt *c*-554 transfers electrons to cyt c_z in a specific reaction manner that might be explained by two-step model. The Rieske ISP forms complex with cyt *c*-556 by movement of the soluble domains and non-polar interaction which would be specific manner in membrane-associated proteins because they locate closer in membrane. On the other hand, soluble cyt *c*-554 cold not accept electrons from the Rieske ISP because of physical crash. Therefore, green sulfur bacteria constructs electron transport chains in membrane that electrons are transferred from the Rieske/cyt*b* complex to RC not directly but through membrane-anchored cyt *c*-556.

I also present evolutionary process of cyt *bc* complexes. This complex was supposed to evolution from the Rieske/cyt*b* type to cyt bc_1 and b_6f complex by obtaining *c*-

type cytochromes. The Rieske/cyt*b* complex was thought as core unit of cyt *bc* complexes. However, results in this study indicate that the Rieske/cyt*b* complex cannot function independently and requires cyt *c*-556 to transfer electrons to the RC. Cyt *bc* complex in green sulfur bacteria would function as the association of the Rieske/cyt*b* complex and membrane-anchored cyt *c*-556 and would be a primitive complex which combines the characteristics of bc_1 and b_6f type complexes. I propose the evolutionary model that the Rieske/cyt*b* complex evolve to cyt b_6f complex by not obtaining cyt *f* but taking in membrane-anchored cyt *c*-556 to complex and replacing it by transmembrane cyt *f*.

Green sulfur bacteria belong to green clade, and structure of cyt *b* was thought to be similar to it of cyt b_6/subunit IV in cyt b_6f complex of cyanobacteria [21]. It corresponds to this evolutionary process that the Rieske/cyt*b* complex evolved to cyt b_6f complex. I am proceeding the purification of the Rieske/cyt*b* complex from *C. tepidum* to determine its structure by X-ray crystallography or single particle analysis. This information is necessary to reveal primitive mechanisms of cyt *bc* complexes in electron transport chain in detail.

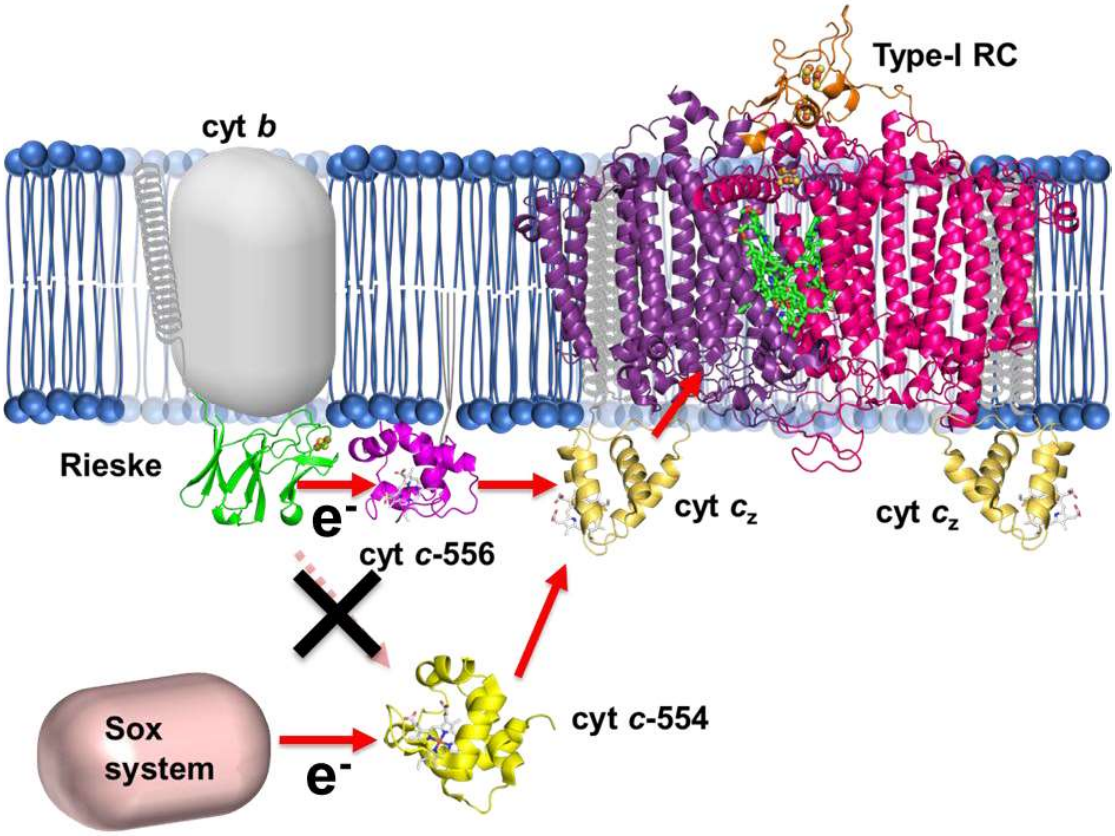


Figure 37. Schematic illustration of electron transfer mechanisms in *C. tepidum*

Red arrows indicate the direction of electron flows. An electron is transferred from the Rieske ISP to cyt c_z (PDBID: 3A9F) of the P840 RC complex (PDBID: 8GWA) via membrane-bound cyt *c*-556. The Rieske ISP and cyt c_z are anchored into membranes with membrane-spanning helices [111], and cyt *c*-556 with fatty acid chains, respectively [25]. The soluble domains of these three proteins are characterized by swinging in aqueous phase to make contacts with each other. Soluble cyt *c*-554 (PDBID: 4J20) accepts electrons from Sox system and transfers electron to cyt c_z. Cyt *c*-554 cannot accepts electrons from the Rieske/cyt*b* complex while cyt *c*-556 can. Therefore, it cannot function as soluble electron carrier between the Rieske/cyt*b* complex and RC.

List of Publication

1. Hyperfine Sublevel Correlation Spectroscopy Studies of Iron-Sulfur Cluster in Rieske Protein from Green Sulfur Bacterium *Chlorobaculum tepidum* Nagashima, H., Kishimoto, H., Mutoh, R., Terashima, N., Oh-oka, H., Kurisu, G., Mino, H. (2017) *Journal of Physical Chemistry B* **121**, 2543-53

2. Soluble Domains of Cytochrome *c*-556 and Rieske Iron-Sulfur Protein from *Chlorobaculum tepidum*: Crystal structures and Interaction Analysis Kishimoto, H., Azai, C., Yamamoto, T., Mutoh, R., Nakaniwa, T., Tanaka, H., Miyanoiri, Y., Kurisu, G., Oh-oka, H. (2023) *Current Research in Structural Biology* (in press)

Acknowledgements

The author would like to express my sincere gratitude to my advisor, Prof. Hirozo Oh-oka for the continuous support of my studies from 2014. His advice and guidance helped me in all the time of research and writing of this dissertation. I would like to extend my deepest gratitude to Prof. Genji Kurisu at Institute for Protein Research, Osaka Univ. for support my experiments at the Laboratory of Protein Crystallography.

I would like to thank Assoc. Prof. Hideaki Tanaka and Assoc. Prof. Yohei Miyanoiri at Institute for Protein Research, Osaka Univ., and Lecturer Risa Mutoh at Faculty of Science, Toho Univ. for their kind help and support to perform X-ray crystallography and NMR measurements. I would like to extend my thanks to Lecturer Chihiro Azai at College of Life Sciences, Ritsumeikan Univ. for his support for my studies in various respects. I am deeply grateful to Prof. Yasuhiro Takahashi at Grad. School of Science and Engineering, Saitama Univ. for offering *E. coli* C41(DE3) cells and pRKISC plasmid, and Dr. Kwan Kim at BioLeaders Corporation for supporting MS spectrometry. I am also grateful to the rest of my dissertation committee, Prof. Takahide Kon.

Special thanks to the member of Laboratory of Photosynthetic Biology Research and Laboratory of Protein Crystallography for their support for eight years.

References

[1] Raines, C. A. (2003) The Calvin cycle revisited. *Photosynthesis Research*. **75**, 1-10.
[2] Olson, J. M. (2006) Photosynthesis in the Archean Era. *Photosynthesis Research*. **88**, 109-117.
[3] Mitchell, P. (1976) Possible Molecular Mechanisms of the Protonmotive Function of Cytochrome Systems. *Journal of Theoretical Biology*. **62**, 327-367.
[4] Stirbet, A., Lazár, D., Guo, Y. & Govindjee, G. (2020) Photosynthesis: basics, history and modelling. *Annals of Botany*. **126**, 511-537.
[5] Bryant, D. A. & Frigaard, N. U. (2006) Prokaryotic photosynthesis and phototrophy illuminated. *Trends in Microbiology*. **14**, 488-496.
[6] Ferguson, S.J., Jackson, J. B. & McEwan, A. G. (1987) Anaerobic respiration in the Rhodospirillaceae: characterization of pathways and evaluation of roles in redox balancing during photosynthesis. *Fems Microbiology Letters*. **46**, 117-143.
[7] Chan, L. K., Morgan-Kiss, R. M. & Hanson, T. E. (2009) Functional Analysis of Three Sulfide:Quinone Oxidoreductase Homologs in *Chlorobaculum tepidum*. *Journal of Bacteriology*. **191**, 1026-1034.
[8] Friedrich, C. G., Bardischewsky, F., Rother, D., Quentmeier, A. & Fischer, J. (2005) Prokaryotic sulfur oxidation. *Current Opinion in Microbiology*. **8**, 253-259.
[9] Majumder, E. L. W. & Blankenship, R. E. (2016). The Diversity of Photosynthetic Cytochromes. Cytochrome Complexes: Evolution, Structures, Energy Transduction, and Signaling. **41**, 25-50.
[10] Esser, L., Elberry, M., Zhou, F., Yu, C. A., Yu, L. & Xia, D. (2008) Inhibitor-complexed Structures of the Cytochrome bc_1 from the Photosynthetic Bacterium *Rhodobacter sphaeroides*. *Journal of Biological Chemistry*. **283**, 2846-2857.
[11] Kurisu, G., Zhang, H. M., Smith, J. L. & Cramer, W. A. (2003). Structure of the Cytochrome b_6f Complex of Oxygenic Photosynthesis: Tuning the Cavity. *Science*. **302**, 1009-1014.
[12] Cape, J. L., Bowman, M. K. & Kramer, D. M. (2006). Understanding the cytochrome *bc* complexes by what they don't do. The Q-cycle at 30. *Trends in Plant Science*. **11**, 46-55.
[13] Kramer, D. M., Cruz, J. A. & Kanazawa, A. (2003). Balancing the central roles of the thylakoid proton gradient. *Trends in Plant Science*. **8**, 27-32.
[14] Schütz, M., Brugna, M., Lebrun, E., Baymann, F., Huber, R., Stetter, K. O., Hauska, G., Toci, R., Lemesle-Meunier, D., Tron, P., Schmidt, C. & Nitschke, W. (2000). Early evolution of cytochrome *bc* complexes. *Journal of Molecular Biology*. **300**, 663-675.
[15] Nitschke, W., Van Lis, R., Schoepp-Cothenet, B. & Baymann F. (2010). The "green" phylogenetic clade of Rieske/cyt*b* complexes. *Photosynthesis Research*. **104**, 347-355.
[16] Mendz, G. L., Smith, M. A., Finel, M. & Korolik, V. (2000). Characteristics of the aerobic respiratory chains of the microaerophiles *Campylobacter jejuni* and *Helicobacter pylori*. *Archives of Microbiology*. **174**,1-10.
[17] Baymann, F., Lebrun, E. & Nitschke, W. (2004). Mitochondrial cytochrome c_1 is a collapsed di-heme cytochrome. *Proceedings of the National Academy of Sciences of the United States of America*. **101**, 17737-17740.

[18] Sone, N., Tsuchiya, N., Inoue, M. & Noguchi, S. (1996). Bacillus stearothermophilus *qcr* operon encoding Rieske FeS protein, cytochrome b_6, and a novel-type cytochrome c_1 of quinol-cytochrome *c* reductase. *Journal of Biological Chemistry*. **271**, 12457-12462.
[19] Osyczka, A., Zhang, H., Mathé, C., Rich, P. R., Moser, C. C. & Dutton, P. L. (2006) Role of the PEWY Glutamate in Hydroquinone-Quinone Oxidation-Reduction Catalysis in the Q_o Site of Cytochrome bc_1. *Biochemistry*. **45**, 10492-10503.
[20] Kramer, D.M., Nitschke, W. & Cooley, J. W. (2009) The Cytochrome bc_1 and Related *bc* Complexes: The Rieske/Cytochrome *b* Complex as the Functional Core of a Central Electron/Proton Transfer Complex. Purple Phototrophic Bacteria. **28**, 451-473.
[21] Davidson, E. & Daldal, F. (1987). Primary structure of the bc_1 complex of *Rhodopseudomonas capsulata*: Nucleotide sequence of the *pet* operon encoding the rieske cytochrome *b*, and cytochrome c_1 apoproteins. *Journal of Molecular Biology*. **195**, 13-24.
[22] Schütz, M., Zirngibl, S., Lecoutre, J., Büttner, M., Xie, D. L., Nelson, N., Deutzmann, R. & Hauska, G. (1994). A transcription unit for the Rieske FeS-protein and cytochrome *b* in *Chlorobium limicola*. *Photosynthesis Research*. **39**, 163-174.
[23] Hauska, G., Schoedl, T., Remigy, H. & Tsiotis, G. (2001). The reaction center of green sulfur bacteria. *Biochimica et Biophysica Acta-Bioenergetics*. **1507**, 260-77.
[24] Oh-oka, H., Iwaki, M. & Itoh, S. (1998). Membrane-bound cytochrome c_z couples quinol oxidoreductase to the P840 reaction center complex in isolated membranes of the green sulfur bacterium *Chlorobium tepidum*. *Biochemistry*. **37**, 12293-12300.
[25] Azai, C., Tsukatani, Y., Itoh, S. & Oh-oka, H. (2010). *C*-type cytochromes in the photosynthetic electron transfer pathways in green sulfur bacteria and heliobacteria. *Photosynthesis Research*. **104**, 189-199.
[26] Thöny-Meyer, L., Fischer, F., Künzler. P., Ritz, D. & Hennecke, H. (1995) *Escherichia coli* Genes Required for Cytochrome *c* Maturation. *Journal of Bacteriology*. **177**, 4321-4326.
[27] Tsukatani, Y., Azai, C., Kondo, T., Itoh, S. & Oh-oka, H. (2008). Parallel electron donation pathways to cytochrome c_z in the type I homodimeric photosynthetic reaction center complex of *Chlorobium tepidum*. *Biochimica et Biophysica Acta-Bioenergetics*. **1777**, 1211-1217.
[28] Mavridou, D. A. I, Ferguson, S. J. & Stevens, J. M. (2013) Cytochrome *c* Assembly. *Iubmb Life*. **65**, 209-216.
[29] Verissimo, A. F. & Daldal, F. (2014) Cytochrome *c* biogenesis System I: An intricate process catalyzed by a maturase supercomplex? *Biochimica et Biophysica Acta-Bioenergetics*. **1837**, 989-998.
[30] Higuchi M., Hirano Y., Kimura Y., Oh-oka H., Miki K., Wang ZY. (2009). Overexpression, characterization, and crystallization of the functional domain of cytochrome c_z from *Chlorobium tepidum*. *Photosynthesis Research*. **102**, 77-84.
[31] Arslan, E., Schulz, H., Zufferey, R., Künzler, P. & Thöny-Meyer, L. (1998). Overproduction of the *Bradyrhizobium japonicum c*-type cytochrome subunits of the cbb_3 oxidase in *Escherichia coli*. *Biochemical and Biophysical Research Communications*. **251**, 744-747.
[32] Miroux, B. & Walker, J. E. (1996). Over-production of proteins in *Escherichia coli*: Mutant hosts that allow synthesis of some membrane proteins and globular proteins at high

levels. *Journal of Molecular Biology*. **260**, 289-298.
[33] Dutton, P. L. (1978). Redox potentiometry: determination of midpoint potentials of oxidation-reduction components of biological electron-transfer systems. *Methods in Enzymology*. **54**, 411-435.
[34] Tsukatani, Y., Miyamoto, R., Itoh, S. & Oh-oka, H. (2006). Soluble cytochrome *c*-554, CycA, is not essential for the photosynthetic electron transfer in *Chlorobium tepidum*. *FEBS Lett.* **580**, 2191–2194.
[35] Laemmli, U. K. (1970). Cleavage of Structural Proteins during the Assembly of Head of Bacteriophage T4. *Nature*. **227**, 680-685.
[36] Iwaki, M., Itoh, S., Kamei, S., Matsubara, H. & Oh-oka, H. (1999). Time-Resolved Spectroscopy of Chlorophyll-*a* like Electron Acceptor in the Reaction Center Complex of the Green Sulfur Bacterium *Chlorobium tepidum*. *Plant and Cell Physiology*. **40**, 1021-1028.
[37] Takaichi, S. & Oh-oka, H. (1999). Pigment Composition in the Reaction Center Complex from the Thermophilic Green Sulfur Bacterium, *Chlorobium tepidum*: Carotenoid Glucoside Esters, Menaquinone and Chlorophylls. *Plant and Cell Physiology*. **40**, 691-694.
[38] Tsukatani, Y., Miyamoto, R., Itoh, S. & Oh-oka, H. (2004). Function of a PscD Subunit in a Homodimeric Reaction Center Complex of the Photosynthetic Green Sulfur Bacterium *Chlorobium tepidum* Studied by Insertional Gene Inactivation - Regulation of Energy Transfer and Ferredoxin-Mediated $NADP^+$ Reduction on the Cytoplasmic Side. *Journal of Biological Chemistry*. **279**, 51122-51130.
[39] Okumura, N., Shimada, K. & Matsuura, K. (1994). Photooxidation of membrane-bound and soluble cytochrome *c* in the green sulfur bacterium *Chlorobium tepidum*. *Photosynthesis Research*. **41**, 125-134.
[40] Oh-oka, H., Kamei, S., Matsubara, H., Iwaki, M. & Itoh, S. (1995). 2 molecules of cytochrome *c* function as the electron donors to P840 in the reaction center complex isolated from a green sulfur bacterium, *Chlorobium tepidum*. *Febs Letters*. **365**, 30-34.
[41] Kjær, B. & Scheller, H. V. (1996) An isolated reaction center complex from the green sulfur bacterium *Chlorobium vibrioforme* can photoreduce ferredoxin at high rates. *Photosynthesis Research*. **47**, 33-39.
[42] Hirano, Y., Higuchi, M., Azai, C., Oh-oka, H., Miki, K. & Wang, Z. Y. (2010). Crystal Structure of the Electron Carrier Domain of the Reaction Center Cytochrome c_z Subunit from Green Photosynthetic Bacterium *Chlorobium tepidum*. *Journal of Molecular Biology*. **397**, 1175-1187.
[43] Knaff, D. B. & Malkin, R. (1976). Iron-sulfur proteins of green photosynthetic bacterium *chlorobium*. *Biochimica et Biophysica Acta*. **430**, 244-252.
[44] Von Jagow, G. & Link, T. A. (1986). Use of specific inhibitors on the mitochondrial bc_1 complex. *Methods in Enzymology*. **126**, 253-271.
[45] Itoh, M., Seo, D., Sakurai, H. & Sétif, P. (2002) Kinetics of electron transfer between soluble cytochrome *c*-554 and purified reaction center complex from the green sulfur bacterium *Chlorobium tepidum*. *Photosynthesis Research*. **71**, 125-135.
[46] Jenney, F. E., Prince, R. C. & Daldal, F. (1994). Roles of the Soluble Cytochrome c_2 and Membrane-Associated Cytochrome c_y of *Rhodobacter capsulatus* in Photosynthetic Electron Transfer. *Biochemistry*. **33**, 2496-2502.

[47] Yu, L. J., Unno, M., Kimura, Y., Yanagimoto, K., Oh-oka, H. & Wang-Otomo, Z. Y. (2013). Structure analysis and characterization of the cytochrome *c*-554 from thermophilic green sulfur photosynthetic bacterium *Chlorobaculum tepidum*. *Photosynthesis Research*. **118**, 249-258.
[48] Hirano, Y., Higuchi, M., Azai, C., Oh-oka, H., Miki, K. & Wang, Z. Y. (2010). Crystal Structure of the Electron Carrier Domain of the Reaction Center Cytochrome c_Z Subunit from Green Photosynthetic Bacterium *Chlorobium tepidum*. *Journal of Molecular Biology*. **397**, 1175-1187.
[49] Otwinowski, Z. & Minor, W. (1997). Processing of X-ray diffraction data collected in oscillation mode. *Macromolecular Crystallography, Pt A*. **276**, 307-326.
[50] Winn, M. D., Ballard, C. C., Cowtan, K. D., Dodson, E. J., Emsley, P., Evans, P. R., Keegan, R. M., Krissinel, E. B., Leslie, A. G. W., McCoy, A., McNicholas, S. J., Murshudov, G. N., Pannu, N. S., Potterton, E. A., Powell, H. R., Read, R. J., Vagin, A. & Wilson, K. S. (2011). Overview of the *CCP4* suite and current developments. *Acta Crystallographica Section D-Structural Biology*. **67**, 235-242.
[51] Murshudov, G. N., Vagin, A. A. & Dodson, E. J. (1997) Refinement of macromolecular structures by the maximum-likelihood method. *Acta Crystallographica Section D-Structural Biology*. **53**, 240-255.
[52] Emsley, P. & Cowtan, K. (2004). *Coot*: model-building tools for molecular graphics. *Acta Crystallographica Section D-Structural Biology*. **60**, 2126-2132.
[53] Liebschner, D., Afonine, P. V., Baker, M. L., Bunkóczi, G., Chen, V. B., Croll, T. I., Hintze, B., Hung, L. W., Jain, S., McCoy, A. J., Moriarty, N. W., Oeffner, R. D., Poon, B. K., Prisant, M. G., Read, R. J., Richardson, J. S., Richardson, D. C., Sammito, M. D., Sobolev, O. V., Stockwell, D. H., Terwilliger, T. C., Urzhumtsev, A. G., Videau, L. L., Williams, C. J. & Adams, P. D. (2019). Macromolecular structure determination using X-rays, neutrons and electrons: recent developments in *Phenix*. *Acta Crystallographica Section D Structural Biology*. **75**, 861-877.
[54] Terwilliger, T. C., Adams, P. D., Read, R. J., McCoy, A. J., Moriarty, N. W., Grosse-Kunstleve, R. W., Afonine, P. V., Zwart, P. H. & Hung, L. W. (2009) Decision-making in structure solution using Bayesian estimates of map quality: the *PHENIX AutoSol* wizard. *Acta Crystallographica Section D Biological Crystallography*. **65**, 582-601.
[55] Ambler, R. P. (1991). Sequence variability in bacterial cytochromes *c*. *Biochimica et Biophysica Acta*. **1058**, 42-47.
[56] Kabsch, W. & Sander, C. (1983). Dictionary of protein secondary structure: Pattern recognition of hydrogen-bonded and geometrical features. *Biopolymers*. **22**, 2577-2637.
[57] Holm, L. (2022). Dali server: structural unification of protein families. *Nucleic Acids Research*. **50**, W210-W5.
[58] Carter, D. C., Melis, K. A., O'Donnell, S. E., Burgess, B. K., Furey, W. F., Wang, B. C. & Stout, C. D. (1985). Crystal structure of *Azotobacter* cytochrome c_5 at 2.5 Å resolution. *Journal of Molecular Biology*. **184**, 279-295.
[59] Bersch, B., Blackledge, M. J., Meyer, T. E. & Marion, D. (1996). *Ectothiorhodospira halophila* Ferrocytochrome c_{551}: Solution Structure and Comparison with Bacterial Cytochromes *c*. *Journal of Molecular Biology*. **264**, 567-584.
[60] Worrall, J. A. R., Schlarb-Ridley, B. G., Reda, T., Marcaida, M. J., Moorlen, R. J.,

Wastl, J., Hirst, J., Bendall, D. S., Luisi, B. F. & Howe, C. J. (2007). Modulation of heme redox potential in the cytochrome c_6 family. *Journal of the American Chemical Society*. **129**, 9468-9475.
[61] Meyer, T. E., Bartsch, R. G., Cusanovich, M. A. & Mathewson, J. H. (1968) The cytochromes of *Chlorobium thiosulfatophilum*. *Biochimica et Biophysica Acta-Bioenergetics*. **153**, 854-861.
[62] Kusai, A. & Yamanaka, T. (1973) A novel function of cytochrome *c*(555, *Chlorobium thiosulfatophilum*) in oxidation of thiosulfate. *Biochemical and Biophysical Research Communications*. **51**, 107-112.
[63] Friedrich, C. G., Rother, D., Bardischewsky, F., Quentmeier, A. & Fischer, J. (2001) Oxidation of Reduced Inorganic Sulfur Compounds by Bacteria: Emergence of a Common Mechanism? *Applied and Environmental Microbiology*. **67**, 2873-2882.
[64] Ogawa, T., Furusawa, T., Nomura, R., Seo, D., Hosoya-Matsuda, N., Sakurai, H. & Inoue, K. (2008) SoxAX Binding Protein, a Novel Component of the Thiosulfate-Oxidizing Multienzyme System in the Green Sulfur Bacterium *Chlorobium tepidum*. *Journal of Bacteriology*. **190**, 6097-6110.
[65] Tetreault, M., Cusanovich, M., Meyer, T., Axelrod, H. & Okamura, M. Y. (2002). Double mutant studies identify electrostatic interactions that are important for docking cytochrome c_2 onto the bacterial reaction center. *Biochemistry*. **41**, 5807-5815.
[66] Sommer, F., Drepper, F., Haehnel, W. & Hippler, M. (2006). Identification of precise electrostatic recognition sites between cytochrome c_6 and the photosystem I subunit PsaF using mass spectrometry. *Journal of Biological Chemistry*. **281**, 35097-35103.
[67] Baker, N. A., Sept, D., Joseph, S., Holst, M. J. & McCammon, J. A. (2001). Electrostatics of nanosystems: Application to microtubules and the ribosome. *Proceedings of the National Academy of Sciences of the United States of America*. **98**, 10037-10041.
[68] Dolinsky, T. J., Nielsen, J. E., McCammon, J. A. & Baker, N. A. (2004). PDB2PQR: an automated pipeline for the setup of Poisson-Boltzmann electrostatics calculations. *Nucleic Acids Research*. **32**, W665-W7.
[69] Ubbink, M., Ejdebäck, M., Karlsson, B. G. & Bendall, D. S. (1998). The structure of the complex of plastocyanin and cytochrome *f*, determined by paramagnetic NMR and restrained rigid-body molecular dynamics. *Structure*. **6**, 323-335.
[70] Volkov, A. N., Worrall, J. A. R., Holtzmann, E. & Ubbink, M. (2006). Solution structure and dynamics of the complex between cytochrome *c* and cytochrome c peroxidase determined by paramagnetic NMR. *Proceedings of the National Academy of Sciences of the United States of America*. **103**, 18945-18950.
[71] Chen, J. H., Wang, W. W., Wang, C., Kuang, T. Y., Shen, J. R. & Zhang, X. (2023) Cryo-electron microscopy structure of the intact photosynthetic light-harvesting antenna-reaction center complex from a green sulfur bacterium. *Journal of Integrative Plant Biology*. **65**, 223-234.
[72] Berry, E. A., De Bari, H. & Huang, L. S. (2013) Unanswered questions about the structure of cytochrome bc_1 complexes. *Biochimica et Biophysica Acta-Bioenergetics*. **1827**, 1258-1277.
[73] Xia, D., Esser, L., Tang, W. K., Zhou, F., Zhou, Y., Yu, L. & Yu, C. A. (2013) Structural analysis of cytochrome bc_1 complexes: Implications to the mechanism of

function. *Biochimica et Biophysica Acta-Bioenergetics*. **1827**, 1278-1294.
[74] Kleinschroth, T., Castellani, M., Trinh, C. H., Morgner, N., Brutschy, B., Ludwig, B. & Hunte, C. (2011). X-ray structure of the dimeric cytochrome bc_1 complex from the soil bacterium *Paracoccus denitrificans* at 2.7-Å resolution. *Biochimica et Biophysica Acta-Bioenergetics*. **1807**, 1606-1615.
[75] Takahashi, Y. & Nakamura, M. (1999). Functional assignment of the ORF2-*iscS-iscU-iscA-hscB-hscA-fdx*-ORF3 gene cluster involved in the assembly of Fe-S clusters in *Escherichia coli*. *Journal of Biochemistry*. **126**, 917-926.
[76] LeMaster, D. M. & Richards, F. M. (1985). ^{1}H-^{15}N Heteronuclear NMR Studies of *Escherichia coli* Thioredoxin in Samples Isotopically Labeled by Residue Type. *Biochemistry*. **24**, 7263-7268.
[77] Guerrero, S. A., Hecht, H. J., Hofmann, B., Biebl, H. & Singh, M. (2001). Production of selenomethionine-labelled proteins using simplified culture conditions and generally applicable host/vector systems. *Applied Microbiology and Biotechnology*. **56**, 718-723.
[78] Iwata, S., Saynovits, M., Link, T. A. & Michel, H. (1996) Structure of a water soluble fragment of the 'Rieske' iron sulfur protein of the bovine heart mitochondrial cytochrome bc_1 complex determined by MAD phasing at 1.5 Å resolution. *Structure*. **4**, 567-579.
[79] Link, T. A. & Iwata, S. (1996) Functional implications of the structure of the 'Rieske' iron-sulfur protein of bovine heart mitochondrial cytochrome bc_1 complex. *Biochimica et Biophysica Acta-Bioenergetics*. **1275**, 54-60.
[80] Carrell, C. J., Zhang, H. M., Cramer, W. A. & Smith, J. L. (1997). Biological identity and diversity in photosynthesis and respiration: structure of the lumen-side domain of the chloroplast Rieske protein. *Structure*. **5**, 1613-1625.
[81] Bönisch, H., Schmidt, C. L., Schäfer, G. & Ladenstein, R. (2002). The structure of the soluble domain of an archaeal Rieske iron-sulfur protein at 1.1 Å resolution. *Journal of Molecular Biology*. **319**, 791-805.
[82] Veit, S., Takeda, K., Tsunoyama, Y., Baymann, F., Nevo, R., Reich, Z., Rögner, M. & Miki, K. (2016). Structural and functional characterisation of the cyanobacterial PetC3 Rieske protein family. *Biochimica et Biophysica Acta-Bioenergetics*. **1857**, 1879-1891.
[83] Nagashima, H., Kishimoto, H., Mutoh, R., Terashima, N., Oh-Oka, H., Kurisu, G. & Mino, H. (2017). Hyperfine Sublevel Correlation Spectroscopy Studies of Iron-Sulfur Cluster in Rieske Protein from Green Sulfur Bacterium *Chlorobaculum tepidum*. *Journal of Physical Chemistry B*. **121**, 2543-2553.
[84] Hasan, S. S. & Cramer, W. A. (2014). Internal Lipid Architecture of the Hetero-Oligomeric Cytochrome b_6f Complex. *Structure*. **22**, 1008-1015.
[85] Stroebel, D., Choquet, Y., Popot, J. L. & Picot, D. (2003). An atypical haem in the cytochrome b_6f complex. *Nature*. **426**, 413-418.
[86] Veit, S., Takeda, K., Tsunoyama, Y., Rexroth, D., Rogner, M. & Miki, K. (2012). Structure of a thermophilic cyanobacterial b_6f-type Rieske protein. *Acta Crystallographica Section D-Structural Biology*. **68**, 1400-1408.
[87] Lange, C. & Hunte, C. (2002). Crystal structure of the yeast cytochrome bc_1 complex with its bound substrate cytochrome *c*. *Proceedings of the National Academy of Sciences of the United States of America*. **99**, 2800-2805.
[88] Berry, E. A., Huang, L. S., Saechao, L. K., Pon, N. G., Valkova-Valchanova, M. &

Daldal, F. (2004). X-ray Structure of *Rhodobacter capsulatus* Cytochrome bc_1: Comparison with its Mitochondrial and Chloroplast Counterparts. *Photosynthesis Research*. **81**, 251-275.
[89] Thompson, J. D., Higgins, D. G. & Gibson, T. J. (1994). CLUSTAL W: improving the sensitivity of progressive multiple sequence alignment through sequence weighting, position-specific gap penalties and weight matrix choice. *Nucleic Acids Research*. **22**, 4673-4680.
[90] Schneider, D., Skrzypczak, S., Anemüller, S., Schmidt, C. L., Seidler, A. & Rögner, M. (2002). Heterogeneous Rieske proteins in the cytochrome b_6f complex of *Synechocystis* PCC6803? *Journal of Biological Chemistry*. **277**, 10949-10954.
[91] Zhang, H., Carrell, C. J., Huang, D. R., Sled, V., Ohnishi, T., Smith, J. L. & Cramer, W. A. (1996). Characterization and crystallization of the lumen side domain of the chloroplast Rieske iron-sulfur protein. *Journal of Biological Chemistry*. **271**, 31360-31366.
[92] Link, T. A., Hagen, W. R., Pierik, A. J., Assmann, C. & Von Jagow, G. (1992). Determination of the redox properties of the Rieske [2Fe-2S] cluster of bovine heart bc_1 complex by direct electrochemistry of a water-soluble fragment. *European Journal of Biochemistry*. **208**, 685-691.
[93] Schröter, T., Hatzfeld, O. M., Gemeinhardt, S., Korn, M., Friedrich, T., Ludwig, B. & Link, T. A. (1998). Mutational analysis of residues forming hydrogen bonds in the Rieske [2Fe-2S] cluster of the cytochrome bc_1 complex in Paracoccus denitrificans. *European Journal of Biochemistry.* **255**, 100-106.
[94] Kolling, D. J., Brunzelle, J. S., Lhee, S., Crofts, A. R. & Nair, S. K. (2007). Atomic resolution structures of Rieske iron-sulfur protein: Role of hydrogen bonds in tuning the redox potential of iron-sulfur clusters. *Structure*. **15**, 29-38.
[95] Gasteiger, E., Gattiker, A., Hoogland, C., Ivanyi, I., Appel, R. D. & Bairoch, A. (2003). ExPASy: the proteomics server for in-depth protein knowledge and analysis. *Nucleic Acids Research*. **31**, 3784-3788.
[96] Denke, E., Merbitz-Zahradnik, T., Hatzfeld, O. M., Snyder, C. H., Link, T. A. & Trumpower, B. L. (1998) Alteration of the Midpoint Potential and Catalytic Activity of the Rieske Iron-Sulfur Protein by Changes of Amino Acids Forming Hydrogen Bonds to the Iron-Sulfur Cluster. *Journal of Biological Chemistry*. **273**, 9085-9093.
[97] Guergova-Kuras, M., Kuras, R., Ugulava, N., Hadad, I. & Crofts, A. R. (2000) Specific Mutagenesis of the Rieske Iron-Sulfur Protein in *Rhodobacter sphaeroides* Shows That both the Thermodynamic Gradient and the pK of the Oxidized Form Determine the Rate of Quinol Oxidation by the bc_1 Complex. *Biochemistry*. **39**, 7436-7444.
[98] Soballe, B. & Poole, R. K. (1999) Microbial ubiquinones: multiple roles in respiration, gene regulation and oxidative stress management. *Microbiology*. **145**, 1817-1830.
[99] Mutoh, R., Muraki, N., Shinmura, K., Kubota-Kawai, H., Lee, Y. H., Nowaczyk, M. M., Rögner, M., Hase, T., Ikegami, T. & Kurisu, G. (2015) X-ray Structure and Nuclear Magnetic Resonance Analysis of the Interaction Sites of the Ga-Substituted Cyanobacterial Ferredoxin. *Biochemistry*. **54**, 6052-6061.
[100] Lee, W., Tonelli, M. & Markley, J. L. (2015). NMRFAM-SPARKY: enhanced software for biomolecular NMR spectroscopy. *Bioinformatics*. **31**, 1325-1327.
[101] Lee, W., Bahrami, A., Dashti, H. T., Eghbalnia, H. R., Tonelli, M., Westler, W. M. &

Markley, J. L. (2019). I-PINE web server: an integrative probabilistic NMR assignment system for proteins. *Journal of Biomolecular NMR*. **73**, 213-222.
[102] Pierce, B. G., Wiehe, K., Hwang, H., Kim, B. H., Vreven, T. & Weng, Z. P. (2014). ZDOCK server: interactive docking prediction of protein-protein complexes and symmetric multimers. *Bioinformatics*. **30**, 1771-1773.
[103] Krissinel, E. & Henrick, K. (2007). Inference of macromolecular assemblies from crystalline state. *Journal of Molecular Biology*. **372**, 774-797.
[104] Krissinel, E. (2010). Crystal Contacts as Nature's Docking Solutions. *Journal of Computational Chemistry*. **31**, 133-143.
[105] Laskowski, R. A. & Swindells, M. B. (2011). LigPlot+: Multiple Ligand-Protein Interaction Diagrams for Drug Discovery. *Journal of Chemical Information and Modeling*. **51**, 2778-2786.
[106] Iwata, M., Björkman, J. & Iwata, S. (1999). Conformational change of the Rieske [2Fe-2S] protein in cytochrome bc_1 complex. *Journal of Bioenergetics and Biomembranes*. **31**, 169-175.
[107] Kazanis, S., Pochapsky, T. C., Barnhart, T. M., Pennerhahn, J. E., Mirza, U. A. & Chait, B. T. (1995). Conversion of a FE_2S_2 Ferredoxin into a Ga^{3+} Rubredoxin. *Journal of the American Chemical Society*. **117**, 6625-6626.
[108] Eisenberg, D., Schwarz, E., Komaromy, M. & Wall, R. (1984). Analysis of membrane and surface protein sequences with the hydrophobic moment plot. *Journal of Molecular Biology*. **179**, 125-142.
[109] Axelrod, H. L. & Okamura, M. Y. (2005). The structure and function of the cytochrome c_2: reaction center electron transfer complex from *Rhodobacter sphaeroides*. *Photosynthesis Research*. **85**, 101-114.
[110] Volkov, A. N. (2015). Structure and Function of Transient Encounters of Redox Proteins. *Accounts of Chemical Research*. **48**, 3036-2043.
[111] Oh-oka, H., Iwaki, M. & Itoh, S. (1997). Viscosity Dependence of the Electron Transfer Rate from Bound Cytochrome *c* to P840 in the Photosynthetic Reaction Center of the Green Sulfur Bacterium *Chlorobium tepidum*. *Biochemistry*. **36**, 9267-9272.